Dynamical Modeling of Marine Boundary Layer convection

By
Hung-chi Kuo

PI: Wayne H. Schubert and Thomas H. Vonder Haar

Department of Atmospheric Science
Colorado State University
Fort Collins, Colorado

Colorado State University

Department of Atmospheric Science

Paper No. 412

DYNAMICAL MODELING OF MARINE BOUNDARY LAYER CONVECTION

by
Hung-chi Kuo

Research supported by NSF Grant ATM-8510664, ONR Grant N00014-84-C-0591 and NOAA Grant NA-85-RAH05045

Principal Investigators: Wayne H. Schubert
Thomas H. Vonder Haar

Department of Atmospheric Science
Colorado State University
Fort Collins, Colorado 80523

April 1987

Atmospheric Science Paper No. 412

This paper was also submitted in partial fulfillment of the requirements for the Degree of Doctor of Philosophy.

ABSTRACT OF THESIS

DYNAMICAL MODELING OF MARINE BOUNDARY LAYER CONVECTION

This dissertation investigates the interaction between dynamics and infrared radiation as well as the problem of entrainment instability in the cloud-topped marine boundary layer. To eliminate most of the assumptions made in the simpler thermodynamic models, a two-dimensional Boussinesq moist model with a numerical technique (Fourier-Chebyshev tau method) and resolution sufficient to simulate cloud top processes has been developed. With the spectral tau method and fourth-order Runge-Kutta time integration scheme, we have higher accuracy with far fewer degrees of freedom and yet realize great computational efficiency when the desired accuracy is high enough.

Previous measurements suggest that the cloud-top radiative cooling is likely to undergo significant horizontal as well as vertical variability which will be principally governed by the variability of cloud liquid water. To investigate the impact of infrared cooling on the boundary layer dynamics, numerical experiments on marine boundary layer convection under various radiative forcings are performed. The results indicate that the model steady state does not depend on the horizontal and the vertical distribution of the cooling so long as the cooling is confined to the turbulent region. The sensitivity of the model to infrared cooling appears to be primarily in the vertical placement of the cooling relative to the turbulent cloud top region. Since the theory of radiative transfer does not support the existence of infrared cooling in the capping inversion (zero cloud fraction or non-turbulent region), a detailed radiative transfer calculation or observation to consider the spatial variability of cloud-top cooling is not necessary.

The thermodynamic theory as well as observations taken during the last fifteen years have been summarized. The results indicate that stratocumulus remain solid even when the equivalent potential temperature change across cloud top satisfies the theoretical entrain-

ment instability criterion. From an initial value problem with an initial cold anomaly, we conclude that insufficient evaporative cooling of the entraining air may be the key missing ingredient in the classical entrainment instability argument. Because of insufficient evaporation, the mixed parcel will not be colder than the surrounding environment even when the equivalent potential temperature jump is negative.

Numerical simulations for stable and unstable soundings under both interactive and non-interactive infrared radiative forcings are performed. The simulated stratocumulus contain dome-shaped convective structures with sharp liquid water gradients on the sides. There is one cell of circulation in the vertical. No decoupled vertical circulation between cloud and sub-cloud layer is observed. The cloud cells can decay and reform in a finite time. The appearance and disappearance of cloud holes may have nothing to do with entrainment instability. We do not observe signs of stratocumulus breakup by entrainment instability in any of the simulations, even in the situation of strong entrainment. The flux profiles averaged over a one hour period suggest that different soundings under different radiative forcings are in the same equilibrium state. This further supports the point that the horizontal variation of infrared cooling will not affect the equilibrium dynamics of the boundary layer. Unless there are multiple equilibria, we should not expect the breakup of marine stratocumulus by the entrainment instability mechanism.

Hung-chi Kuo
Atmospheric Science Department
Colorado State University
Fort Collins, Colorado 80523
Spring 1987

ACKNOWLEDGMENTS

The author wishes to thank his advisers, Professors Wayne H. Schubert and Thomas H. Vonder Haar, for their guidance and support during this work and throughout my tenure as a graduate student. Many thanks also go to the other members of my advisory committee, Professors Richard H. Johnson and Gerald D. Taylor, for their careful review of this research. The author has benefited greatly from discussions with George Young, Philip A. Durkee and Paul Ciesielski. Clark Weaver and Chi-Fan Shih are acknowledged for their support and advice concerning the DYCOMS data. A special note of thanks also goes to Jenny Martin for her expertise and efficiency in preparing this manuscript.

The author would like to extend special thanks to Scott Fulton for providing the package of Chebyshev routines which were so important for the completion of this dissertation. Lastly, the author wishes to thank his wife Ling-ling for her companionship and encouragement during the time period of research.

This work was supported by NSF grant ATM-8510664 and ONR grant N00014-84-C-0591, with additional support from the Cooperative Institute for Research in the Atmosphere (CIRA) at Colorado State University. Acknowledgment is also made to the National Center for Atmospheric Research, which is sponsored by the National Science Foundation, for computer time used in this research.

TABLE OF CONTENTS

LIST OF TABLES

LIST OF FIGURES

CHAPTER I

INTRODUCTION

Two popular misconceptions among inexperienced meteorologists are that layered clouds are always associated with gentle large-scale ascending motion and that strong temperature inversions act as "lids" through which no air moves. Both of these ideas collapse as soon as one begins to understand the physical processes involved in boundary layer stratocumulus. These layered clouds often extend for hundreds or thousands of kilometers over the cold ocean in the face of large-scale descent in the northern hemisphere summer, when upward motion in the ITCZ and downward motion in the subtropical highs is strongest. The descending air moves right through the strong temperature inversion at or just above cloud top. Schubert et al. (1979a) identified five principal cool coastal dry climates bordered by a cool ocean current, frequently associated with large stratocumulus cloud decks (coastal California and Mexico, Ecuador, Peru and Chile, northwestern Africa, southwestern Africa and northeastern Africa). Other areas where favorable synoptic conditions frequently occur and boundary layer stratocumulus are often observed are near the southern coast of Australia (Paltridge, 1974; Platt, 1976), over the northern Atlantic and over the North Sea (e.g., Slingo et al., 1982a,b; Roach et al., 1982; Nicholls, 1984) and during wintertime cold air outbreaks over the Kuroshio Current (e.g., Ninomiya, 1975; Nitta, 1976; Lenschow and Agee, 1976), the Gulf Stream and the Great Lakes (Lenschow, 1973).

Although marine stratocumulus convection may not attract as much attention as other more violent weather systems, it appears to play an important and especially interesting role in the global atmospheric circulation and climate. Like nonprecipitating trade wind cumulus convection, stratocumulus convection in the subtropical region condenses water at lower levels, transports it upward and evaporates it at higher levels, and in so doing, moistens the air in the downward branches of the Hadley cell. Thus, stratocumulus and trade wind

cumulus together can be thought of as the giant humidifiers of the air flowing toward the intertropical convergence zone. Other regions of stratocumulus clouds also strongly influence the rate of heat and moisture exchange between the troposphere and the boundary layer. These clouds play an important role in the hydrological cycle of the earth-atmosphere system. In addition, the high albedo of the stratocumulus compared with that of the ocean background reduces the flux of solar radiation into the atmosphere-ocean system while their low altitude prevents significant compensation in thermal emission. Owing to their effect on the earth's radiative energy budget, maritime stratocumulus are likely to influence climate change strongly. Clearly, any realistic general circulation model has to reproduce reasonably extensive stratocumulus decks in order to simulate the climate. Besides these quasi-persistent influences on the earth's climate, stratocumulus are also important for short-range weather forecasting in coastal areas. The prediction of air temperature or fog formation and dispersal is very sensitive to the presence or absence of stratocumulus.

Because of the importance of these clouds, there has been considerable theoretical work on stratocumulus convection. Modeling work on the marine boundary layer can be divided into three classes of increasing complexity. These three classes range in complexity from the simple thermodynamical (mixed layer and variable lapse rate models), to the semi-dynamic (one-dimensional turbulence closure models), and finally to detailed two- or three-dimensional dynamical models. In the mixed layer models equivalent potential temperature Θ and total water mixing ratio r are assumed to be independent of height below the inversion. These models then have three degrees of prognostic freedom for the vertical structure, i.e. the only predictive equations are for Θ, r and the boundary layer depth z_B. The mixed layer model was first described by Lilly (1968). Variations and applications of this model are described by Schubert (1976), Deardorff (1976), Kraus and Schaller (1978a,b), Schubert et al. (1979a,b), Schaller and Kraus (1981a,b), Randall (1980a), Wakefield and Schubert (1981), Fravalo et al.(1981), Stage and Businger (1981a,b), and others. Albrecht et al.(1979a,b) studied the trade wind boundary layer with a variable lapse rate model which allows more degrees of freedom in the vertical. Studies of stratocumulus have also been made using one-dimensional turbulence closure models (Burke, 1977; Oliver et al. 1978; Bougeault, 1981a,b,1982,1985; Chen and Cotton, 1983a,b). The one-dimensional turbu-

lence closure models are continuous in the vertical so that discretized versions can have any number of degrees of freedom in the vertical. However, since they do not explicitly calculate horizontal variation of convective elements, they are only semi-dynamic, and their results are crucially dependent on the turbulence closure. Finally, two- and three-dimensional dynamic models usually involve numerical integration of the Boussinesq equations for shallow moist convection. Air mass transformation over a warm sea has been studied by two-dimensional modeling (Asai and Nakamura, 1978; Nakamura and Asai, 1985). Three-dimensional models have been used to test assumptions made in simple mixed-layer models by Deardorff (1980b) and Moeng (1986, 1987).

A list of past contributions to the theory of cloud-topped boundary layers indicates a strong preference for the simple mixed layer model. Along with the concentration on simple thermodynamic models there have arisen several questions, two of the most recurrent being:

- How should radiation and closure be handled in mixed layer models?
- What happens when the jump in equivalent potential temperature across cloud top becomes less than some critical value?

Boundary-layer convection is often driven by the upward virtual temperature flux from a warm underlying surface. However, the virtual temperature flux at the surface for the stratocumulus topped boundary is usually only weakly positive or even negative, and yet the boundary layer is quite turbulent. Thus, the cloud-topped boundary layers are often driven not by heating from below but by radiative cooling from above. There have been discussions centered around the relationship between the radiative flux and convective flux and entrainment at the top of the marine mixed layer. Lilly (1968) assumed that the radiative cooling was confined to the cloud-top jump condition so that radiation did not appear in the mixed layer heat budget. Deardorff (1976, 1981) and Kahn and Businger (1979) have questioned this assumption. Deardorff has suggested that only some of the radiative cooling should appear in the cloud-top jump condition, while Kahn and Bussinger have suggested that none should. In an effort to clear up this point, Lilly and Schubert (1980) have studied the effect of internal radiative cooling in a dry "cloud" model. These studies showed sensitivity to various specifications of the infrared cooling in the mixed layer

model. Observations of infrared radiation reported by Slingo et al. (1982b) showed that as the cloud becomes thicker, the infrared cooling becomes more confined to the cloud top. The convective motions take the form of cold downward moving plums, which are generated by the radiative loss from the cloud top. Since a simple mixed layer structure is assumed in these thermodynamic models and the convective fluxes are obtained through the closure assumptions, it is not clear whether the radiation controversy is simply conceptual or whether it has more practical implications.

An interesting feature of the stratocumulus study by Lilly (1968) concerns the stability of the cloud top against penetration by very dry upper air. Under certain conditions (Lilly, 1968; Randall,1980b; Deardorff,1980a; Nicholls and Turton, 1986) the mixture of unsaturated air from above the inversion with saturated air from the cloud layer may be negatively buoyant, forcing vertical mixing and entrainment at the inversion. The continuous entrainment is postulated to lead to the evaporation of the cloud layer. This process has been suggested as a mechanism for the breakup of stratocumulus clouds as well as the reason for the transition from the stratocumulus regime to the trade wind cumulus regime (Arakawa, 1975; Riehl, 1979). However, observations taken during the last fifteen years (as summarized in Chapter 2) do not seem to agree with this theoretical argument. There are more observations having large negative Θ jumps (which are unstable according to the theory) than positive Θ jumps, with the cloud remaining solid for quite a long time. Clearly, the problem of entrainment instability needs further investigation. Radiative cooling, latent heat exchange, turbulence and large scale subsidence are all involved in the entrainment process in the cloud-topped marine boundary layer. Moreover, the boundary layer turbulence budget depends crucially on these diabatic effects (radiative cooling and evaporative cooling). Thus a complete study of the entrainment problem requires consideration of the interaction of dynamical effects (turbulence), thermodynamical effects (diabatic forcings) and large scale mean conditions.

Tethered balloon observations have been used to study the small scale air motion and temperature in a layer of nocturnal stratocumulus in Great Britain by Roach et al. (1982), Caughey et al.(1982), Slingo et al.(1982b) and Caughey and Kitchen (1984). Their observations indicate a very sharp and intermittently turbulent entrainment interfacial layer (EIL)

with some evidence for a characteristic entrainment scale of about 10m. The entrainment can take place as radiatively or evaporatively cooled parcels are accelerated downward from the cloud top region, drawing in filaments of warm dry air from the EIL. These observations highlight the necessity for a model which adequately simulates the small scale cloud top processes pertinent to the entrainment instability problem.

Dynamical modeling with numerical techniques and resolution sufficient to simulate stratocumulus cloud-top processes can eliminate most of the assumptions made in the simpler models. If we are to better understand the role of radiation, the problem of turbulence closure, and the physics of cloud top entrainment instability, it would appear that we need to shift our emphasis away from the simpler models toward the dynamical models. This dissertation is an effort in this direction. We will try to answer the questions of entrainment instability and the importance of infrared radiation from the viewpoint of dynamical modeling. Thus, one objective of this thesis is to construct and run the simplest dynamical, shallow moist convection model which uses numerical techniques and resolution sufficient enough to simulate stratocumulus cloud-top processes. A two-dimensional Boussinesq moist model with Fourier-Chebyshev spatial discretization has been constructed to achieve this goal. Other objectives of our modeling study are to investigate the impact of the various infrared radiative forcings on the marine boundary layer dynamics as well as to study the problem of the entrainment instability.

In Chapter 2 the background for the investigation of the radiation and entrainment instability problems is presented. The two-dimensional Boussinesq moist model and its discretization are introduced in Chapter 3. Spatial discretization is accomplished by the Fourier-Chebyshev tau method. With this approach we hope to have higher accuracy with far fewer degrees of freedom and great efficiency when the desired accuracy is high enough. The fourth-order Runge-Kutta time integration scheme is used to increase the efficiency of the spectral method. Also described in Chapter 3 is the physics of condensation and evaporation. Chapter 4 contains the model parameters and soundings used in the study as well as some dry model test runs. The specification of the various infrared radiative forcings in the model are addressed in Chapter 5. Chapter 5 also covers the impact of these various forcings on the stratocumulus boundary layer dynamics. The results of the entrainment

instability study are presented in Chapter 6. Chapter 7 summarizes the principal conclusions of the dissertation and includes recommendations for future work.

CHAPTER II

BACKGROUND

2.1 Cloud top infrared radiative cooling

In his pioneering work on the cloud-topped marine boundary layer, Lilly(1968) disregarded the effects of the surface shear-generated turbulence but considered radiation off the cloud tops as an essential element in the maintenance of a mixed layer 500 to 1000 meters or more in thickness. He argued that "It would appear impossible for any observed combination of subsidence, convection, and shear turbulence to produce sufficient amounts of kinetic energy to maintain a 15-20 degree inversion at a height of 500-1000 meters without a radiatively effective cloud cover." Since the publication of Lilly's paper, this importance of cloud top infrared radiation loss has been generally accepted. There are numerous theoretical as well as observational studies concentrated not only on the longwave but also on the shortwave radiative properties of marine stratocumulus clouds.

Estimates of cloud shortwave absorption vary considerably and both Reynolds et al. (1975) and Stephens et al. (1978) report large values of absorption of solar radiation. Aircraft observations in the Joint Air-Sea Interaction experiment (JASIN) indicate that at midday the shortwave heating approximately cancels the longwave cooling of the cloud, despite the large cloud top cooling rate. Thus, a diurnal cycle of the stratocumulus layer is expected according to these measurements (Slingo et al. 1982a). However, there are great discrepancies between the observations and theoretical calculations of solar absorption in stratocumulus. The observations indicate the solar absorption can be as large as 20% while the theoretical calculations suggest only 6% (Wiscombe et al. 1984). Several mechanisms have been proposed to reconcile the differences between theory and measurement. Grassl (1975) showed that the presence of aerosols in clouds can produce increased absorption. Since many of the measurements showing anomalous absorption were taken in clouds far

from known pollution sources, the question remains as to whether there would be sufficient aerosol present to significantly influence cloud absorption. Welch et al. (1980) and Wiscombe et al. (1984) performed calculations which suggest that excess absorption of solar radiation may be due to precipitation or very large droplets in the clouds, although Twomey (1978) pointed out that departures of the cloud from stratiform geometry may invalidate the derivation of the absorption from the observed fluxes, because some radiation would be lost through the sides of the cloud. This particular issue of the large observed solar absorption in clouds (Absorption Paradox) is still an open question. Therefore, only the interaction between dynamics and infrared radiation will be considered in this thesis.

The studies of the cloud top infrared radiation indicate a good agreement between the measured longwave fluxes and cooling rates and theoretical calculations (e.g. Stephens et al., 1978; Slingo et al., 1982b; Kuo, 1983; Fouquart 1985). The typical cloud top cooling is about 5-10 K hr^{-1} and covers the top 50-100 meters of the cloud. In addition, the effective emissivity of the cloud can be accurately parameterized by the liquid water path (Stephens et al., 1978; Slingo et al., 1982b). Tethered balloon observations have been used by Slingo et al. (1982b) to study cloud microphysics and infrared radiation effects in a layer of nocturnal stratocumulus. Although these observations were taken over land (Cardington, England), they have many characteristics in common with marine stratocumulus. The three panels of Fig. 2.1 (from Slingo et al.1982b) show the vertical profiles of the net upward infrared flux and the cooling rate taken from the tethered balloon observations on three separate nights. They are arranged in order of increasing cloud thickness. We observe from Fig. 2.1 that as the clouds become thicker the infrared cooling becomes more confined to the cloud top. Moreover, the magnitude of the cooling varies as the cloud thickness varies. Thus, the infrared radiative forcing in the marine boundary layer is very sensitive to the cloud liquid water content. Aircraft measurements in stratocumulus clouds off the east coast of Australia such as reported by Stephens and Platt (1987) indicate the horizontal inhomogeneity of stratocumulus clouds. The fractional deviation of cloud liquid water content as a function of the normalized in-cloud depth for three of the flights are plotted in Fig. 2.2. The fractional deviation here is defined as the ratio of the standard deviation divided by its mean and all the horizontal flight paths are 16 km long. Note that the

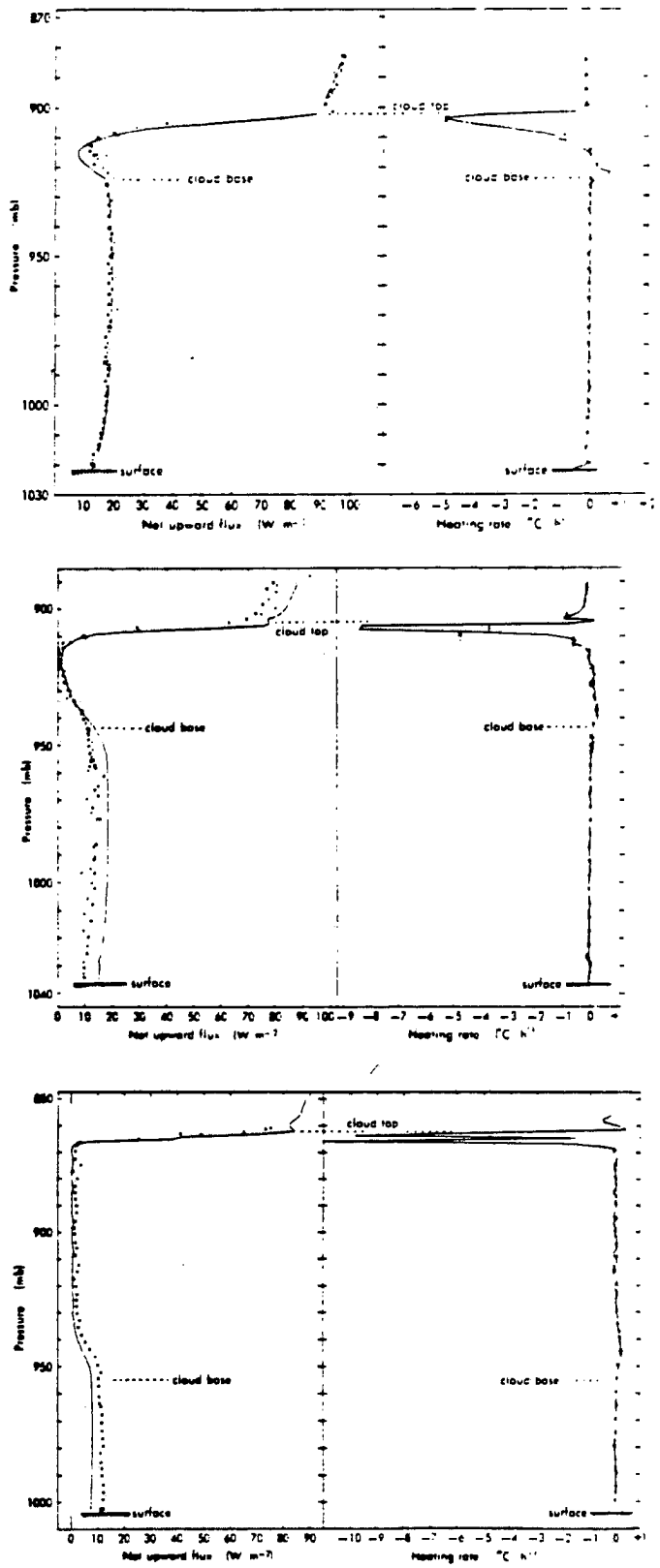

Figure 2.1. Comparison of the observed (dotted lines) and theoretical (solid lines) net infrared fluxes and cooling rates. The three measurements are arranged in order of increasing cloud thickness.

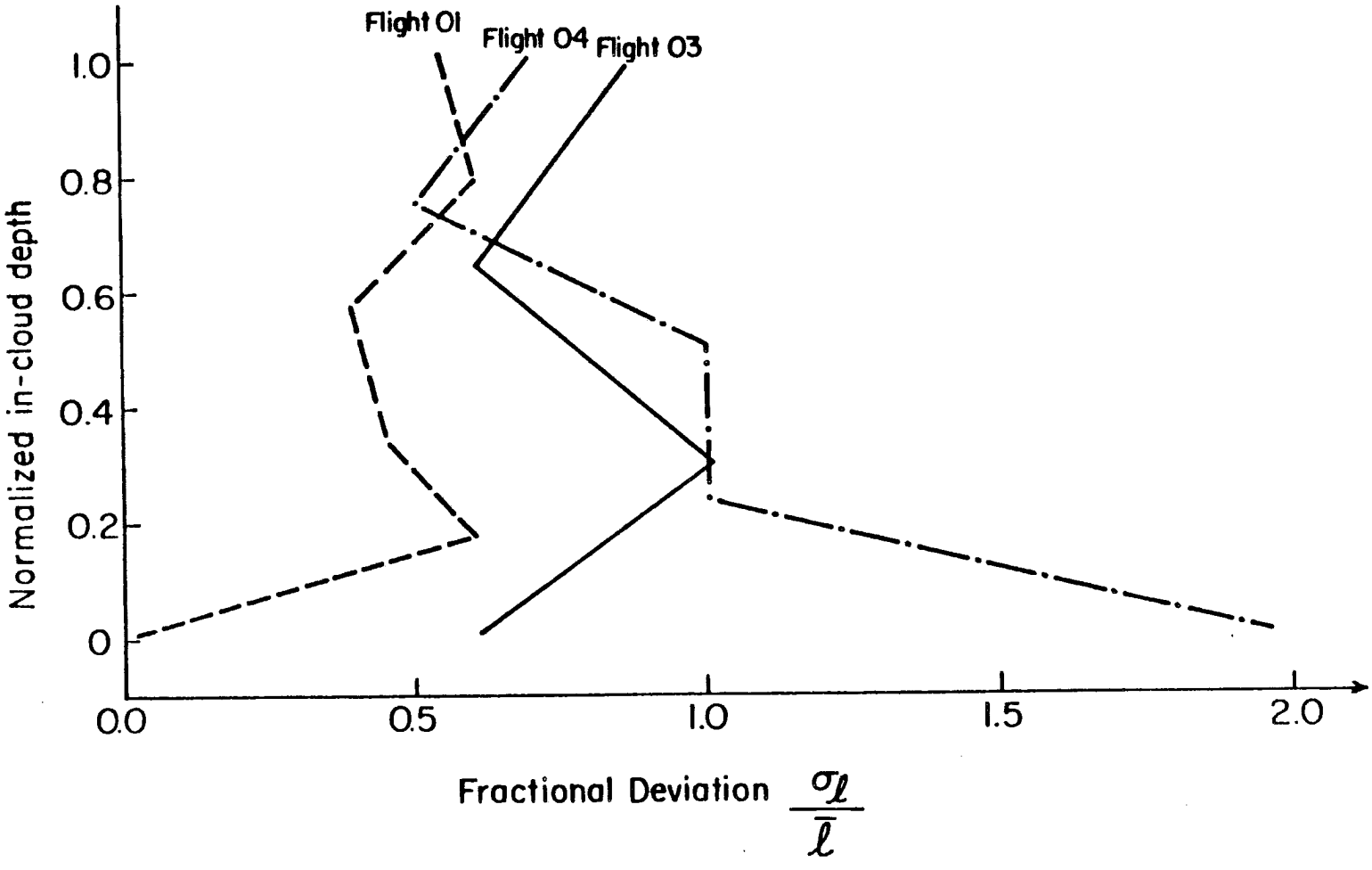

Figure 2.2. The fractional deviation of cloud liquid water as a function of the normalized in-cloud depth. The fractional deviation is defined as the ratio of the standard deviation divided by its mean. The horizontal flight paths are 16 km long.

fractional deviation of the cloud liquid water is large throughout the whole cloud layer. The results in Fig. 2.2 suggest that cloud liquid water is highly variable along a given level inside the cloud.

The implications of the observations presented in Figs. 2.1 and 2.2 are that the cloud top radiative cooling is likely to undergo significant horizontal as well as vertical variability which will be principally governed by the variability of cloud liquid water. Since the infrared radiation is the driving force of the boundary layer, one might then wonder how the boundary layer dynamics will vary according to these different spatial distributions of radiative cooling. In addition, because the horizontal variability of the optical medium (stratocumulus) is as extreme as the vertical variability, the usefulness of the classical one-dimensional plane parallel radiative transfer theory in a fine resolution dynamical model is questionable. On the other hand, the need for more complicated radiative transfer calculations or observations to take the horizontal variability of stratocumulus into account will depend on how the boundary layer dynamics are affected by the various spatial distributions of radiative cooling. We will try to understand the detailed behavior of stratocumulus under various infrared radiative forcings in the present dissertation.

2.2 Entrainment instability

2.2.1 Lilly's hypothesis

In a paper which has become a classic, Lilly (1968) constructed a simple model of the shallow, cloud-topped boundary layers which form under strong subsidence inversions associated with subtropical and midlatitude high pressure systems. Lilly argued that one of the theoretical requirements for applicability of his model was the stability of cloud top against penetration by the very dry upper air mass. According to his argument, cloud top instability could be understood as follows: "If a parcel of the upper air is introduced into the cloud layer and mixed by turbulence, evaporation of cloud droplets into the dry parcel will reduce its temperature. If the mixed parcel reaches saturation at a colder temperature than that of the cloud top it will be negatively buoyant and can then penetrate freely into the cloud mass. In such a case the evaporation and penetration process will occur spontaneously and increase unstably until the cloud is evaporated." Since the condition for

no change in temperature upon evaporative mixing (while maintaining saturation) is that the equivalent potential temperatures $\Theta = \theta + \frac{L}{C_p} q$ of the wet and dry layers be equal, Lilly assumed that for stability of a cloud layer the temperature inversion must be sufficiently strong so that the equivalent potential temperature remains constant or increases upward at cloud top. Defining the jump operator Δ as the above-cloud value minus the in-cloud value, this condition for stability can be written

$$\Delta\Theta > 0. \tag{2.1}$$

Near the end of his paper Lilly presented three radiosonde soundings taken in August 1962 at Oakland, California during stratus overcast conditions. The soundings showed that the warm, dry air above the inversion had an equivalent potential temperature about 5 to 9K higher than the cool, moist boundary layer air. Lilly concluded that the prediction of a positive $\Delta\Theta$ "seems to agree with the observational data."

Although the mixed layer model equation set proposed by Lilly took into account the effects of water vapor and liquid water on buoyancy, his cloud top stability analysis did not. Randall (1980b) and Deardorff (1980a) included these additional buoyancy effects, and since then several discussions and elaborations have appeared, e.g. Hanson (1981), Betts (1982, 1983), Albrecht et al. (1985), Rogers and Telford (1986), Nicholls and Turton (1986). Together these constitute a thermodynamic theory of cloud top entrainment instability, which we shall now summarize.

2.2.2 Thermodynamic theory of cloud top entrainment instability

Consider a unit mass mixture consisting of χ mass units of the warm dry air just above the inversion and $1 - \chi$ mass units of the cool moist air just below the inversion. Using the subscripts a and b to denote respectively the above inversion parcel and the below inversion parcel, we obtain

$$\Theta = \chi\Theta_a + (1-\chi)\Theta_b = \Theta_b + \chi\Delta\Theta \ , \tag{2.2}$$

$$r = \chi r_a + (1-\chi) r_b = r_b + \chi\Delta r \ , \tag{2.3}$$

for the equivalent potential temperature Θ and the total water mixing ratio r of the mixed parcel. If we also know the height z of the mixed parcel, we can use the Boussinesq

version of the theory of moist convection (Ogura and Phillips, 1962) to obtain the potential temperature θ, the water vapor mixing ratio q, the saturation water mixing ratio q^* and the liquid water mixing ratio l from the four equations

$$\theta = \Theta - \frac{L}{c_p} q \,, \tag{2.4}$$

$$q^* = \bar{q}^* \exp\left\{ \frac{L}{R_v \theta_0} \left(\frac{\theta - \theta_0}{\theta_0} \right) \right\} \,, \tag{2.5}$$

$$(q, l) = \left\{ \begin{array}{ll} (q^*, r - q^*) & r > q^* \\ (r, 0) & r \leq q^* \end{array} \right\} \,. \tag{2.6,2.7}$$

Here L is the constant latent heat of condensation, R_v the gas constant for water vapor, θ_0 a constant reference potential temperature and $\bar{q}^*$ the known function

$$\bar{q}^*(z) = \frac{m_v}{m_a} \frac{e^*(\bar{T}(z))}{p_0} \,,$$

where m_v and m_a are the molecular weights for water vapor and dry air, $p_0 = 100$ kPa, and $\bar{T}(z) = \theta_0 - gz/c_p$. If θ_0 is chosen to be 15° C and Teten's formula is used for the saturation vapor pressure e^*, then $\bar{q}^*(z)$ can be computed. To actually solve (2.4)–(2.7) for θ, q, q^*, l from given z, Θ, r we can proceed as follows. First assume the second alternative in (2.6,2.7), i.e. $r \leq q^*$ and $(q, l) = (r, 0)$, so that θ can be computed from (2.4) with q replaced by r. Next compute q^* from (2.5) and check to see if $r \leq q^*$ as originally assumed. If a contradiction is reached, we conclude that $r \geq q^*$; we must then iteratively adjust θ, q (which now equals q^*) and l until we obtain the solution of (2.4), (2.5) and the first alternative in (2.6,2.7). A rapidly convergent refined Newton scheme for doing this is discussed in Chapter 3. After solving (2.4)–(2.7) we can compute the mixed parcel's virtual potential temperature ϑ from

$$\vartheta = \theta + \theta_0(\delta q - l) \,, \tag{2.8}$$

where $\delta = 0.608$. From a comparison of ϑ with ϑ_b we can predict whether the mixed parcel is likely to rise or sink. Thus, (2.2)–(2.8) form the basis for the thermodynamic theory of cloud top entrainment instability.

We now attempt to find an analytical approximation for the buoyancy $\vartheta - \vartheta_b$ when $\chi \leq \hat{\chi}$, with $\hat{\chi}$ denoting the mixing where the liquid water content of the mixed parcel

vanishes. Using (2.3) and (2.8) we obtain

$$\vartheta - \vartheta_b = \theta - \theta_b + \theta_0[(1+\delta)(q - q_b) - \chi\Delta r] \,. \tag{2.9}$$

For $\chi \leq \hat{\chi}$, q and q_b are saturation values given in terms of θ and θ_b by (2.5). If we approximate the right hand side of (2.5) by the first two terms in its Taylor series expansion about $\theta = \theta_b$ we obtain

$$\frac{L}{C_p}(q^* - q_b^*) = \gamma(\theta - \theta_b) = \frac{\gamma}{1+\gamma}(\Theta - \Theta_b) \,, \tag{2.10}$$

where $\gamma = \frac{L}{C_p}\frac{\partial q^*}{\partial \theta}$. Using (2.2) and (2.10) in (2.9) we obtain

$$\frac{\vartheta - \vartheta_b}{\theta_0} = \chi(\frac{C_p}{Lk}\Delta\Theta - \Delta r) \,, \tag{2.11}$$

where

$$k = \frac{(1+\gamma)\frac{C_p\theta_0}{L}}{1 + (1+\delta)\gamma\frac{C_p\theta_0}{L}} \approx 0.23.$$

If the term within the parentheses of (2.11) is negative, all mixtures with $0 < \chi \leq \hat{\chi}$ will be negatively buoyant. On the other hand, if the term within the braces is positive, we conclude that there will be no mixture which is negatively buoyant. Thus, according to the thermodynamic theory of entrainment instability,

$$\Delta\Theta > k\frac{L}{C_p}\Delta r \tag{2.12}$$

is the condition for stability of a cloud-topped mixed layer.

The inequality (2.12) divides the ($\Delta\Theta$, Δr) plane into the stable and unstable regions shown in Fig. 2.3. If the thermodynamic theory of entrainment instability is correct, we should not observe persistent atmospheric states with $\Delta\Theta$,Δr combinations lying to the left of the critical curve in Fig. 2.3. We shall now show that this prediction of the thermodynamic theory of entrainment instability is at odds with observations.

2.2.3 Observations

A substantial observational data base on the cloud-topped boundary layer has accumulated over the last ten years. We can divide most of this data base into two parts: aircraft and tethered balloon data taken along and off the California coast in the subtropical marine stratocumulus regime of summer and fall; and aircraft, tethered balloon and shipboard

sounding data taken in midlatitude stratocumulus over England and over the surrounding waters of the North Atlantic and the North Sea. This data base is described in the eleven papers summarized in Table 2.1. We have surveyed these papers with the objective of documenting the $(\Delta\Theta, \Delta r)$ values of soundings through persistent stratocumulus decks. The results of this survey are given by the 48 coded symbols shown in Fig. 2.3, with the solid symbols for the subtropical case and the open symbols for the midlatitude case. The most surprising result is that two thirds (32 out of 48) of the points violate the condition (2.12). The worst offenders are the subtropical cases, especially those taken southwest of San Diego during DYCOMS (Dynamics and Chemistry of Marine Stratocumulus; Weaver, 1987). As examples consider the points for which $(\Delta\Theta, \Delta r) = (-11\ \text{K}, -7.5\ \text{g kg}^{-1})$ and $(-12\ \text{K}, -8\ \text{g kg}^{-1})$. The Θ profiles for these cases (17:57 and 22:33 GMT 9 August 1985, respectively) are shown in Fig. 2.4. High resolution GOES images at 18:03 and 23:33 GMT from the CSU Satellite Earthstation are shown in Fig. 2.5, confirming the persistence of this extensive cloud deck.

2.2.4 Towards a dynamical theory of cloud top entrainment instability

Why should the predictions of the seemingly plausible thermodynamic theory of cloud top entrainment instability be so much at odds with observations ? Our belief is that the theory is neither closed nor sufficient to predict the entrainment instability. For (2.12) to be valid, χ must be restricted in range so that the mixed parcel remains saturated. Since there is no equation determining χ, (2.12) may not be true if the value of $\hat{\chi}$ in the cloud-topped marine boundary layer is small. A closed thermodynamic theory requires additional knowledge about χ. However, the theory may still be incapable of predicting the cloud top entrainment instability even with additional knowledge about χ. The radiative cooling near cloud top and latent heat exchange inside the cloud not only influence the entrainment but also regulate the turbulence and thus affect the χ value. We believe that a closed argument requires that (2.2) and (2.3) be replaced by the conservation laws for Θ and r while the χ information be given by the momentum equations. With this approach, subsidence and radiative cooling effects can be part of the theory and interact freely with the dynamics. Unfortunately, this makes the mathematical problem complicated enough

Table 2.1. The data base for figure 2.3.

	Location	Time	Comments
Subtropical			
Albrecht et al. (1985)	near 35° N, 125° W	5, 13, 17 June 1976	Three NCAR Electra flights from NASA Ames
Hanson(1984)	near 29° N, 122° W	27 June 1981	NOAA WP-3D flights from San Diego
Rogers and Telford(1986)	about 100 km west of San Francisco	25 August 1982	Seven of eight NCAR Queen Air soundings showed $\Delta\Theta < 0$. Soundings S7 and S9 are shown in Fig. 2.3.
Weaver (1987)	about 500 km southwest of San Diego	30 July to 21 August 1985	Ten NCAR Electra flights from San Diego
Gerber(1986)	San Nicolas Island, California	18–29 October, 1984	Naval Research Laboratory tethered balloon flights into stratocumulus overcast (flights 12, 17, 18)
Midlatitude			
Slingo et al. (1982a)	near 60° N, 10° W	8 August 1978	Three aircraft during JASIN
Taylor et al. (1983)	Ship triangle centered at 59° N, 12° W	31 August 1978	Radiosondes at 1 to 2 hour intervals during JASIN
Nicholls (1984)	North Sea, off Yorkshire coast	22 July 1982	MRF C-130 data taken in extensive 450 m thick stratocumulus layer
Nicholls and Leighton (1986)	UK coastal waters, primarily North Sea	27 April, 29 July 1982, 15 December 1982, 2, 16 November 1983	Other MRF C-130 flights, some into layers decoupled from the service
Slingo et al. (1982b)	Cardington, U.K.	26-27 October 1977, 15 January 1978	Tethered balloon flights into nocturnal stratocumulus

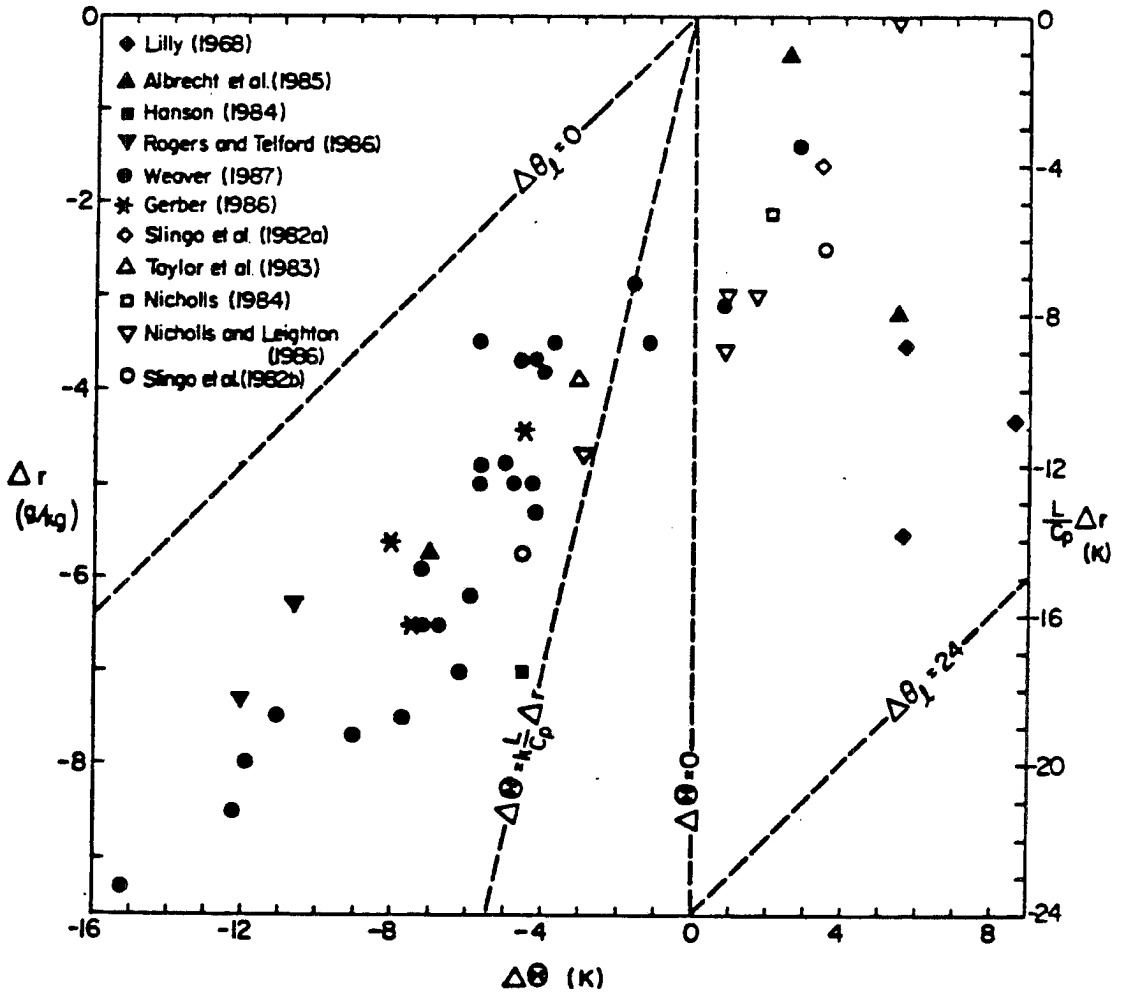

Figure 2.3. The $\Delta\Theta$, Δr plane, with the Lilly critical curve ($\Delta\Theta = 0$) and the Randall-Deardorff critical curve ($\Delta\Theta = k\frac{L}{C_p}\Delta r$). Observational data are indicated by the coded symbols, with solid symbols for subtropical cases and open symbols for midlatitude cases. About two-thirds of the observations are at odds with the predictions of the thermodynamic theory of cloud top entrainment instability.

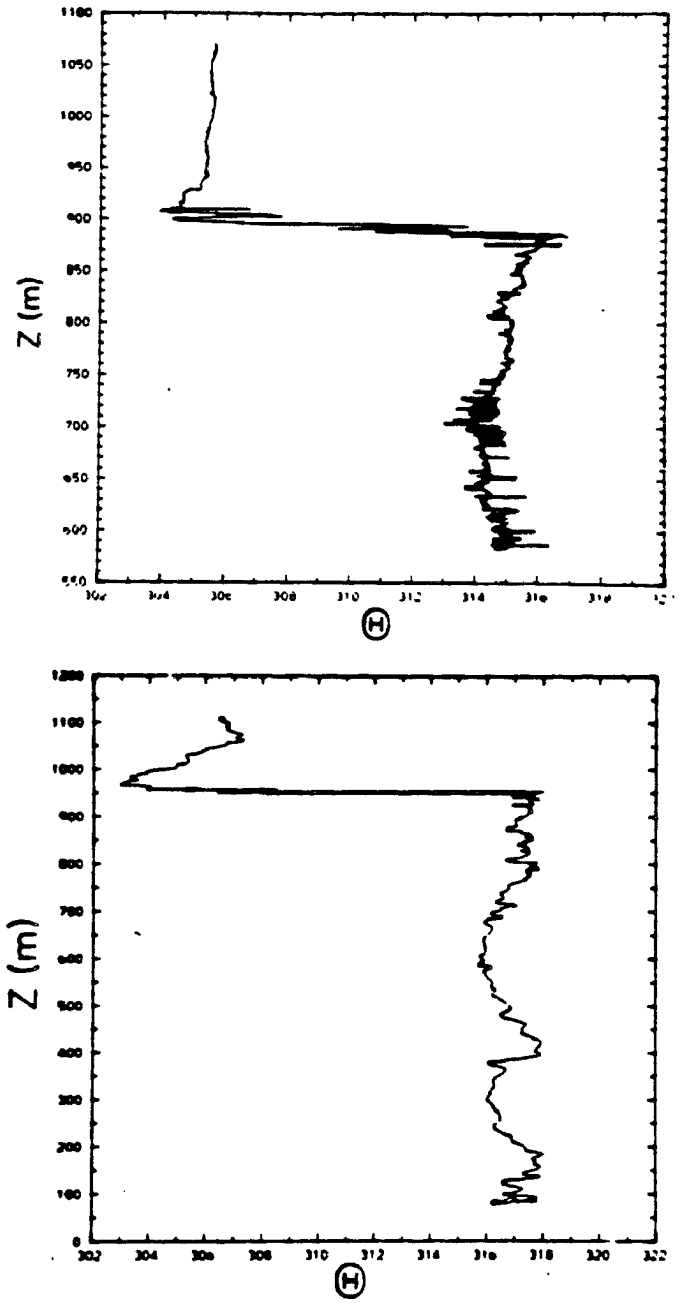

Figure 2.4. The Θ soundings at 1757 (upper) and 2233 (lower) GMT 9 August 1985 in the DYCOMS observational region.

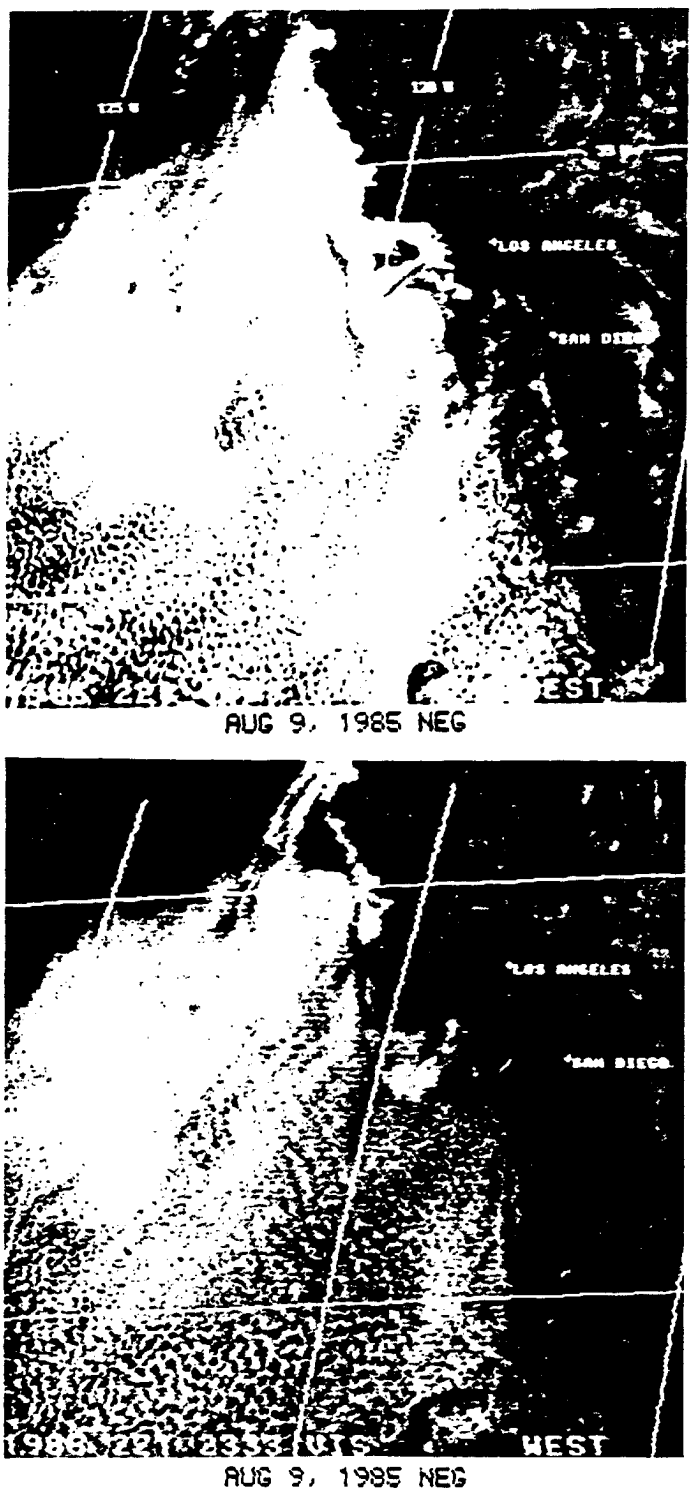

Figure 2.5. GOES visible images for 1803 (upper) and 2333 (lower) GMT 9 August 1985. The box indicates the DYCOMS observational region.

that analytical progress is difficult. This leaves numerical simulation as the only reasonable alternative. In the remainder of this thesis we shall describe the simplest possible two-dimensional dynamical formulation which can replace (2.2)–(2.8). We shall then compare numerical simulations based on various initial conditions, some of which satisfy (2.12) and some of which violate (2.12).

CHAPTER III

TWO-DIMENSIONAL BOUSSINESQ MODEL

3.1 Governing equations

The starting point for our model is the formal scale analysis of Ogura and Phillips (1962), who derived the anelastic (or soundproof) equations under the assumptions that the percentage range of potential temperature is small and the time scale is set by the Brunt-Väisälä frequency. The anelastic equations reduce to the Boussinesq equations under the additional assumption that the vertical scale of motion is small compared to the depth of an isentropic atmosphere. Since the above assumptions are justified for the marine boundary layer problem, we shall use Ogura and Phillips' Boussinesq equations for shallow moist convection. If the flow is constrained to be two-dimensional we can write these equations in the vorticity/streamfunction form

$$\left\{ \begin{array}{c} \dfrac{\partial^2 \psi}{\partial x^2} + \dfrac{\partial^2 \psi}{\partial z^2} = \varsigma \\ \psi(x,0,t) = \psi(x,H,t) = 0 \end{array} \right\} , \tag{3.1}$$

$$\frac{\partial \varsigma}{\partial t} + \frac{\partial}{\partial x}\left(-\frac{\partial \psi}{\partial z}\varsigma\right) + \frac{\partial}{\partial z}\left(\frac{\partial \psi}{\partial x}\varsigma\right) - \frac{g}{\theta_0}\frac{\partial \vartheta}{\partial x} = \mathcal{F} , \tag{3.2}$$

$$\frac{\partial \Theta}{\partial t} + \frac{\partial}{\partial x}\left(-\frac{\partial \psi}{\partial z}\Theta\right) + \frac{\partial}{\partial z}\left(\frac{\partial \psi}{\partial x}\Theta\right) = \mathcal{G} + \mathcal{Q} , \tag{3.3}$$

$$\frac{\partial r}{\partial t} + \frac{\partial}{\partial x}\left(-\frac{\partial \psi}{\partial z}r\right) + \frac{\partial}{\partial z}\left(\frac{\partial \psi}{\partial x}r\right) = \mathcal{H} + \mathcal{R} , \tag{3.4}$$

$$\theta = \Theta - \frac{L}{c_p} q , \tag{3.5}$$

$$q^* = \bar{q}^* \exp\left\{ \frac{L}{R_v \theta_0} \left(\frac{\theta - \theta_0}{\theta_0} \right) \right\} , \tag{3.6}$$

$$(q,l) = \left\{ \begin{array}{ll} (q^*, r - q^*) & r > q^* \\ (r,0) & r \leq q^* \end{array} \right\} , \tag{3.7,3.8}$$

$$\vartheta = \theta + \theta_0(\delta q - l) . \tag{3.9}$$

This is a closed system in ψ, ς, θ, Θ, ϑ, q, q^*, l and r, where ψ and ς are the streamfunction and vorticity, θ the potential temperature, Θ the equivalent potential temperature, ϑ the virtual potential temperature, q and q^* the mixing ratio and saturation mixing ratio of water vapor, l the mixing ratio of liquid water, and r the mixing ratio of total water (vapor plus liquid). The unconventional notation for equivalent potential temperature and virtual potential temperature has been introduced in order to avoid excessive subscripts in the next section. The symbols $\mathcal{F}$, $\mathcal{G}$ and $\mathcal{H}$ represent small scale diffusion processes, $\mathcal{R}$ the convergence of the sea surface total water flux and $\mathcal{Q}$ the infrared radiative loss plus the convergence of the sea surface equivalent potential temperature flux. The forcing functions $\mathcal{Q}$ and $\mathcal{R}$ will be discussed in chapters 4 and 5. In (3.6) L is the constant latent heat of condensation, R_v the gas constant for water vapor, and $\bar{q}^*$ the known function

$$\bar{q}^*(z) = \frac{m_v}{m_a} \frac{e^*(\bar{T}(z))}{p_0} ,$$

where m_v and m_a are the molecular weights for water vapor and dry air, $p_0 = 100$ kPa, and $\bar{T}(z) = \theta_0 - gz/c_p$. If θ_0 is chosen to be 15° C and Teten's formula is used for the saturation vapor pressure e^*, then $\bar{q}^*(z)$ has the form shown in Fig. 3.1. Finally we note that the effects of both water vapor and liquid water on buoyancy are included in (3.9), with $\delta = 0.608$, and that after prediction of Θ and r from (3.3) and (3.4), iteration is required to diagnose θ, q, q^*, and l from (3.5)–(3.8).

We shall solve (3.1)–(3.9) on the domain $0 \leq x \leq L, 0 \leq z \leq H$, with the assumption that all variables are periodic in x and $\psi = 0$ on $z = 0, H$. In the following section we discuss an accurate spectral method (Fourier-Chebyshev tau method) for solving the system (3.1)–(3.9).

3.2 Space and time discretization

The strong gradients of temperature and moisture which are produced in marine boundary layer convection place great demands on spatial discretization schemes used in simulation models. In the present work we have used a scheme which is spectral in both the horizontal and vertical directions. In the horizontal, Fourier basis functions are used so that the periodicity is built into each basis function. In the vertical, Chebyshev polynomial

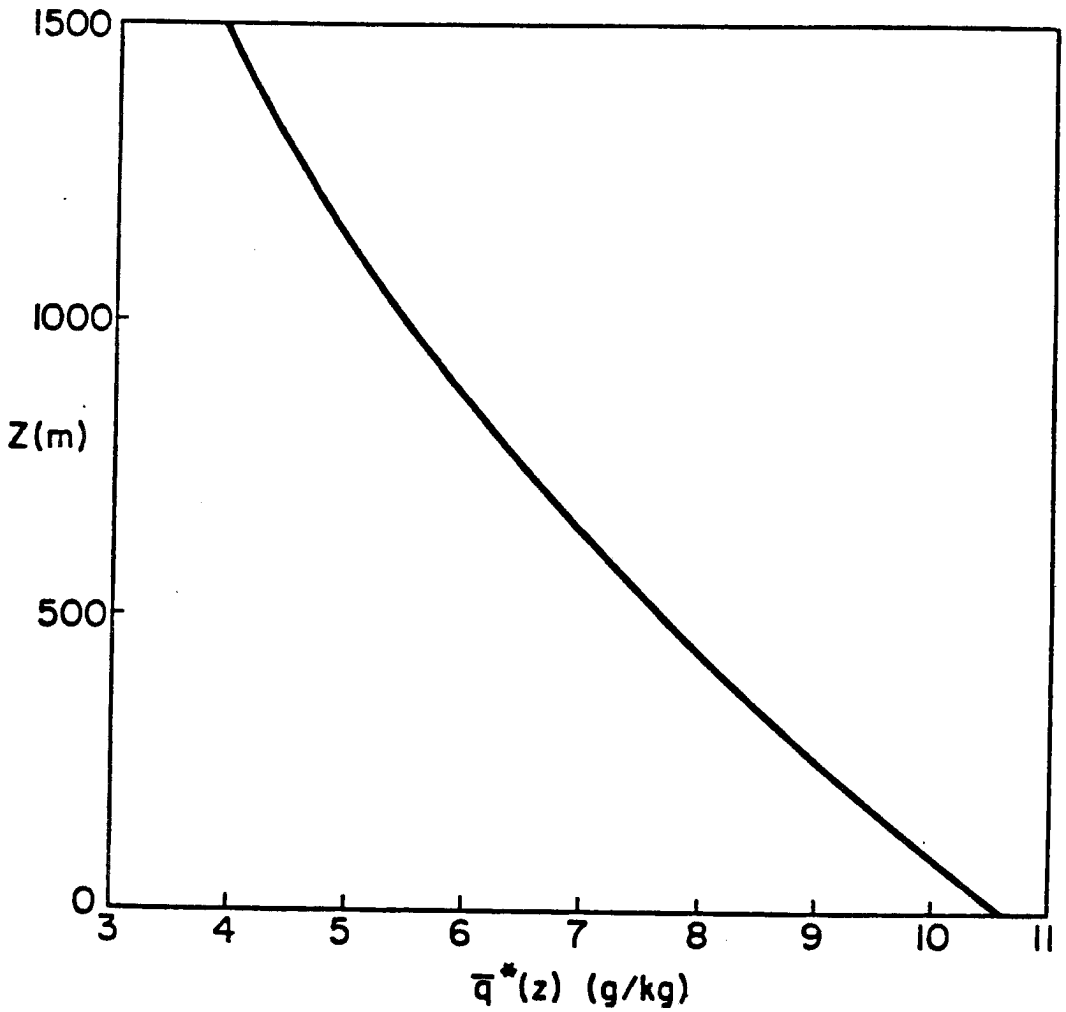

Figure 3.1. The $\bar{q}^*(z)$ as a function of height for θ_0 is 15° C.

basis functions are used; the upper and lower boundary conditions are not satisfied by each basis function, but rather by the series as a whole.

The dependent variables ψ, ς, Θ, ϑ and r are approximated by the series expansions

$$\begin{bmatrix} \psi(x,z,t) \\ \varsigma(x,z,t) \\ \Theta(x,z,t) \\ \vartheta(x,z,t) \\ r(x,z,t) \end{bmatrix} = \sum_{m=-M}^{M} \sum_{n=0}^{N} \begin{bmatrix} \hat{\psi}_{mn}(t) \\ \hat{\varsigma}_{mn}(t) \\ \hat{\Theta}_{mn}(t) \\ \hat{\vartheta}_{mn}(t) \\ \hat{r}_{mn}(t) \end{bmatrix} T_n(z') e^{2\pi i m x/L} , \tag{3.10}$$

where the $T_n(z')$ are the Chebyshev polynomials defined on the interval $-1 \le z' \le 1$ by $T_n(z') = \cos(n\phi)$ with $z' = 2z/H - 1 = \cos\phi$. Let us define the Fourier-Chebyshev inner product of two functions $f(x,z)$ and $g(x,z)$ as

$$\langle f,g \rangle = \frac{1}{L} \int_{-1}^{1} \int_{0}^{L} \frac{f(x,z) g^*(x,z)}{(1-z'^2)^{1/2}} \, dx \, dz' , \tag{3.11}$$

where the star denotes complex conjugate. The spectral coefficient $\hat{\psi}_{mn}(t)$ is given by

$$\hat{\psi}_{mn}(t) = \frac{2}{\pi c_n} \left\langle \psi(x,z,t), T_n(z') e^{2\pi i m x/L} \right\rangle \tag{3.12}$$

with $c_n = \left\{ \begin{array}{ll} 2 & n=0 \\ 1 & n>0 \end{array} \right\}$. Similar relations hold for $\hat{\varsigma}_{mn}(t)$, $\hat{\Theta}_{mn}(t)$, $\hat{\vartheta}_{mn}(t)$ and $\hat{r}_{mn}(t)$. Equation (3.12) is the transformation from physical space to Fourier-Chebyshev spectral space and (3.10) is the transformation back.

The coefficients in (3.10) are determined by requiring the residual in (3.2), (3.3) and (3.4) to be orthogonal to all the basis functions $T_n(z') e^{2\pi i m x/L}$ ($-M \le m \le M$ and $0 \le n \le N$), the residual in the Poisson equation (3.1) to be orthogonal to all the basis functions except those for which $n = N-1, N$, and the boundary conditions on ψ to be satisfied by the series as a whole. Thus, with the nonlinear terms defined by

$$\begin{aligned} A &= -\tfrac{\partial \psi}{\partial z} \varsigma, \quad B = \tfrac{\partial \psi}{\partial z} \varsigma , \\ C &= -\tfrac{\partial \psi}{\partial z} \theta, \quad D = \tfrac{\partial \psi}{\partial z} \theta , \\ E &= -\tfrac{\partial \psi}{\partial z} r, \quad F = \tfrac{\partial \psi}{\partial z} r , \end{aligned} \tag{3.13}$$

the tau equations are

$$\left\{ \begin{array}{l} \frac{4}{H^2 c_n} \sum\limits_{\substack{p=n+2 \\ p+n \text{ even}}}^{N} p(p^2-n^2) \hat{\psi}_{mp} - \left(\frac{2\pi m}{L}\right)^2 \hat{\psi}_{mn} = \hat{\varsigma}_{mn} \quad (n = 0,1,2,\cdots,N-2) \\ \sum\limits_{p=0}^{N} (-1)^p \hat{\psi}_{mp} = 0 \\ \sum\limits_{p=0}^{N} \hat{\psi}_{mp} = 0 \end{array} \right\} \tag{3.14}$$

$$\frac{d\hat{\zeta}_{mn}}{dt} + \hat{A}^{(1,0)}_{mn} + \hat{B}^{(0,1)}_{mn} - \frac{g}{\theta_0}\hat{\vartheta}^{(1,0)}_{mn} = \hat{\mathcal{F}}_{mn} \ , \tag{3.15}$$

$$\frac{d\hat{\Theta}_{mn}}{dt} + \hat{C}^{(1,0)}_{mn} + \hat{D}^{(0,1)}_{mn} = \hat{\mathcal{G}}_{mn} + \hat{\mathcal{Q}}_{mn} \ , \tag{3.16}$$

$$\frac{d\hat{r}_{mn}}{dt} + \hat{E}^{(1,0)}_{mn} + \hat{F}^{(0,1)}_{mn} = \hat{\mathcal{H}}_{mn} + \hat{\mathcal{R}}_{mn} \ , \tag{3.17}$$

where $\hat{A}^{(1,0)}_{mn}$, $\hat{C}^{(1,0)}_{mn}$, $\hat{E}^{(1,0)}_{mn}$, $\hat{\vartheta}^{(1,0)}_{mn}$ are the spectral coefficients of $\partial A/\partial x$, $\partial C/\partial x$, $\partial E/\partial x$, $\partial \vartheta/\partial x$ and $\hat{B}^{(0,1)}_{mn}$, $\hat{D}^{(0,1)}_{mn}$, $\hat{F}^{(0,1)}_{mn}$ are the spectral coefficients of $\partial B/\partial z$, $\partial D/\partial z$, $\partial F/\partial z$. Likewise $\hat{\mathcal{Q}}_{mn}$, $\hat{\mathcal{R}}_{mn}$, $\hat{\mathcal{F}}_{mn}$, $\hat{\mathcal{G}}_{mn}$ and $\hat{\mathcal{H}}_{mn}$ are the spectral coefficients of $\mathcal{Q}$, $\mathcal{R}$, $\mathcal{F}$, $\mathcal{G}$ and $\mathcal{H}$. Some of the details in the derivation of (3.14)–(3.17) are given in Appendix A. The relation between $\hat{A}^{(1,0)}_{mn}$ and $\hat{A}_{mn}$ (the spectral coefficient of A) is

$$\hat{A}^{(1,0)}_{mn} = i\left(\frac{2\pi m}{L}\right)\hat{A}_{mn} \ , \tag{3.18}$$

with similar relations for $\hat{C}^{(1,0)}_{mn}$, $\hat{E}^{(1,0)}_{mn}$, and $\hat{\vartheta}^{(1,0)}_{mn}$. As discussed in the appendix the relation between $\hat{B}^{(0,1)}_{mn}$ and $\hat{B}_{mn}$ (the spectral coefficient of B) is

$$\hat{B}^{(0,1)}_{mn} = \frac{4}{Hc_n} \sum_{\substack{p=n+1 \\ p+n \text{ odd}}}^{N} p\hat{B}_{mp} \ , \tag{3.19}$$

with similar relations for $\hat{D}^{(0,1)}_{mn}$ and $\hat{F}^{(0,1)}_{mn}$. Although the spectral evaluation of z derivatives by (3.19) looks at first sight more difficult than the spectral evaluation of x derivatives by (3.18), such is not the case. Equation (3.19) yields the (backward) recurrence formula

$$c_{n-1}\hat{B}^{(0,1)}_{m,n-1} - \hat{B}^{(0,1)}_{m,n+1} = \frac{4}{H}n\hat{B}_{m,n} \quad (n = 1, 2, \cdots, N-1) \tag{3.20}$$

with the starting values $\hat{B}^{(0,1)}_{m,N+1} = \hat{B}^{(0,1)}_{m,N} = 0$. For fixed m, the use of (3.20) allows the N values of $\hat{B}^{(0,1)}_{mn}$ to be computed in $O(N)$ operations. The transform method (Orszag, 1970; Eliasen et al., 1970) is used in computing the spectral coefficients $\hat{A}_{mn}$, $\hat{B}_{mn}$, $\hat{C}_{mn}$, $\hat{D}_{mn}$, $\hat{E}_{mn}$ and $\hat{F}_{mn}$. To eliminate aliasing error, $3M$ by $\frac{3}{2}N$ points are needed in the physical domain.

The subgrid diffusion process in the model is handled in spectral space by adding a second- and fourth-order linear diffusion term to the right hand side of the spectral coefficient equations. The second-order diffusion term is used in the x direction and a more

scale-selective fourth-order diffusion is used in the z direction. This spectral subgrid diffusion is given by

$$\begin{aligned}
\hat{\mathcal{F}}_{mn} &= -k_x \left(\tfrac{2\pi m}{L}\right)^2 \hat{\zeta}_{mn} - k_z \left(\tfrac{2\pi n}{H}\right)^4 \hat{\zeta}_{mn} , \\
\hat{\mathcal{G}}_{mn} &= -k_x \left(\tfrac{2\pi m}{L}\right)^2 \hat{\Theta}_{mn} - k_z \left(\tfrac{2\pi n}{H}\right)^4 \hat{\Theta}_{mn} , \\
\hat{\mathcal{H}}_{mn} &= -k_x \left(\tfrac{2\pi m}{L}\right)^2 \hat{r}_{mn} - k_z \left(\tfrac{2\pi n}{H}\right)^4 \hat{r}_{mn} .
\end{aligned} \tag{3.21}$$

In the numerical time integration of the above equations, we must solve (3.14) at each time step. For a given m ($-M \leq m \leq M$) we regard (3.14) as a linear algebraic system in the $N+1$ unknowns $\hat{\psi}_{mn}$ ($0 \leq n \leq N$), with known right hand side $\hat{\zeta}_{mn}$. The matrix structure of this linear system is upper triangular except for the last two rows, which come from the boundary conditions. There are many possible ways to solve (3.14), two of which are discussed by Gottlieb and Orszag (1977, page 119–120). Because (3.14) holds for each m separately, direct methods are a reasonable alternative, a situation which does not exist when Chebyshev expansions are used in both directions.

Asymptotic arguments (Fulton and Schubert, 1987) demonstrate that when enough accuracy is desired, Chebyshev spectral methods are more efficient than finite diffference methods. Central to this question of efficiency is the issue of the time differencing. A study by Fulton and Schubert (1987) based on the one-dimensional linear advection equation indicates that fourth-order time differencing is generally as efficient as second-order; when the time step is limited by accuracy rather than stability, fourth-order schemes can be at least an order of magnitude more efficient. The efficiency of the time discretization is not directly related to the use of Fourier-Chebyshev series expansions but rather to the exponential convergence of the spectral method. Similar conclusions can also be found in Appendix B, a study of the one-dimensional nonlinear advection equation. Because of the high accuracy required to simulate cloud top processes, fourth-order Runge-Kutta time discretization is used in the present model.

3.3 Condensation and evaporation

At each point in physical space on the transform grid, we must solve (3.5)–(3.8) iteratively. Beginning with the values of Θ and r predicted from (3.3) and (3.4), we first assume that $r \leq q^*$. If this assumption leads to a contradiction, we must conclude that $r > q^*$ and

$q = q^*$. Then, q can be eliminated between (3.5) and (3.6) to obtain

$$G(\theta) = \theta + \frac{L}{c_p}\bar{q}^* \exp\left\{\frac{L}{R_v\theta_0}\left(\frac{\theta-\theta_0}{\theta_0}\right)\right\} - \Theta = 0\,, \tag{3.22}$$

which must be solved iteratively for θ. If we are at iteration $\nu+1$, two approximations to $G(\theta) = 0$ are

$$G(\theta^{(\nu)}) + G'(\theta^{(\nu)})(\theta^{(\nu+1)} - \theta^{(\nu)}) = 0 \tag{3.23}$$

and

$$G(\theta^{(\nu)}) + G'(\theta^{(\nu)})(\theta^{(\nu+1)} - \theta^{(\nu)}) + \frac{1}{2}G''(\theta^{(\nu)})(\theta^{(\nu+1)} - \theta^{(\nu)})^2 = 0\,, \tag{3.24}$$

where $\theta^{(\nu)}$ is the value of potential temperature at iteration ν and the prime denotes differentiation with respect to θ. If we approximate the last term in (3.24) by the value of $\theta^{(\nu+1)} - \theta^{(\nu)}$ determined in (3.23) we obtain

$$\theta^{(\nu+1)} = \theta^{(\nu)} - \frac{G(\theta^{(\nu)})}{G'(\theta^{(\nu)})}\left\{1 + \frac{1}{2}\frac{G''(\theta^{(\nu)})G(\theta^{(\nu)})}{[G'(\theta^{(\nu)})]^2}\right\}\,, \tag{3.25}$$

which is a refined Newton scheme. The refined Newton scheme finds frequent application in numerical analysis, e.g. in the calculation of Gaussian quadrature points (Davis and Rabinowitz, 1984, page 114). It reduces to the ordinary Newton scheme if the second derivative term in the braces is neglected. According to Langlois (1973), the estimation of θ by (3.25) is accurate enough that iteration is not necessary. Our experience is almost this good; we have found that (3.25) produces a machine accurate solution to (3.22) in only three iterations even when the initial guess of θ is off by 10 K. Fig. 3.2 illustrates the absolute errors in θ and l as a function of the number of iterations of equation (3.25) when the initial θ guess is either equal to Θ or 10° K away from the solution. In the model integrations discussed here we have applied (3.25) four times at each time step.

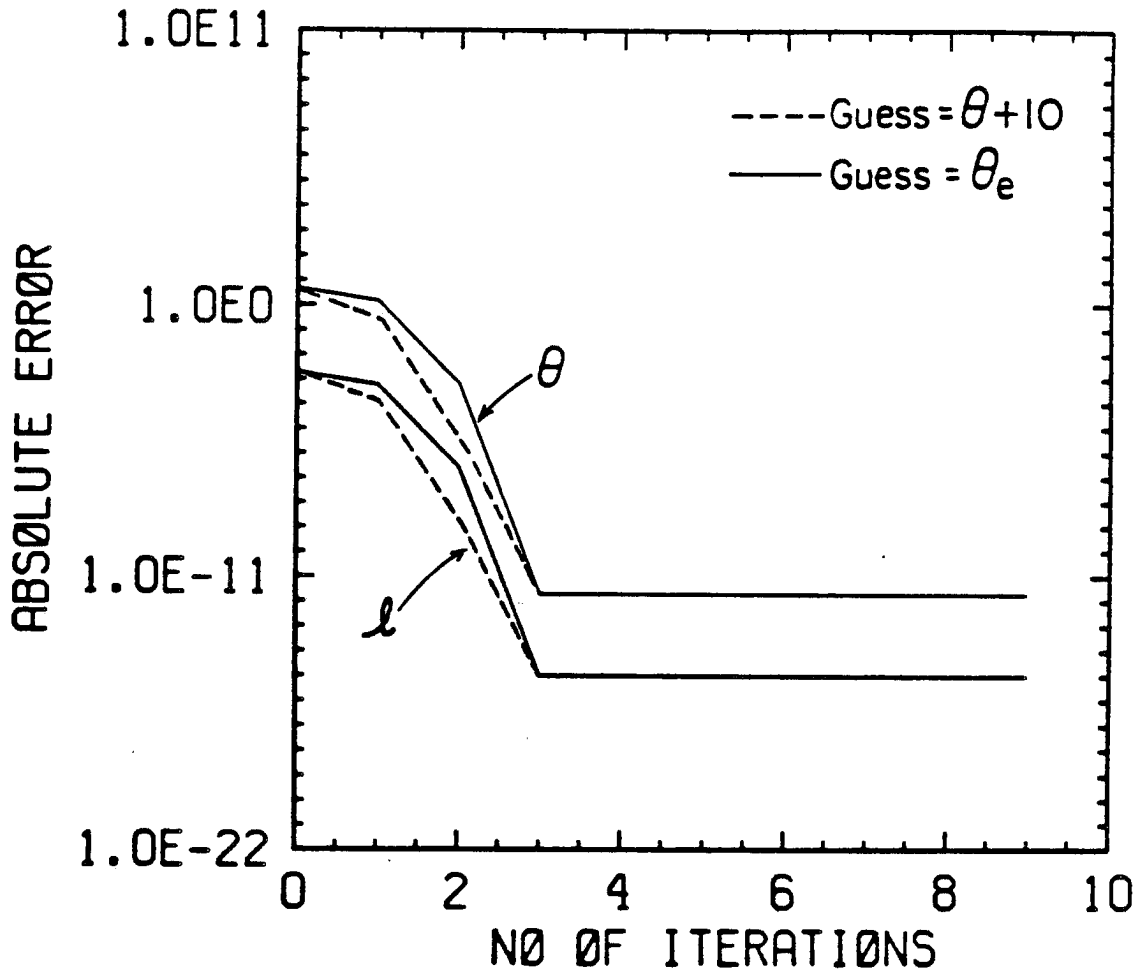

Figure 3.2. The absolute errors of the θ temperature and l cloud liquid water mixing ratio as a function of the number of iterations for the moisture physics iteration scheme (3.25) when the initial θ guess is equal to either the Θ temperature or 10° K away from the solution.

CHAPTER IV

MODEL PARAMETERS, SOUNDINGS AND DRY MODEL RUN

To simulate entrainment instability, both unforced and radiatively forced moist model experiments are performed. In each case the model domain is 2500 m in the (periodic) horizontal direction and 800 m in the vertical. The spectral discretization is Fourier-Galerkin in the horizontal and Chebyshev-tau in the vertical, with 64 modes in each direction ($N = M = 64$). The transform grid for the calculation of nonlinear and diabatic terms consists of 192 equally spaced points in the horizontal and 96 unequally spaced points in the vertical, giving an approximate resolution of nearly 10 m in each direction. A four second time step is used in the fourth-order Runge-Kutta time integration. This four second time step retains the full accuracy of the spatial discretization. The coefficient of eddy diffusivity k_z is 1.8 m^2s^{-1} and k_z is 8 m^4s^{-1} in the present model. These coefficients have been chosen so that the enstrophy cascade in the initial bubble experiment will not lead to spectral blocking. In testing the model we found that the time and horizontally averaged fluxes from a radiatively forced model change little when k_z and k_z are changed by a factor of two. For the forced moist model, a large scale subsidence is specified according to a climatic divergence value of 5×10^{-6} s^{-1}. Additional upper incoming boundary conditions for Θ and r are also specified. The ocean is assumed to have a surface potential temperature θ_{sfc} of 286.2 K. This sea surface temperature corresponds to a saturation mixing ratio q^*_{sfc} of 9.4 g kg^{-1} and a Θ_{sfc} of 309.3 K. The oceanic surface fluxes are computed by the bulk formulas, i.e.

$$\overline{w'\Theta'}_{sfc} = C_T V(\Theta_{sfc} - \Theta_{ref}) ,$$

$$\overline{w'r'}_{sfc} = C_T V(q^*_{sfc} - r_{ref}) ,$$

where Θ_{ref} and r_{ref} are the equivalent potential temperature and total water at a reference level(i.e. at the top of the surface layer, 25 m) and C_T is the bulk transfer coefficient, which

has the constant value of 0.0015. The surface wind speed V is taken to be 7 m/s in the present study. The Θ and r fluxes in the surface layer have a specified height dependence which decreases to nearly zero at the top of the surface layer. The magnitude of the surface flux is computed from the bulk aerodynamic formula. The convergences of the Θ and r fluxes in the surface layer (surface to 25 m altitude) are computed every time step in physical space ($\mathcal{R}$ and surface forcing part of $\mathcal{Q}$) and then transformed into spectral space to generate the model tendencies in the forced situation. The infrared forcing part of $\mathcal{Q}$ will be discussed in Chapter 5.

The initial conditions considered here consist of a well mixed but motionless boundary layer with a depth of about 450 m. The equivalent potential temperature in this mixed layer is 305.0 K and total water mixing ratio is 7.9 g kg^{-1}. The sub-cloud potential temperature is very near the sea surface temperature. The inversion depth is 100m. The cloud layer in this boundary layer extends from 200 m to 450 m with the liquid water content increasing nearly linearly with height at the adiabatic rate. The peak liquid water content in the cloud is 0.32 g kg^{-1}. Four types of air are considered above this boundary layer. The first type is relatively dry with a total water content of 2 g kg^{-1} and an equivalent potential temperature of 302.0 K at the top of the inversion (hereafter referred to as the U1 sounding). The second type of overlying air has a total water content of 3.5 g kg^{-1} and a Θ of 308 K at the top of the inversion (hereafter referred to as the S sounding). The third type of air considered above the same boundary layer is a very dry one with a total water content of 0.5 g kg^{-1} (hereafter referred to as the U2 sounding). The last type of air has a total water content of 2 g kg^{-1} and a Θ of 311 K (hereafter referred to as the S1 sounding). In all cases, Θ gradually increases at a rate of 0.01 K m^{-1} from the inversion top to the model top. The vertical profiles of equivalent potential temperature Θ, potential temperature θ, cloud liquid water l and water vapor q for the S1, S, U1 and U2 soundings are shown in Figs. 4.1 through 4.4.

Physically, both the U1 and U2 soundings are classical "unstable" cases in the sense that the Θ jump across the capping inversion is negative (-3 K for the U1 case and -7 K for the U2 case). The inversion strength in the U1 and U2 cases is about 10 K in θ. The U2 sounding will be used to test the idea of stratocumulus breakup by entrainment instability

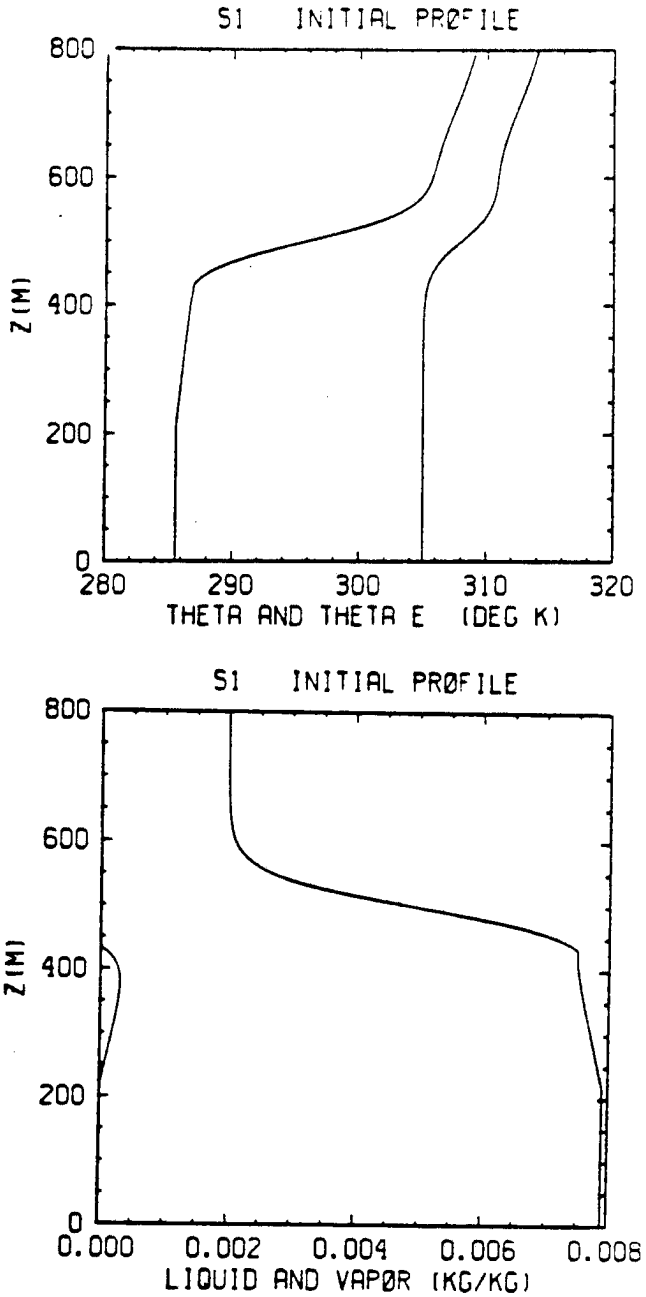

Figure 4.1. The S1 initial profiles of Θ the equivalent potential temperature, θ the potential temperature, q the mixing ratio of water vapor and l the mixing ratio of liquid water.

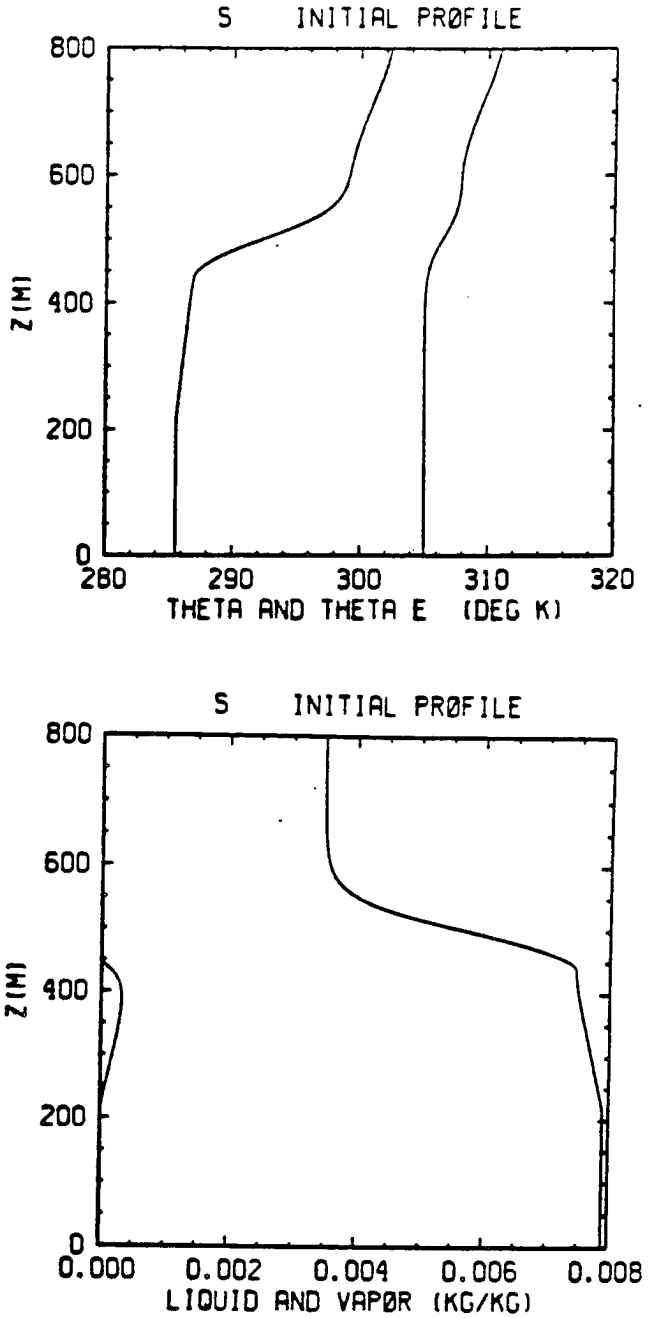

Figure 4.2. Same as figure 4.1 except for the S sounding.

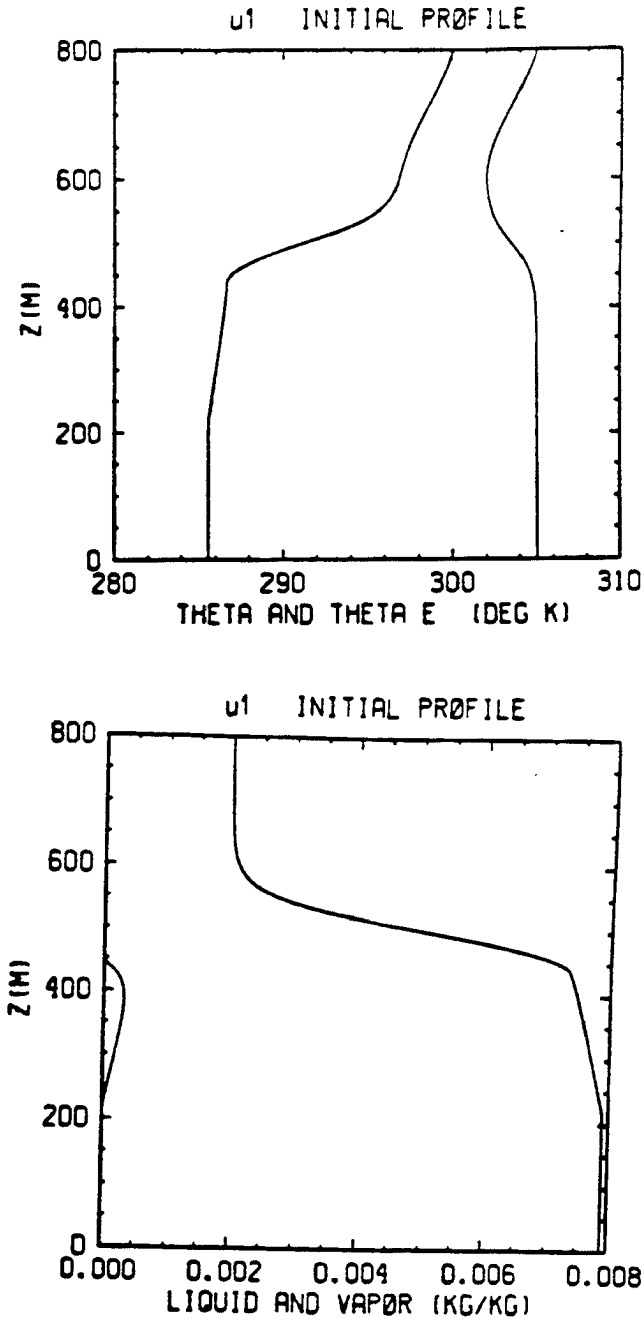

Figure 4.3. Same as figure 4.1 except for the U1 sounding.

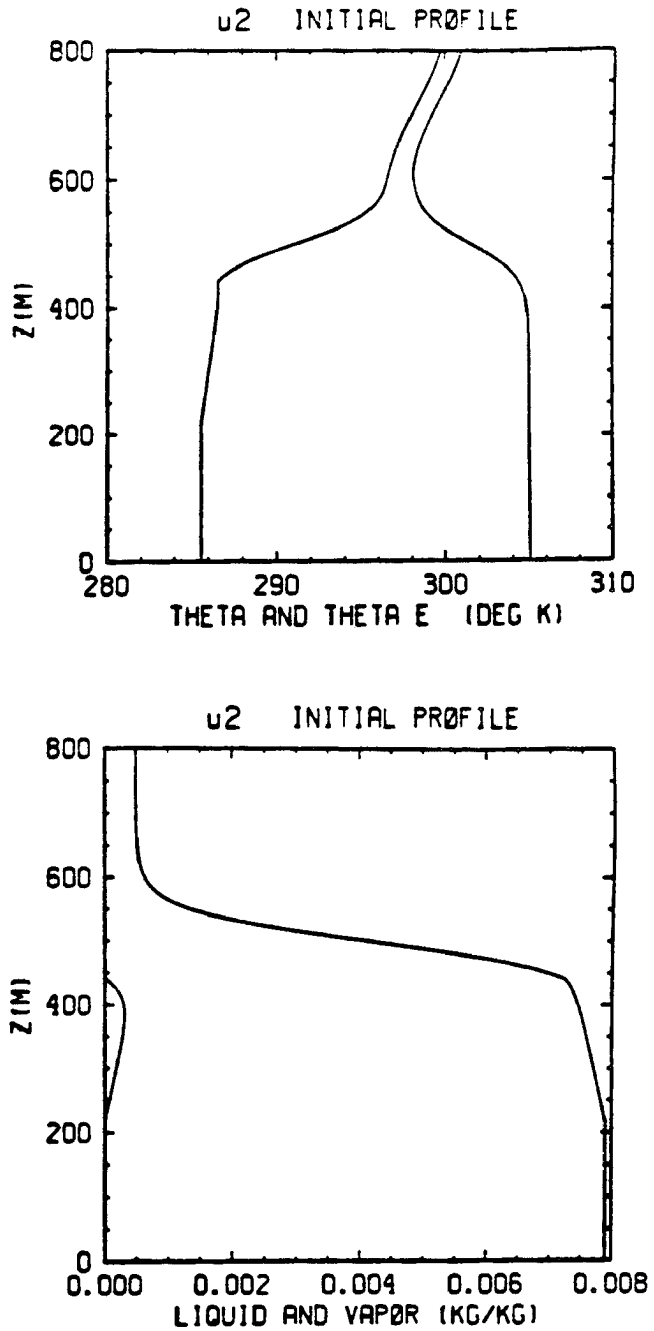

Figure 4.4. Same as figure 4.1 except for the U2 sounding.

when the upper air is extremely dry and the negative Θ jump is large. The S profile is constructed so that it has a 2 K stronger θ temperature inversion strength than the U1 and U2 soundings and with a higher total water content (3.5 g kg^{-1}) above the boundary layer. Due to more moisture aloft, the S case has a Θ jump of 3 K. The S case is stable because of the positive Θ jump across the cloud top. We will use these three soundings (the U1, U2 and S soundings) to study the problem of entrainment instability in the unforced (initial value problem) and radiatively forced moist models. The S1 sounding will be used to study the interaction of the infrared radiative loss and the boundary layer dynamics.

We are interested in the relationship between the local structure of the cloud topped boundary layer and the different local mean conditions (e.g. sea surface temperature, subsidence, radiative cooling) rather than investigating the evolution of the cloud boundary layer with time. Therefore, all the fluxes in the radiatively forced experiments are computed for a one hour period after an hour or two of model integration, thus increasing the probability that the boundary layer is in equilibrium with fixed mean conditions. As we shall discuss later, the steady state dynamics of the boundary layer does not depend on the horizontal and vertical distributions of the radiative cooling so long as the cooling is in the turbulent region. In addition, the classical unstable cases U1 and U2 do not differ much from the stable case S. We do not see signs of the cloud breakup in any of the cases. The concept of "stratocumulus breakup by entrainment instability"may be a misleading one.

Two "dry" model runs will be performed before the radiatively forced moist experiments. In these two dry experiments, the effect of latent heat is completely ignored. A rising warm anomaly of 1 K in the 'dry' well mixed boundary layer is the first experiment. The θ fields with a contour interval of 0.25 K superimposed on the velocity fields (in arrows) are illustrated in Figs. 4.5 through 4.9. These figures are in a 5 minute model time sequence. Fig. 4.5 illustrates the initial condition of a 4 K inversion located at 500 m and a warm anomaly of 1 K assumed near the surface. A mushroom shaped rising bubble with a sharp temperature gradient can be clearly seen after 5 minutes (Fig. 4.6). In Fig. 4.7 and Fig. 4.8 we observe that the warm bubble rises to the top of the boundary layer and excites gravity wave oscillations in the capping inversion. Finally, the propagation of the secondary circulations toward the boundary is shown in Fig. 4.9. These secondary circulations seem

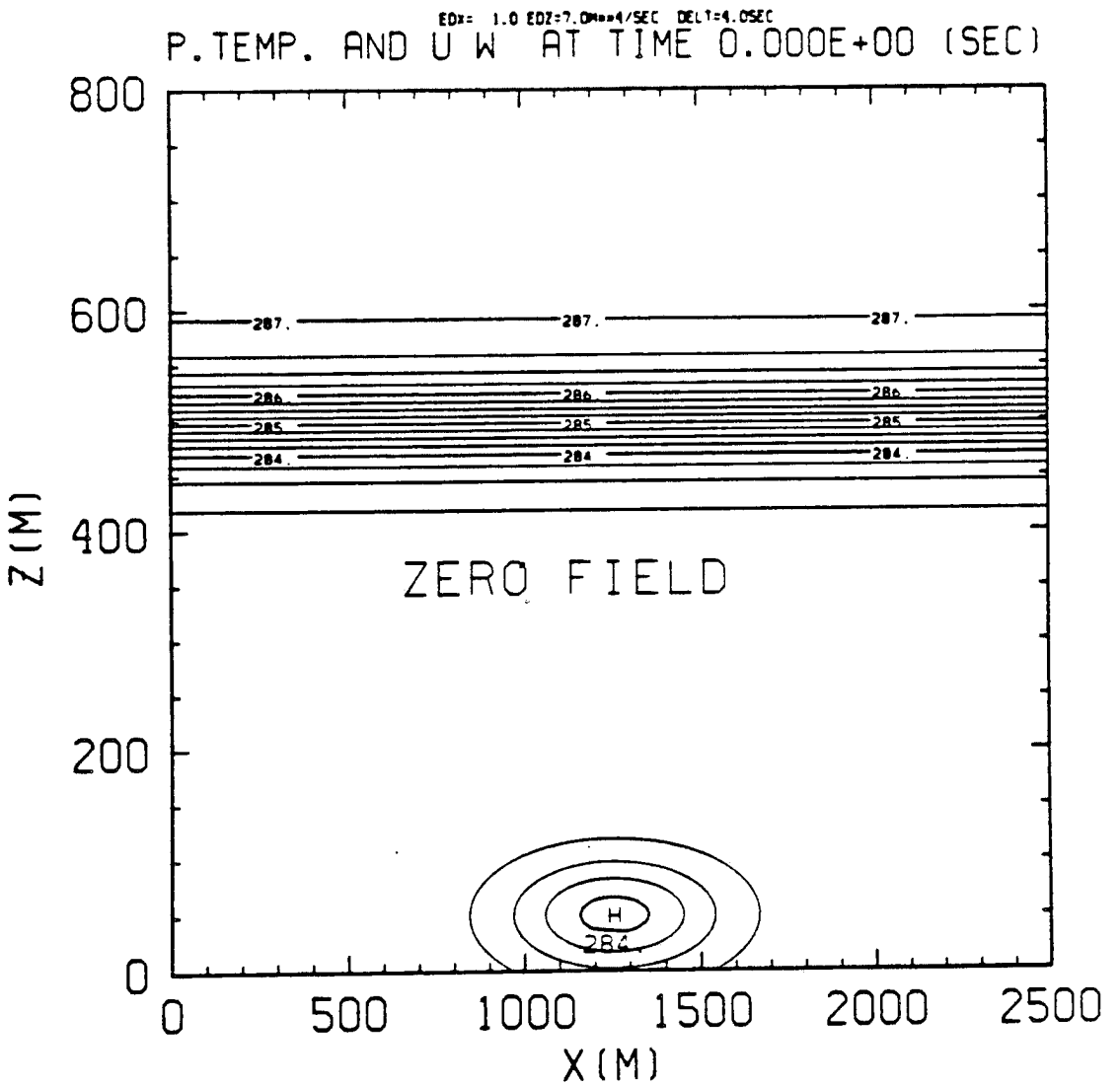

Figure 4.5. The initial θ temperature and velocity in the physical domain for the dry initial value problem.

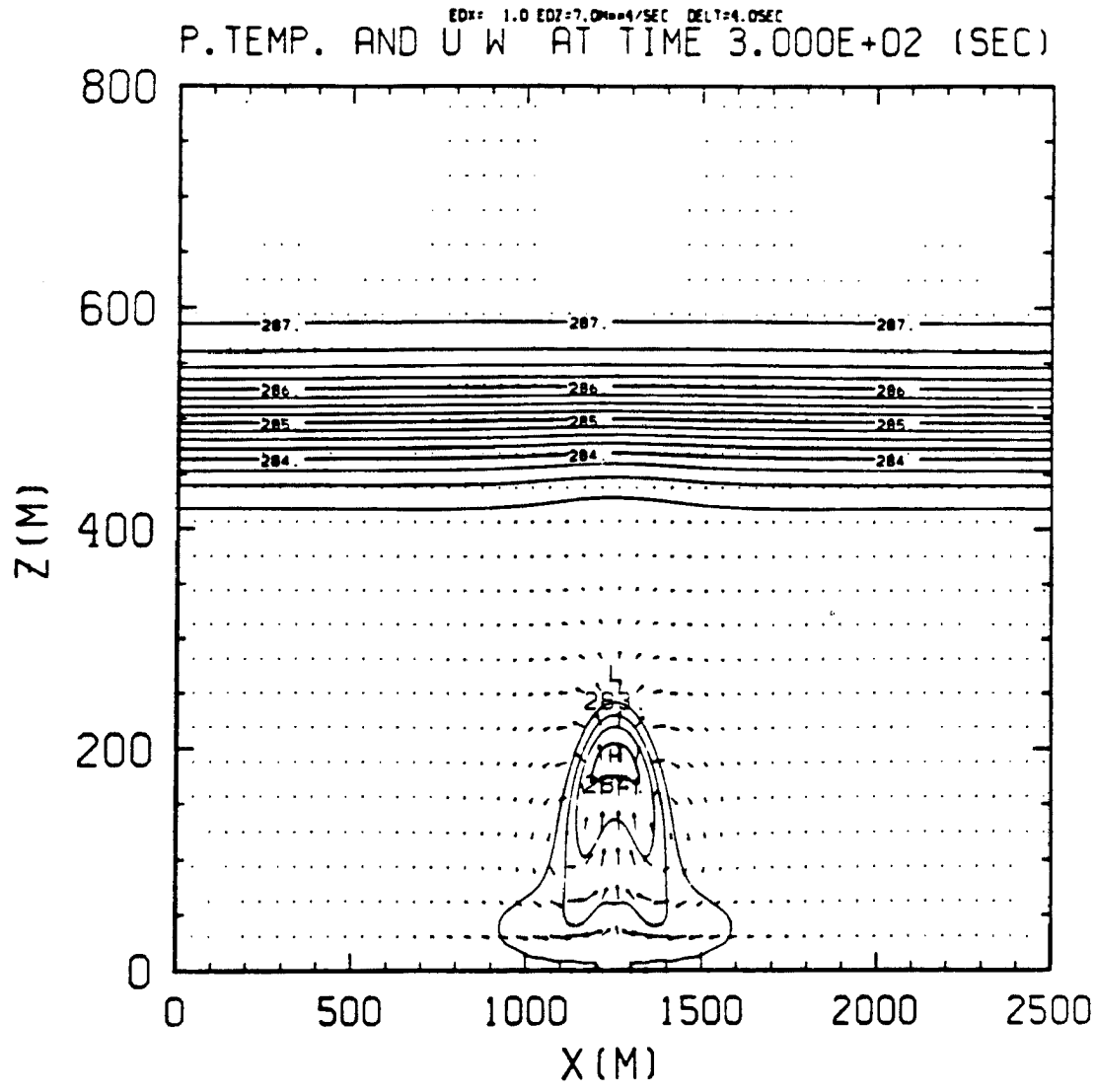

Figure 4.6. The θ temperature and velocity in the physical domain at 5 minutes for the dry initial value problem. Arrows represent wind velocity scaled by maximum velocity. The maximum velocity is 1.93 m s^{-1}.

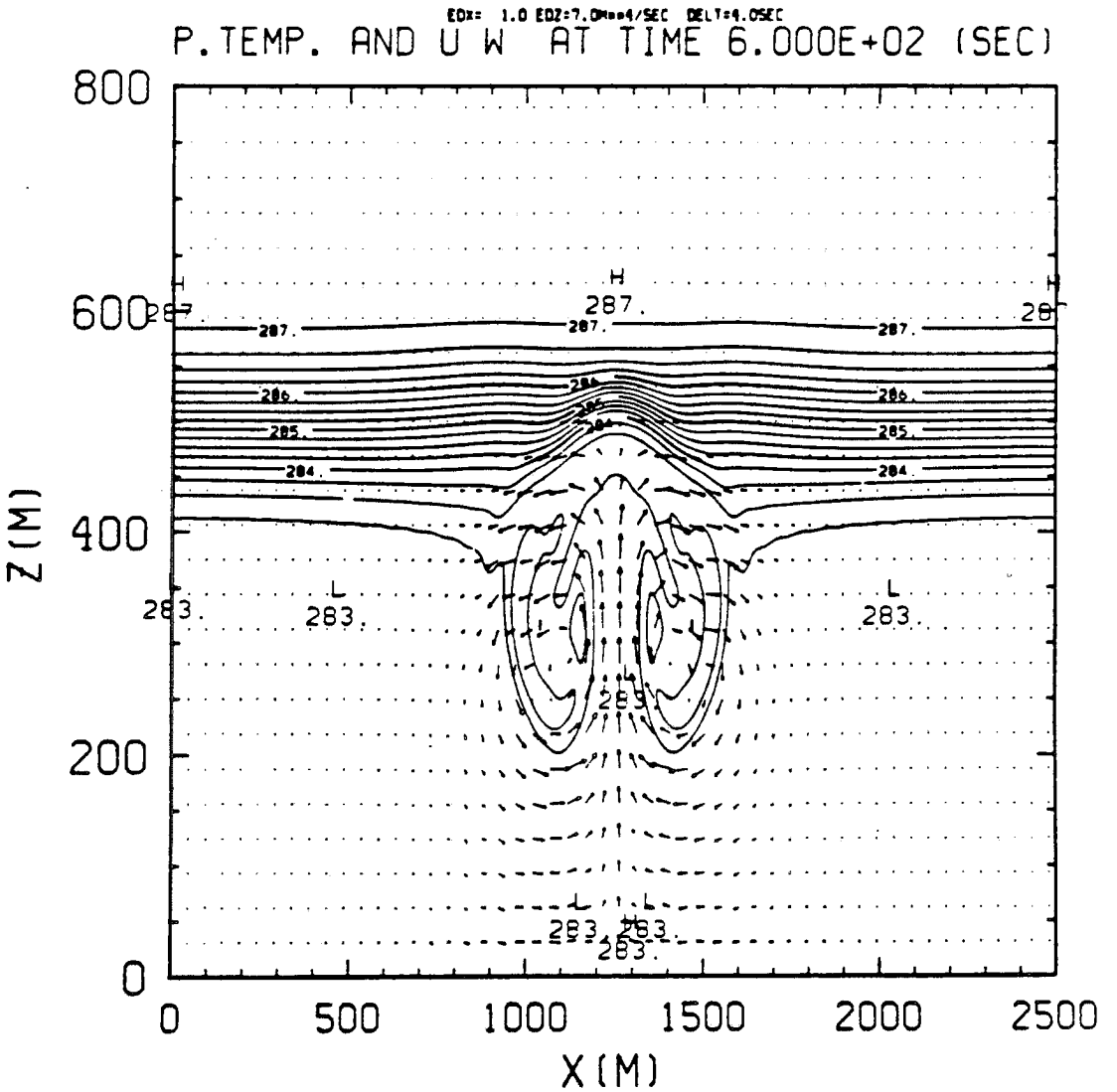

Figure 4.7. Same as figure 4.6 except at 10 minutes and the maximum velocity is 2.47 m s^{-1}.

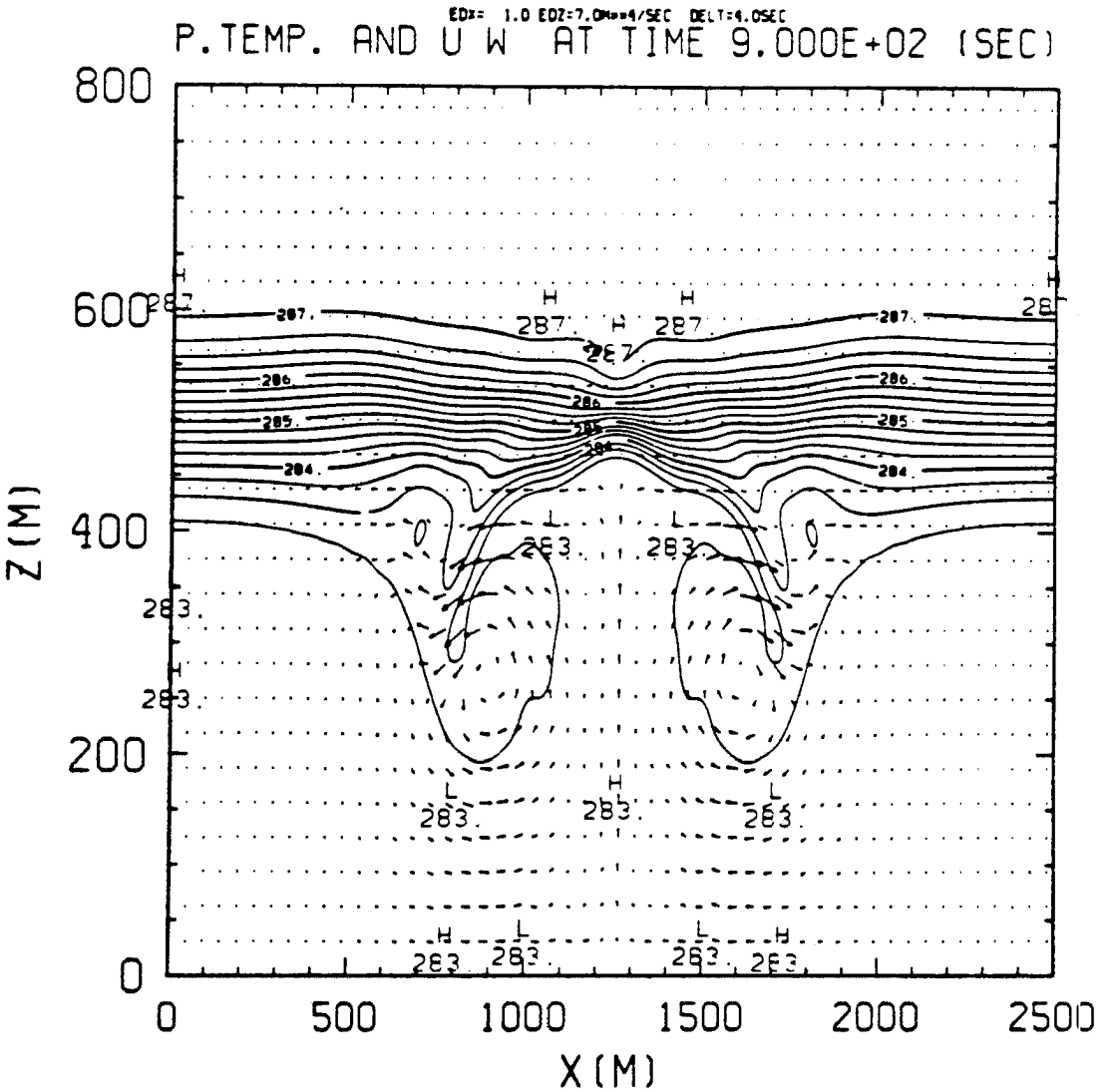

Figure 4.8. Same as figure 4.6 except at 15 minutes and the maximum velocity is 2.66 m s^{-1}.

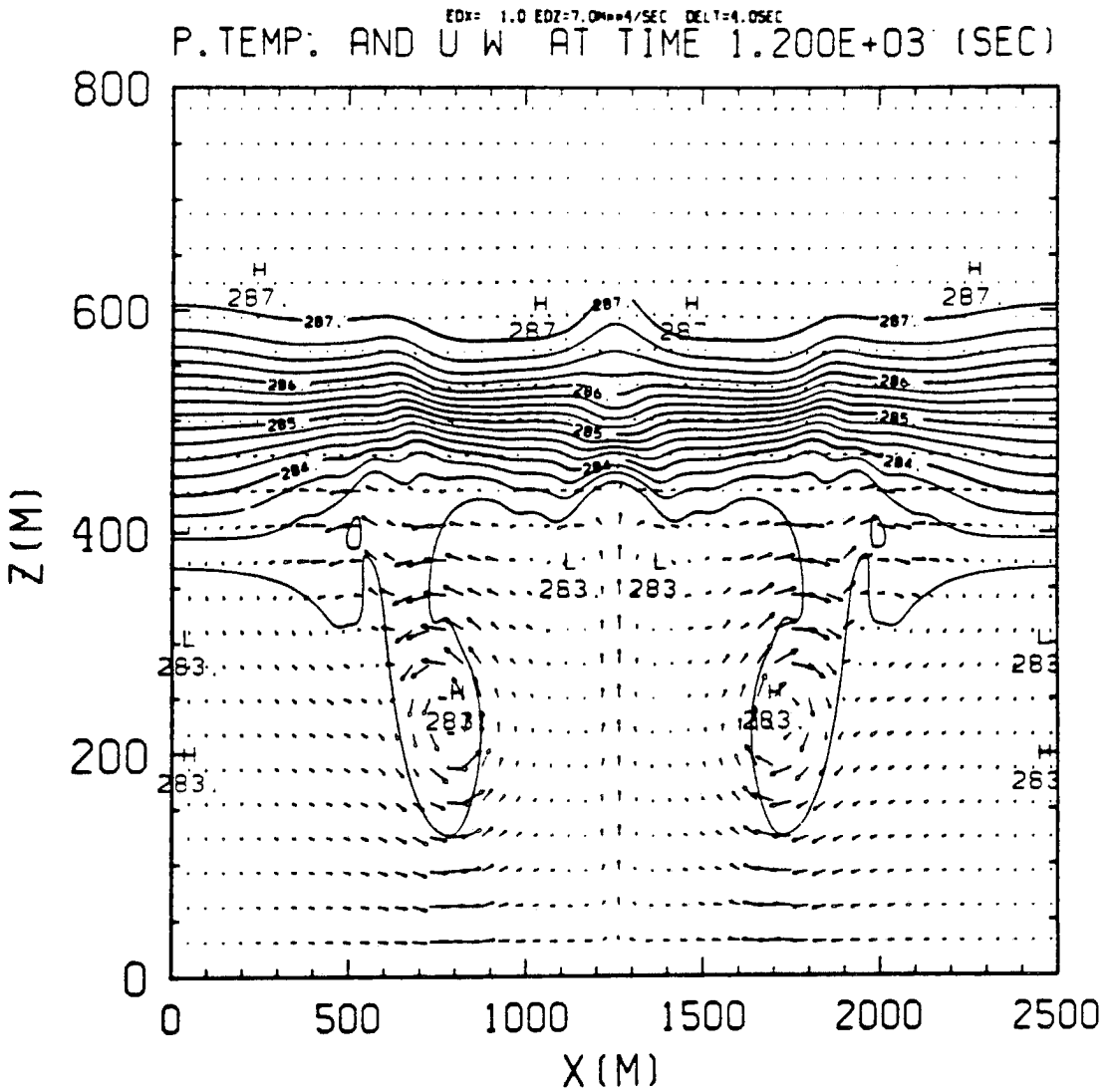

Figure 4.9. Same as figure 4.6 except at 20 minutes and the maximum velocity is 1.49 m s^{-1}.

to travel with the speed of gravity waves in the inversion. Another interesting feature is the entrainment of warmer inversion air into the boundary layer associated with the secondary circulations and the trapped gravity waves in the inversion. The Fourier-Chebyshev discretization and the spectral subgrid diffusion in this experiment are capable of producing the physically realistic, steep temperature gradients. We have also run this experiment with a less scale-selective subgrid diffusion in physical space and with the Crank-Nicholson scheme (not shown here); similar results were obtained except that the inversion depth spread 50 m in 20 minutes. Therefore, the subgrid diffusion in spectral space as discussed before will be used throughout the rest of this study.

The second 'dry' experiment is a radiatively forced one. A 450 m deep boundary layer of 305 K under a 6 K capping inversion is used as the initial condition. This initial condition is time integrated with a fixed radiative cooling of 10 K hr^{-1}, localized at the top of the boundary layer. Note that there is no background turbulence initially and the surface heat flux is very weak throughout the whole period of integration (90 minutes). Fig. 4.10 shows the vertical profiles of the horizontally averaged θ field at the initial time, 20 minutes and 90 minutes. The minimum θ appears near 400 m at 20 minutes because of the radiative cooling and the lack of enough turbulence at this time to smooth it. This θ minimum disappears and the turbulent boundary layer is well mixed at the end of the model integration time. The θ fields and velocity fields at 80 and 90 minutes are presented in Figs. 4.11 and 4.12. These figures indicate a boundary layer with one cell of circulation in the vertical and with gravity waves mostly trapped in the inversion. Because the surface flux is very small, these circulations are driven radiatively from the boundary layer top. The dome-shaped inversion base, the well mixed boundary layer as well as the strong entrainment of warmer air from the inversion (e.g. at $x \simeq 200$ m in Fig. 4.11) are all attributed to the presence of these convective circulations. The heat flux profile computed during last 30 minutes is shown in Fig. 4.13. The flux inside the boundary layer is linear, as we would expect from a well mixed boundary layer. The large negative flux at the top of the boundary layer is consistent with the strong entrainment observed in Figs. 4.11 and 4.12.

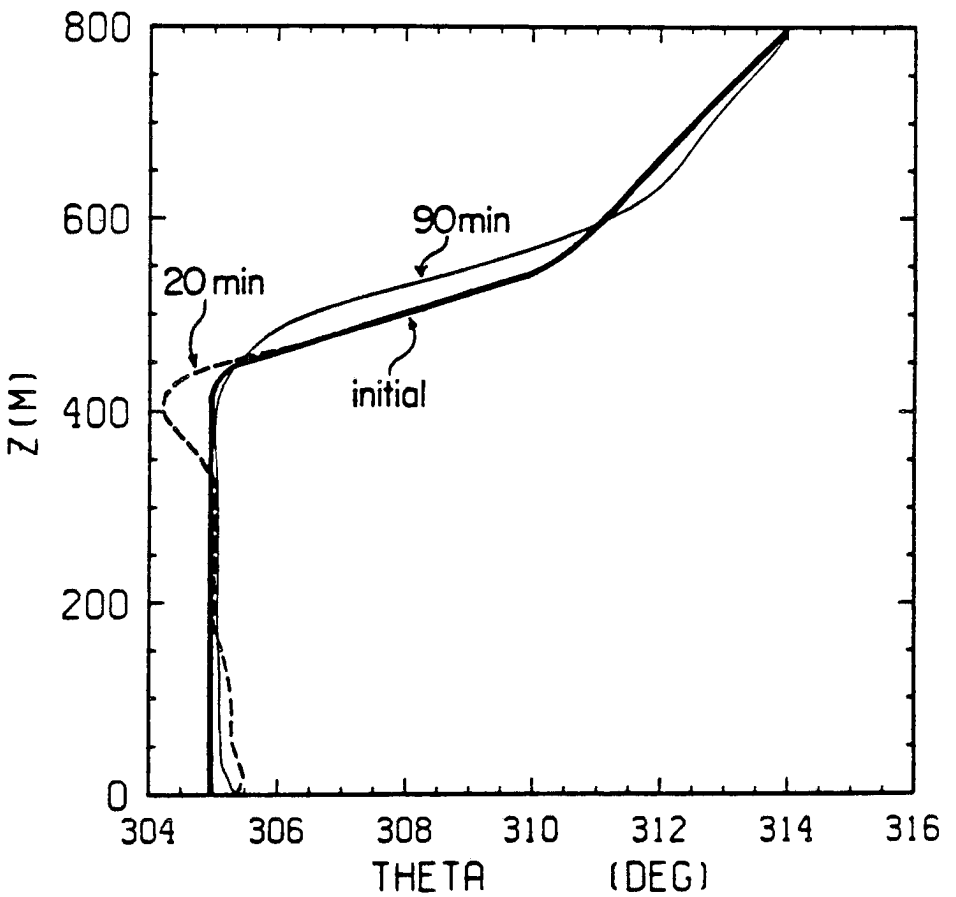

Figure 4.10. The vertical profiles of the horizontally averaged θ temperature at initial time, 20 minutes and 90 minutes in the radiatively forced dry experiment.

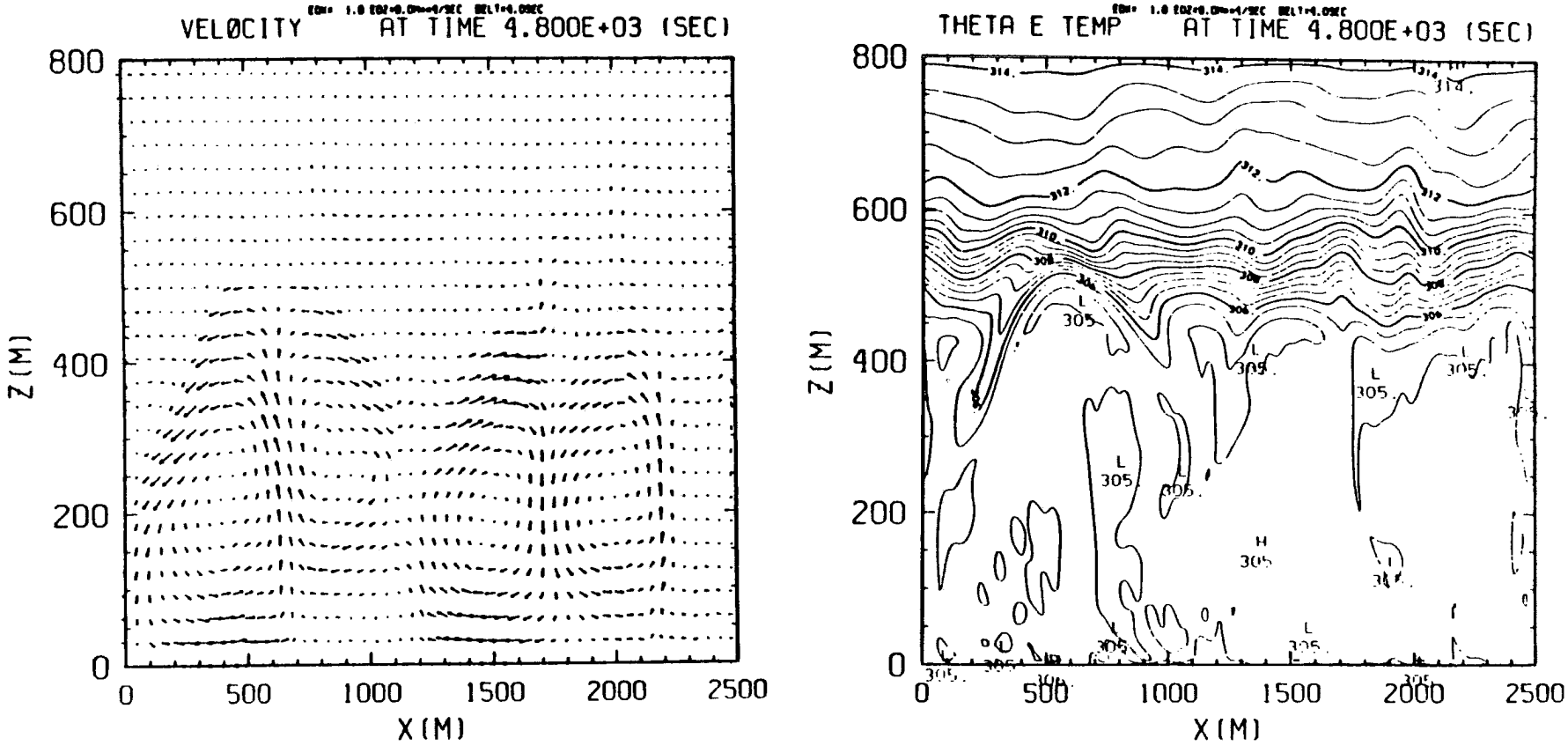

Figure 4.11. The velocity and the θ fields in the physical domain at 80 minutes in the radiatively forced dry experiment. The velocity picture is presented in the left adjacent to the θ picture. The maximum velocity is 4.25 m s^{-1}.

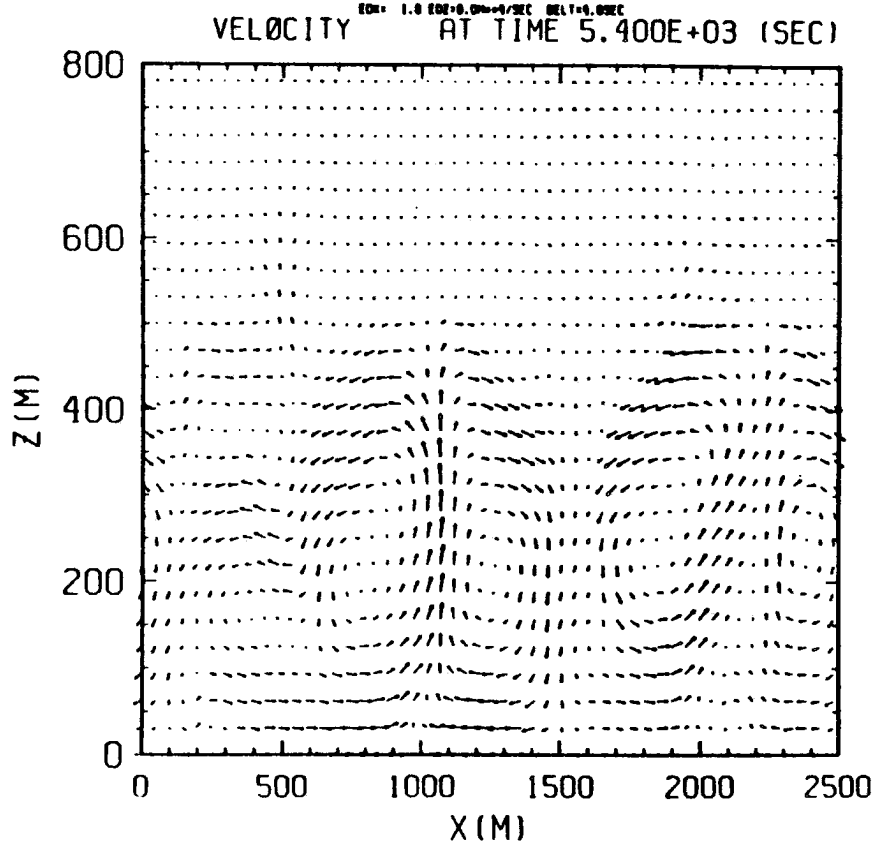

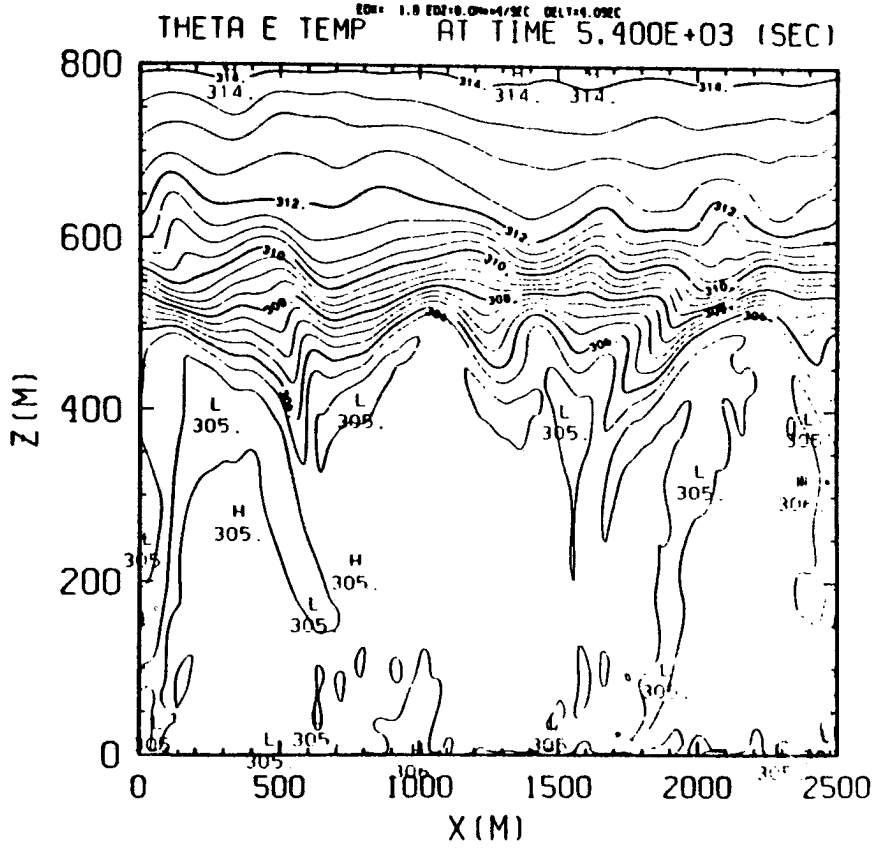

Figure 4.12. **Same as figure 4.11 except at 90 minutes and the maximum velocity is 4.02 m s^{-1}.**

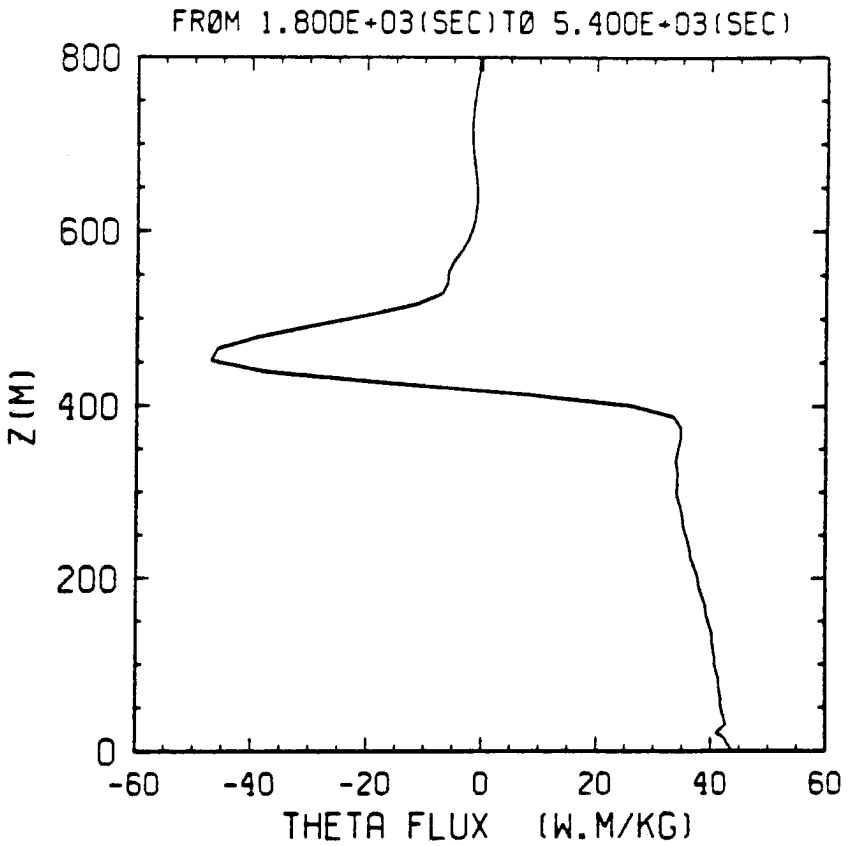

Figure 4.13. **The heat flux profile computed in the period of 30 minutes from the radiatively forced dry experiment.**

CHAPTER V

CLOUD TOP INFRARED RADIATIVE COOLING

The long wave infrared cooling at the cloud top plays an important role in the maintenance of the cloud top inversion and the convective circulations in the cloud-topped mixed layer. Tethered balloon measurements showed that as clouds become thicker, the infrared cooling becomes more confined to the cloud top. Stephens and Platt (1987) emphasized the potential importance of the horizontal variation in infrared radiative cooling. In this chapter, we will study how the dynamics in the marine boundary layer are affected by vertical and horizontal variations of infrared radiative cooling. Section 5.1 describes the inclusion of cloud-topped infrared radiative cooling in the model. Sensitivity tests are performed to determine the importance of the various infrared radiative forcings in section 5.2.

5.1 Radiative forcings

Instead of using the classical one-dimensional radiative transfer calculation fully interactively in the model, some simple cloud-top radiative forcings will be implemented. To understand the impact of the various infrared cooling rates on the boundary dynamics, the S1 sounding illustrated in chapter 4 will be integrated under several different radiative forcings. Because of the low cloud base and cold ocean surface temperature (about the same as the surface air temperature), cloud base warming by infrared radiation is neglected. There are two reasons for not using detailed fully interactive radiative transfer calculations in the present stage of this work. First, it is not clear that the classical plane parallel assumption is valid in a fine resolution model like ours. Also, we want to use the majority of computer resources on the resolution necessary for simulation of non-radiative cloud-top processes. Secondly, as we will discuss in the next section, the average vertical heat and water flux profiles are insensitive to the different types of radiative cooling so long as the cooling is inside the turbulent cloudy region. Thus the use of a simple radiative forcing seems to be

justified. A more detailed infrared radiative transfer calculation may not be necessary if we are only after a steady state solution.

The cloud top infrared radiative cooling will be handled either non-interactively or interactively. Five profiles of infrared radiative forcing are presented in Fig. 5.1. The cooling profiles C, D and E are for the non-interactive radiative forcings while profiles A and B are for the interactive forcings. The vertical bar in Fig. 5.1 indicates the vertical extent of the cloud initially. The non-interactive radiative forcings are fixed; they are homogeneous in the horizontal and in time. The cooling in profiles D and E is 50m deep and has a peak of about -11 K hr^{-1}. The cooling profile C covers a depth of 120m and peaks at 350m with a magnitude of about 3.5 K hr^{-1}. The cooling region in profile E is well into the capping inversion while that in profile C is deep inside the cloud. Throughout most of the model integration, forcing C is in the one hundred percent cloud fraction region while forcing E is in the region of zero cloud fraction. The cloud fraction in the region where the cooling D is placed may become less than one hundred percent during the integration due to the formation of small gaps between cloud cells. Parts of the cooling will unavoidably be applied to clear regions between cloud cells. We will use these non-interactive forcings to study the importance of different vertical distributions of radiative cooling.

The interactive infrared radiative forcings (forcings A and B) are designed to follow variations in cloud liquid water content and are confined to the top 75m of the cloud. The height of the maximum cooling in the interactive forcings varies to follow the cloud top topography. The radiative forcing A occurs in a 75m deep layer with the peak cooling in the center of the layer. The maximum cooling rate in forcing A is about 3.5 K hr^{-1} which is very close to the peak value in forcing C. The profile B is similar to profile A except the maximum cooling is at the very top of the layer where cooling is applied. From cooling profile A or B as well as the initial cloud liquid water content profile in the top 75m of the cloud, we can find a height dependent ratio of infrared radiative cooling rate divided by liquid water content. To find the magnitude of the cooling at one vertical column during the time integration, the local cloud top height has to be found first. The cooling rate is then determined by multiplying the cloud liquid water content by the corresponding ratio counting from the cloud top down. Thus the cooling will always cover about the top 75m

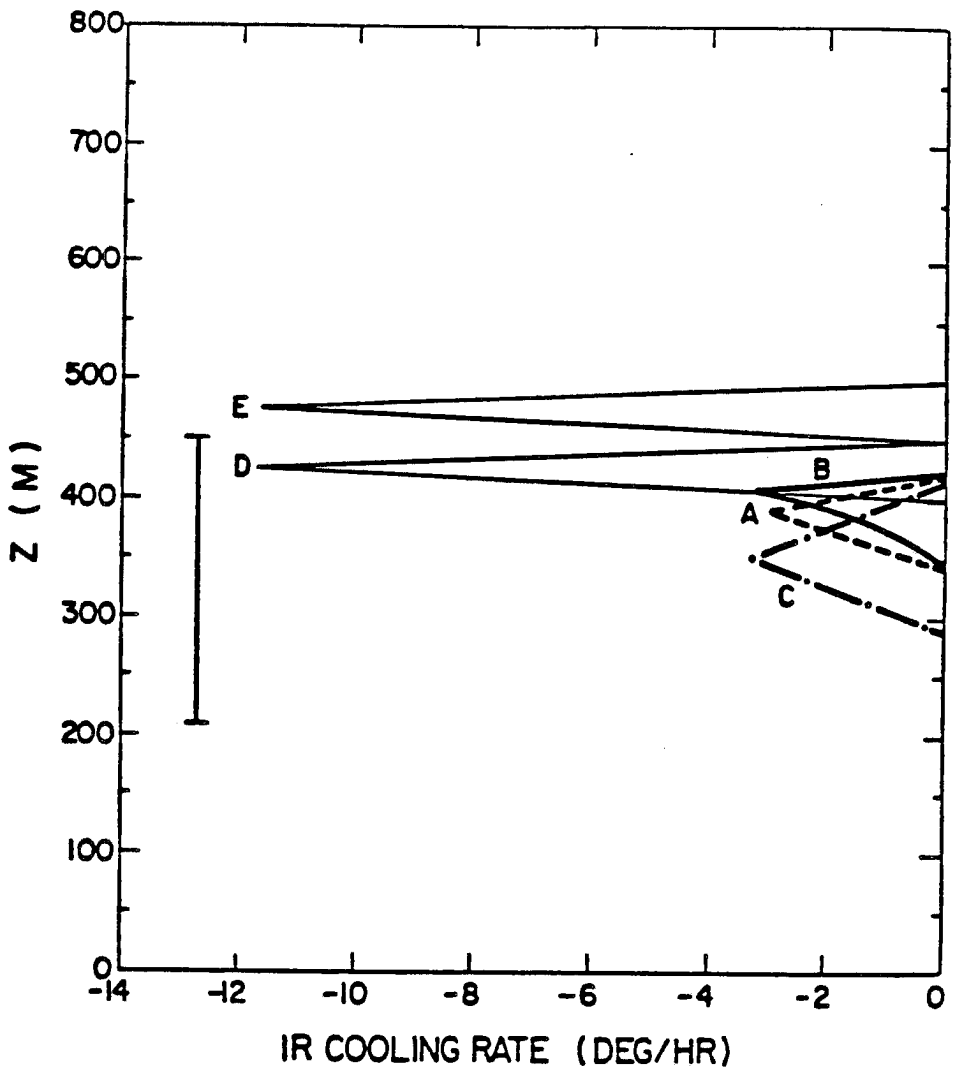

Figure 5.1. Five different profiles of infrared radiation cooling forcings used in the moist experiments. The vertical bar indicates the vertical extent of cloud at the initial time.

of the cloud in one vertical column with its magnitude depending on the amount of the liquid water content locally. The vertical distribution of the cooling depends on whether profile A or B is used in computing the height dependent ratio. This radiative forcing is interactive in the sense that the amount of cooling occurring locally is linearly proportional to the amount of liquid water diagnosed from the model. There will be no radiative cooling locally if cloud holes are formed; all the cooling is confined in the cloudy air. The interactive radiation is inhomogeneous in both space and time. The model sensitivity test based on forcings A, B and C will reveal the importance of spatial variability in cloud top cooling.

5.2 Infrared cooling sensitivity test

Satellite pictures reveal that stratocumulus over the cold ocean can exist for several days with little change in appearance. This implies that the boundary layer is often in a steady state. The equilibrium state of the marine boundary layer will be investigated by time and horizontally averaged flux profiles. The fluxes in all the experiments are computed in a one hour period after 60 minutes or 100 minutes of model integration from the S1 initial condition. The one hour or one hour 40 minutes model adjustment time before computation of the flux allows the boundary layer to reach an equilibrium state with fixed external conditions (e.g. the sea surface temperature, subsidence and radiative cooling).

To illustrate the importance of infrared cooling, experiments with the S1 sounding as initial condition under the five different radiative forcings are performed (hereafter referred to as experiments A, B, C, D and E). The horizontally averaged Θ, θ, q, and l profiles at the end of the model integration time are very similar to their initial values (in equilibrium with the mean conditions); therefore only the horizontally averaged Θ fields from experiments D and E at the end of model integration are shown in Fig. 5.2 (dash and dash dotted). Also plotted in Fig. 5.2 is the initial Θ profile (solid line). Fig. 5.2 indicates a well mixed layer at the end of the model integration. The minimum Θ in the capping inversion from experiment E is due to the radiative cooling and the lack of turbulence to smooth it. The slight warming above 600m in both experiments is due to the effect of subsidence. Fig. 5.3 presents the fluxes of Θ,θ,ϑ,r,q and l for all the experiments. These flux profiles are in the energy unit Wm kg^{-1} which is the same as the W m^{-2} if the air density is taken to be 1 kg

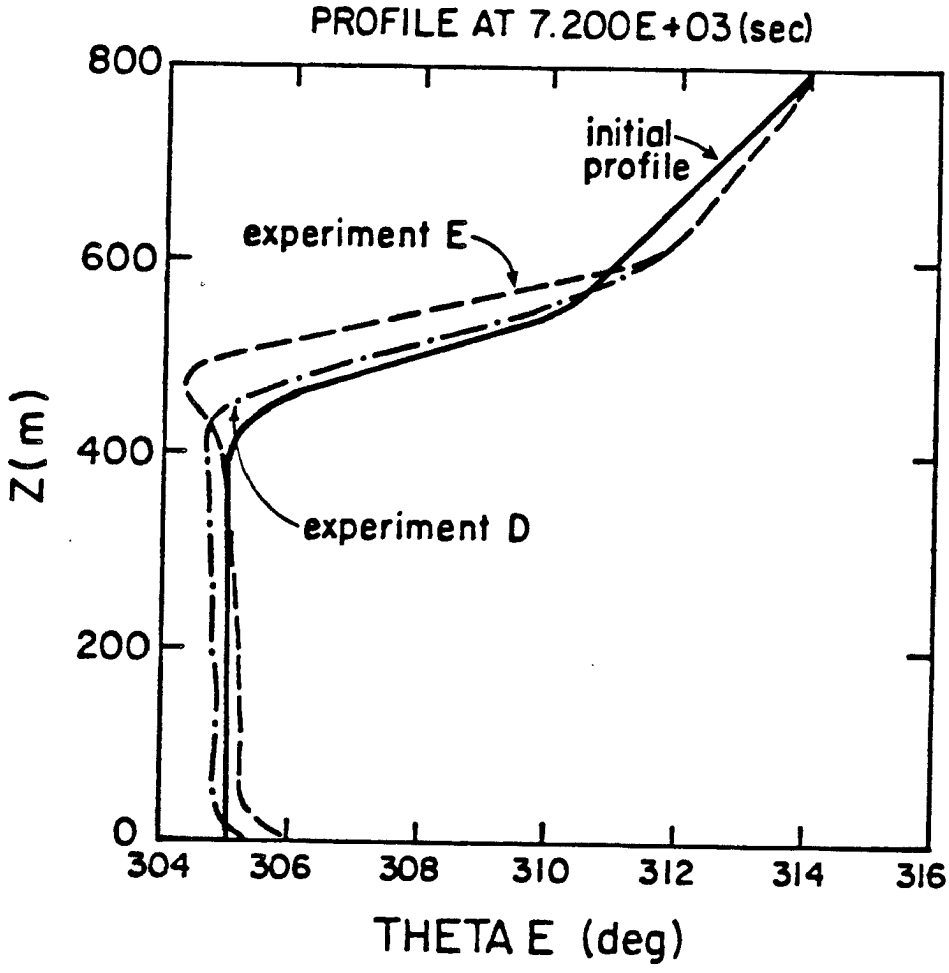

Figure 5.2. The vertical profiles of the horizontally averaged Θ temperature for experiments D and E at the end of the model integration time. Also plotted is the initial Θ profile (dashed line) of these two experiments.

m^{-3}. There are negative values in the cloud top regions for the buoyancy flux (ϑ flux), the heat flux (θ flux) and the Θ flux. These negative regions reflect the phenomena of convective overshooting. The Θ flux profiles from all five experiments are similar and comparable to the mixed layer model results of Schubert (1976, 1979a) except for the convective overshooting regions. The latent heat release inside the cloud contributes to larger θ and ϑ flux values in the cloud region. The sub-cloud buoyancy and heat fluxes are positive in experiments A, B, C and D as opposed to the negative values obtained in the classical mixed layer model. The total water and liquid water flux profiles are also comparable to the mixed layer results except for the increase of the flux near cloud top. One point to make here about Fig. 5.3 is that the individual flux profiles are almost identical for experiments A, B and C. The radiative forcings in experiments A and B are interactive and horizontally inhomogeneous, and the vertical distribution of cooling involved in experiments A and B are different. Experiment C has a homogeneous cooling deep inside the cloud. These three simple and independent types of cooling produce nearly the same convective flux profiles, indicating that the steady state of the model is insensitive to the vertical as well as the horizontal distribution of the radiative cooling so long as the cooling is inside the cloud. Experiment D has similar flux profiles compared to experiments A, B and C. However, the heat and buoyancy flux profiles in experiment E are quite different from the rest of the experiments. There are small negative heat and buoyancy fluxes near the cloud base region in experiment E. The sub-cloud heat and buoyancy fluxes in experiment E are smaller than in experiment D even though they both have the same amount of radiative cooling. The flux profiles from Fig. 5.3 indicate two types of equilibrium state, with experiment E differing from experiments A, B, C and D.

The velocity field (in arrows) and the cloud liquid water content at the end of the model integration for experiments A, B, C, D and E are shown in Figs. 5.4. through 5.8. The motion field and liquid water content pictures are shown adjacent to each other. From these liquid water pictures, we see that the stratocumulus cloud cell resembles a dome with sharp liquid water gradients on the sides. This sharp liquid water gradient has a length scale of approximately 40m and can extend down to the cloud base. The regions of the peak liquid water content (e.g. greater than 0.4g kg^{-1}) appear to be dome shaped and

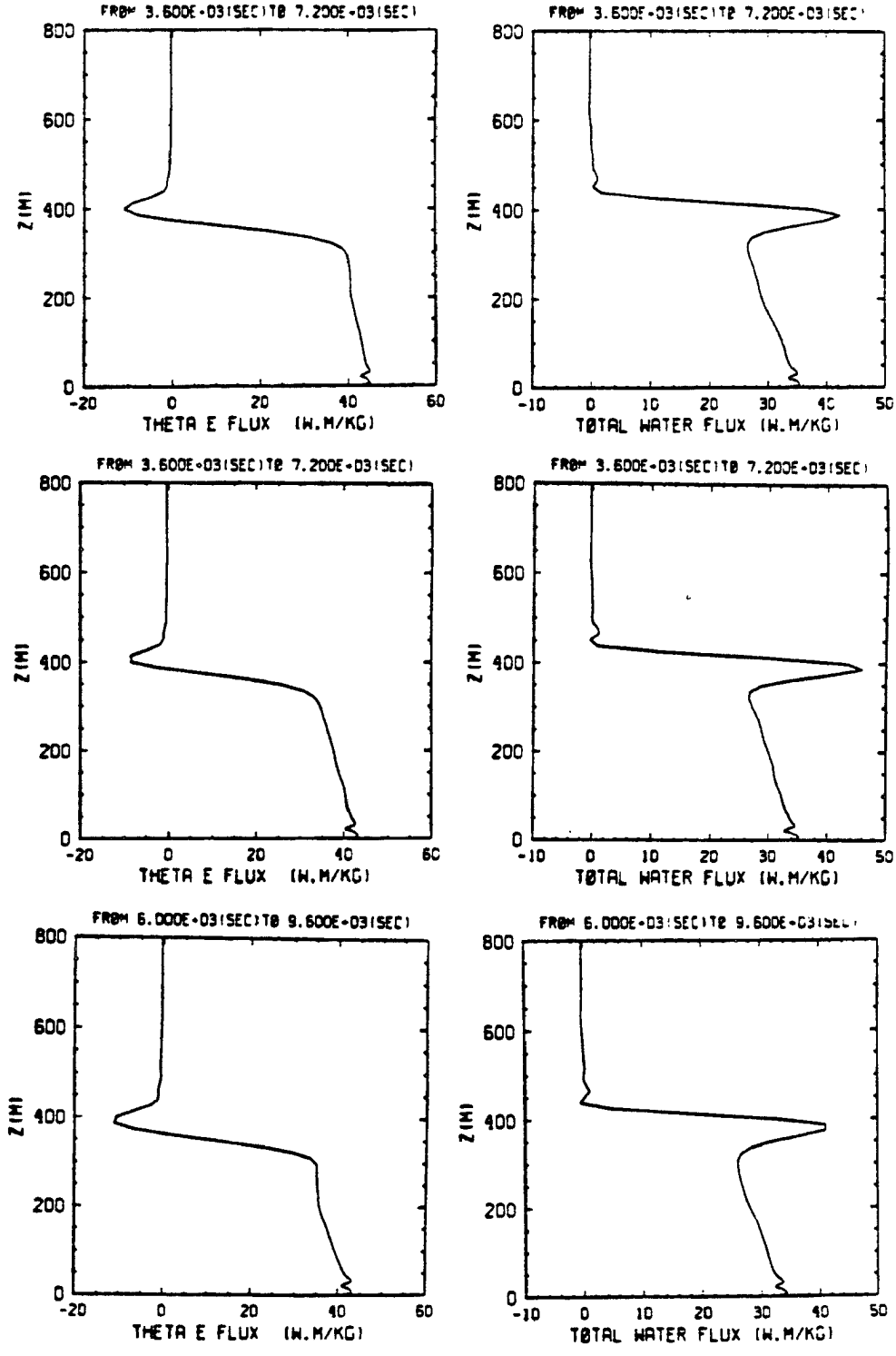

Figure 5.3a. The Θ and r flux profiles computed in a period of the last one hour for experiments . , B, C, D and E. The five rows are arranged in the order of experiments A, B, C, D and E.

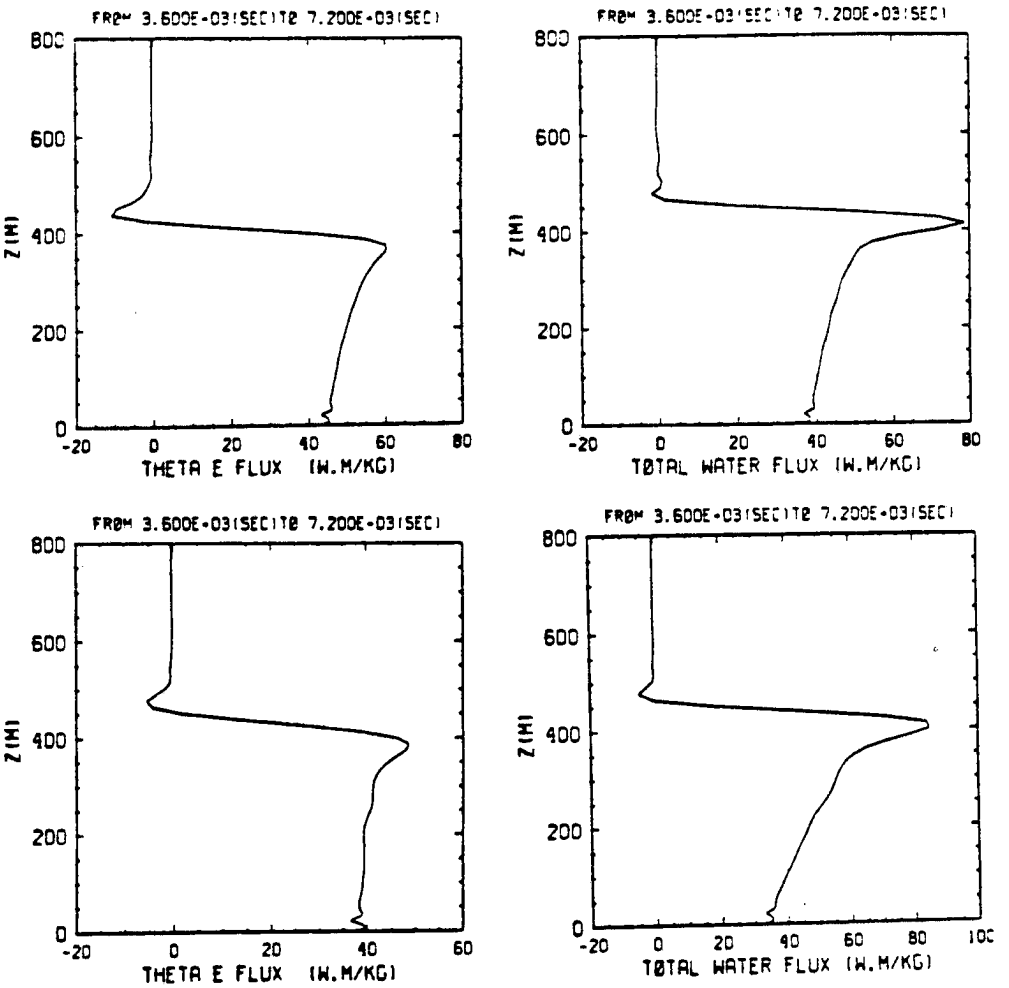

Figure 5.3a. (Continued)

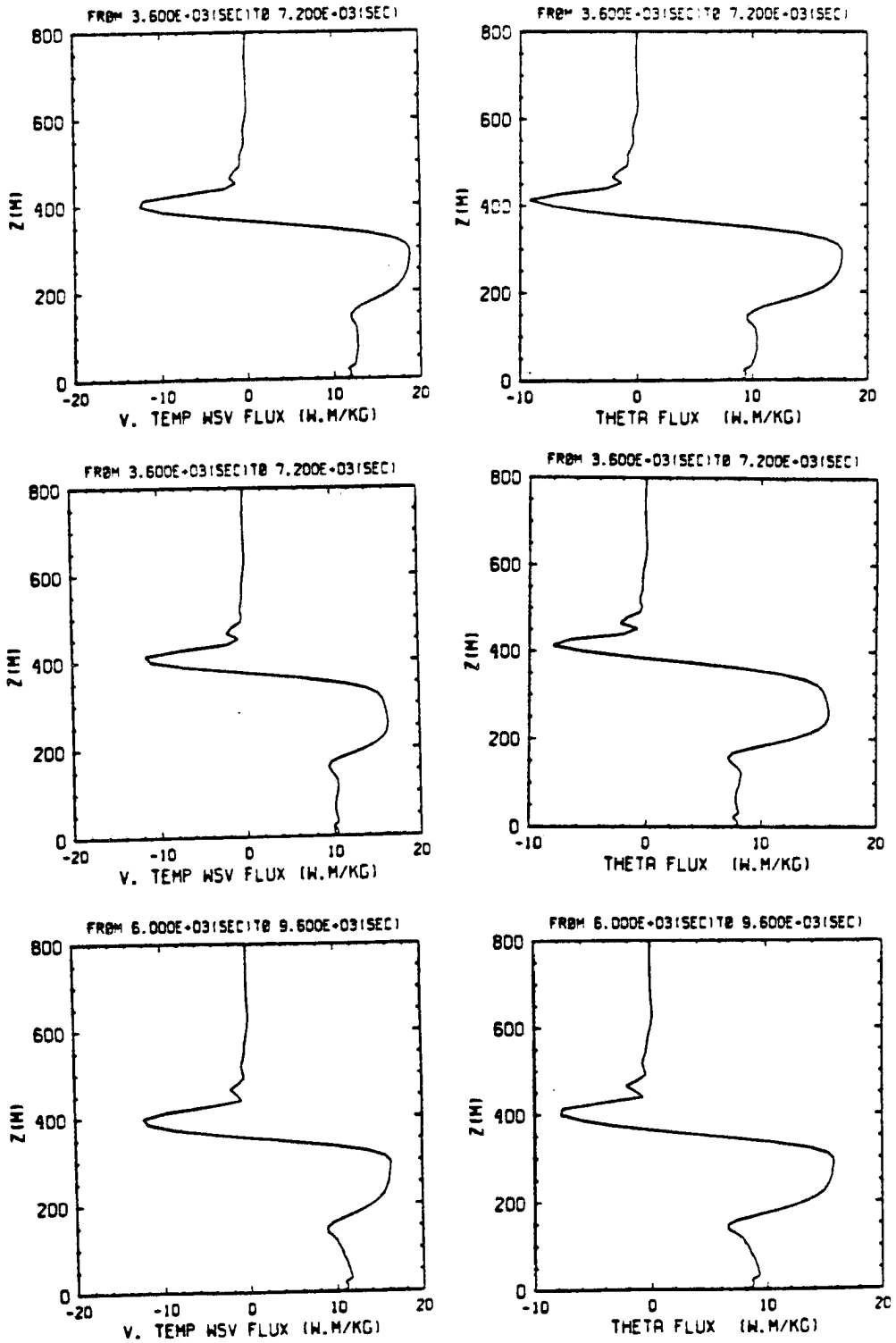

Figure 5.3b. Same as figure 5.3a except for the flux profiles of θ and ϑ.

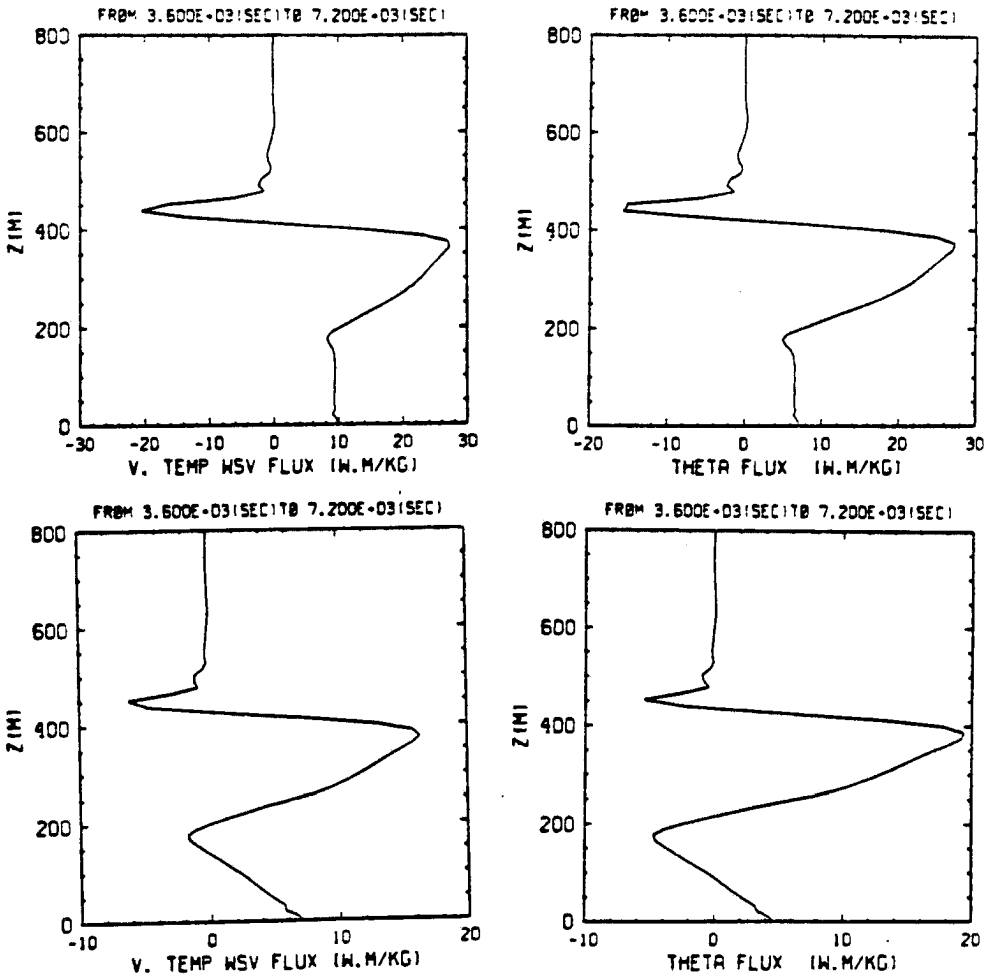

Figure 5.3b. (Continued)

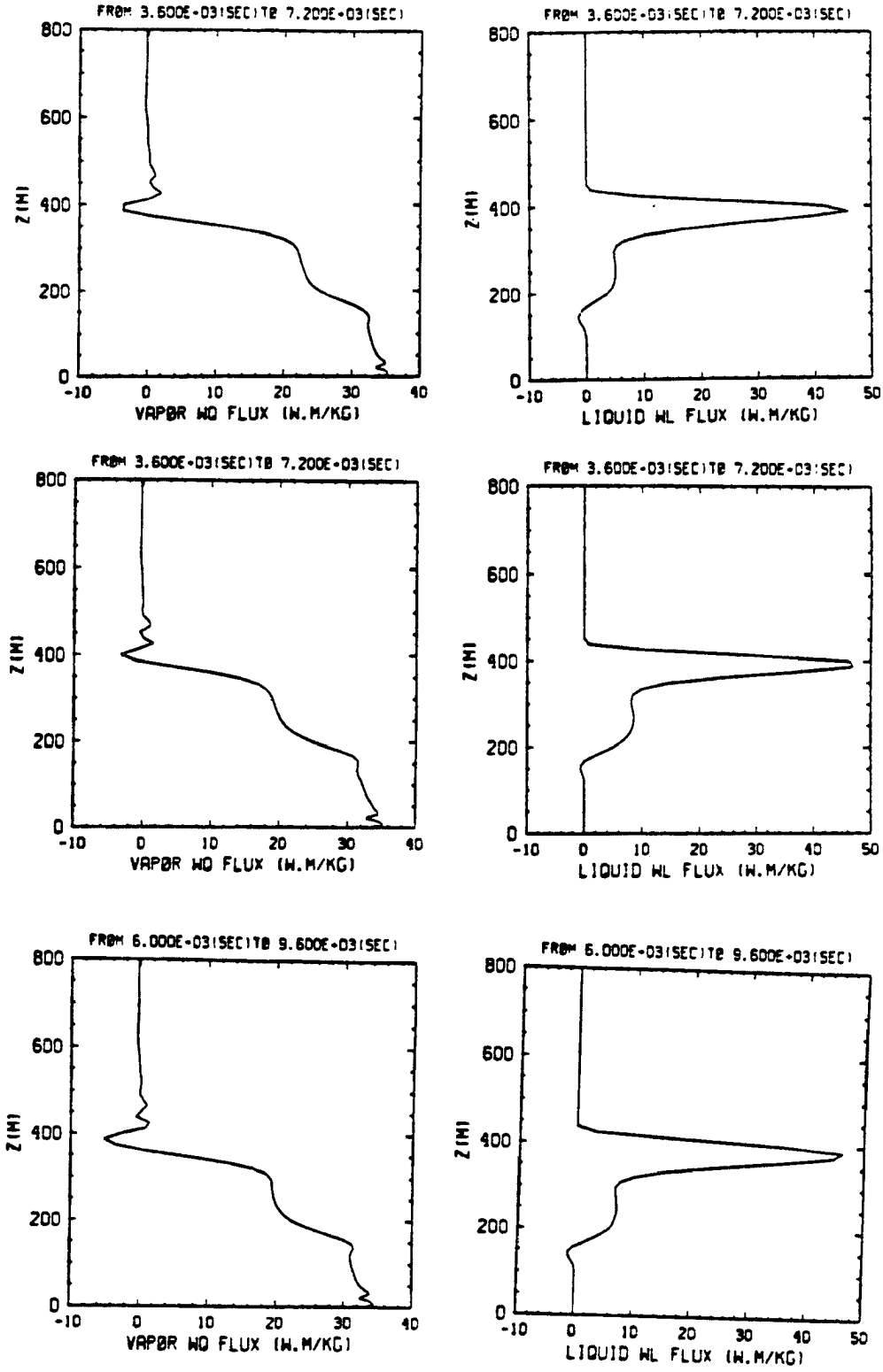

Figure 5.3c. Same as figure 5.3a except for the flux profiles of q and l.

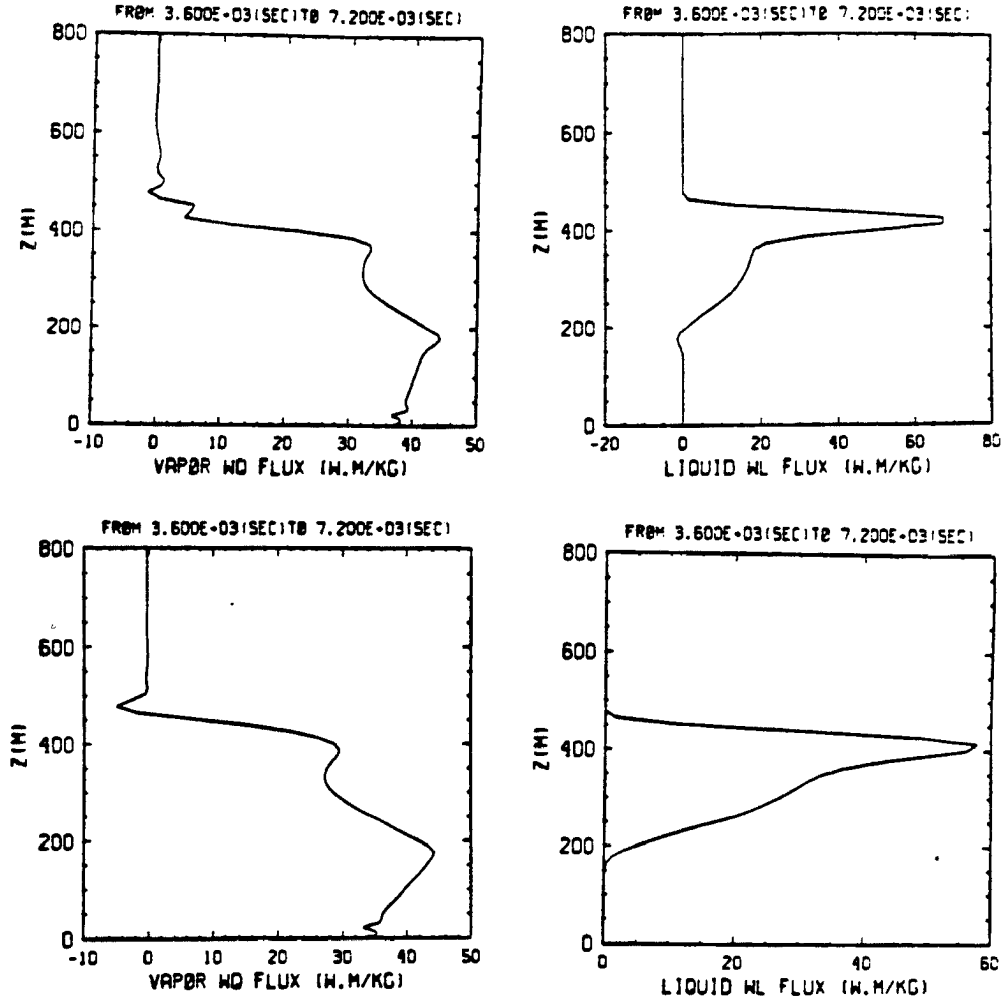

Figure 5.3c. (Continued)

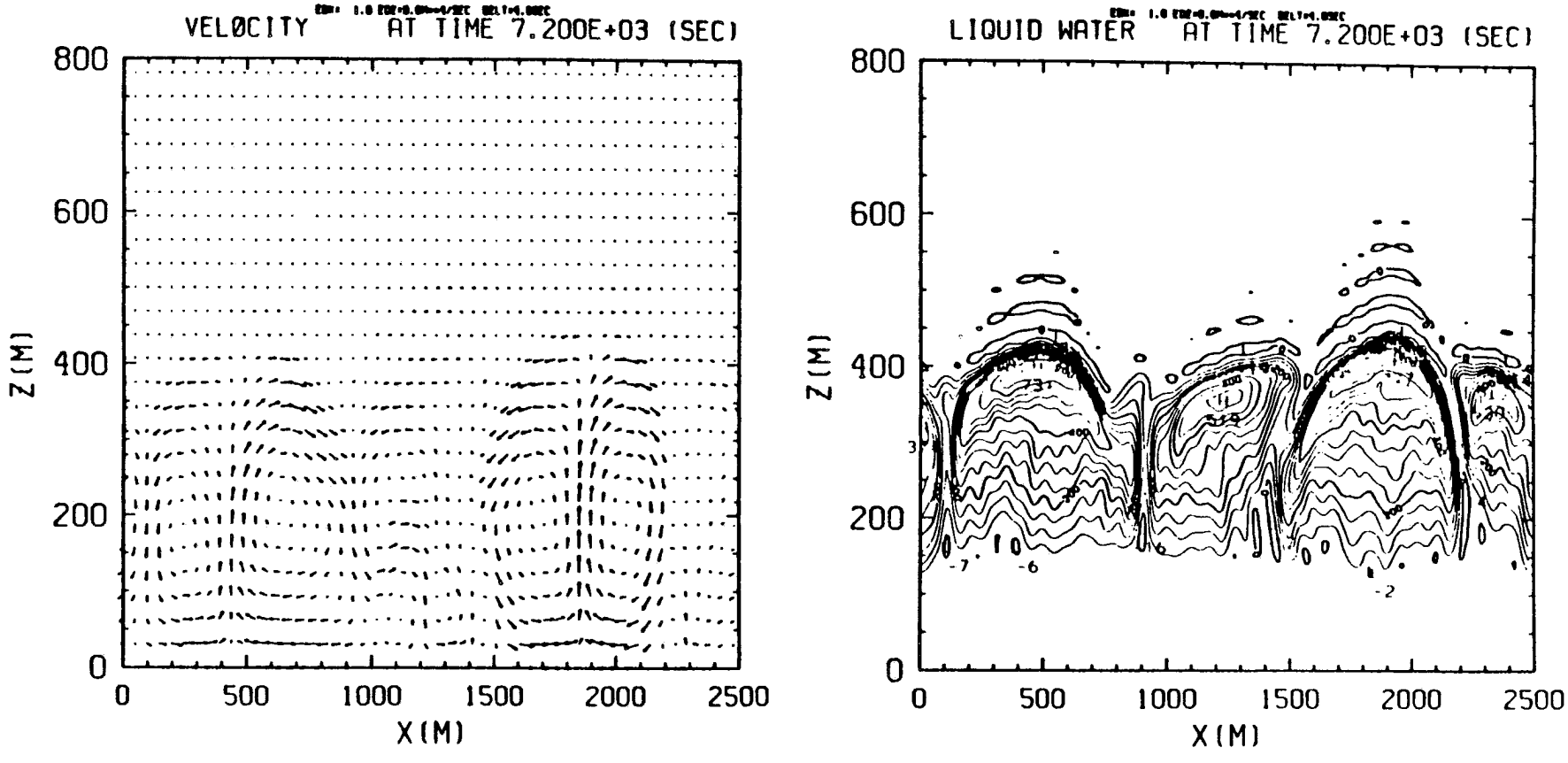

Figure 5.4. The velocity and the liquid water mixing ratio fields in the physical domain for experiment A. The velocity picture is presented in the left adjacent to the liquid water picture. Arrows represent wind velocity scaled by maximum velocity. The maximum velocity is 2.80 m s^{-1}. The liquid water mixing ratio in unit g kg^{-1} is scaled by 10^3.

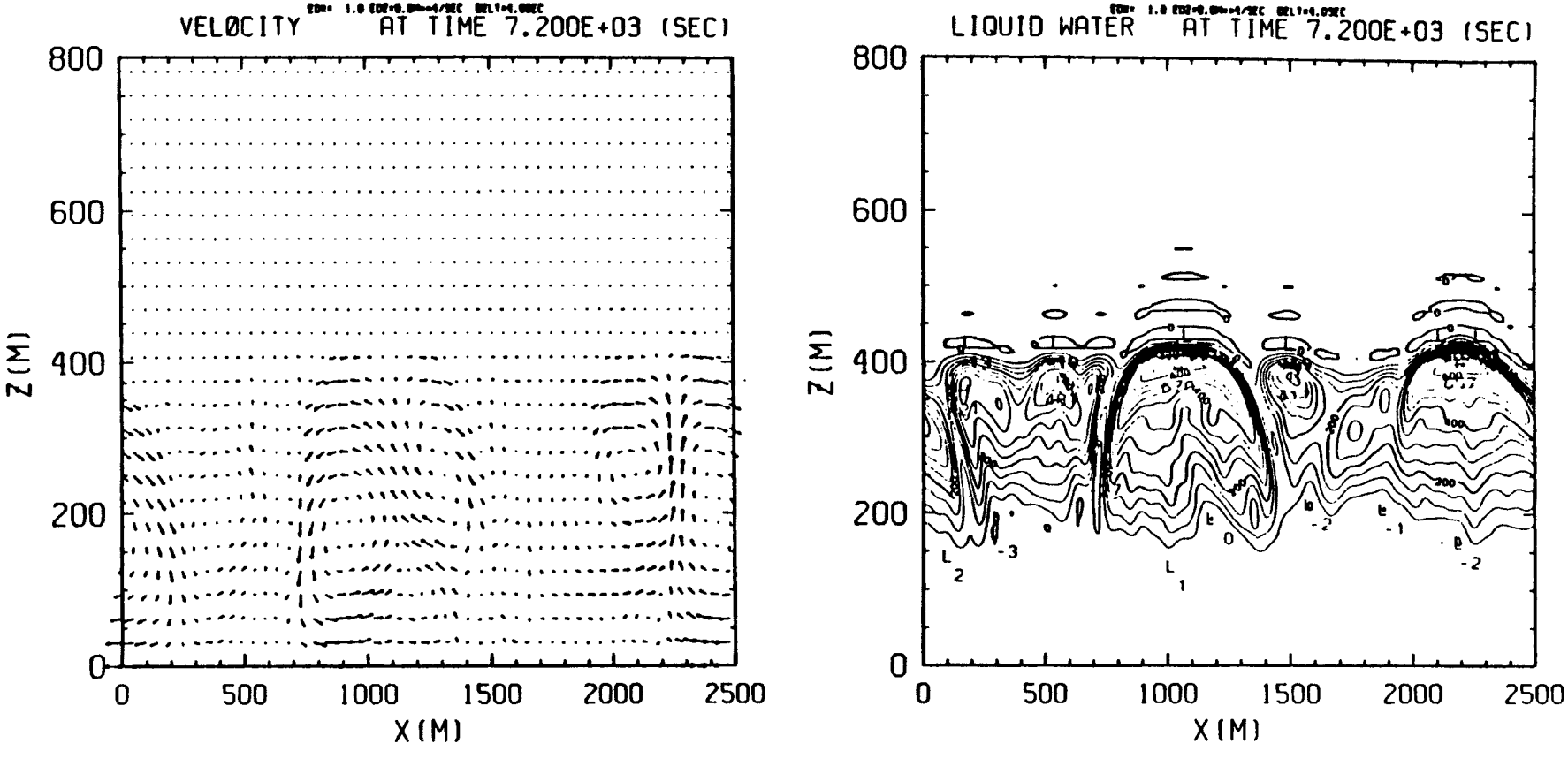

Figure 5.5. Same as figure 5.4 except for experiment B and the maximum velocity is 2.52 m s^{-1}.

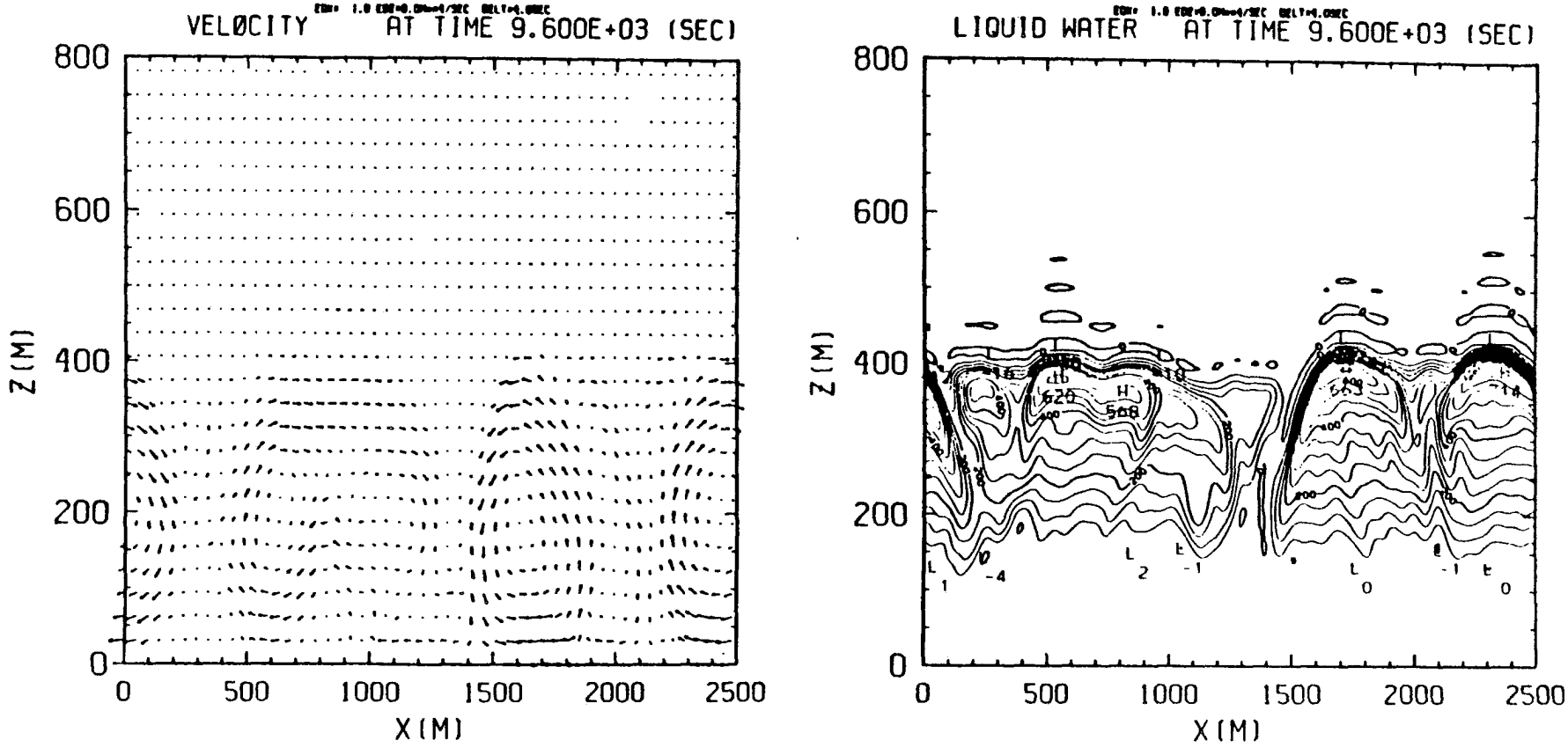

Figure 5.6. Same as figure 5.4 except for experiment C and the maximum velocity is 2.93 m s^{-1}.

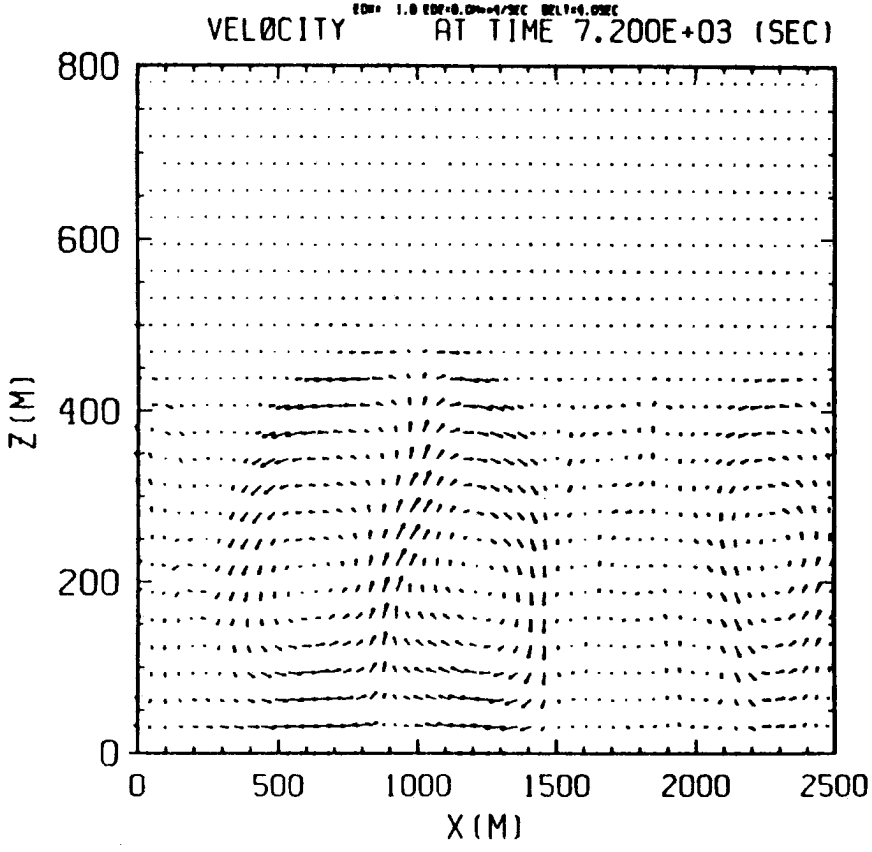

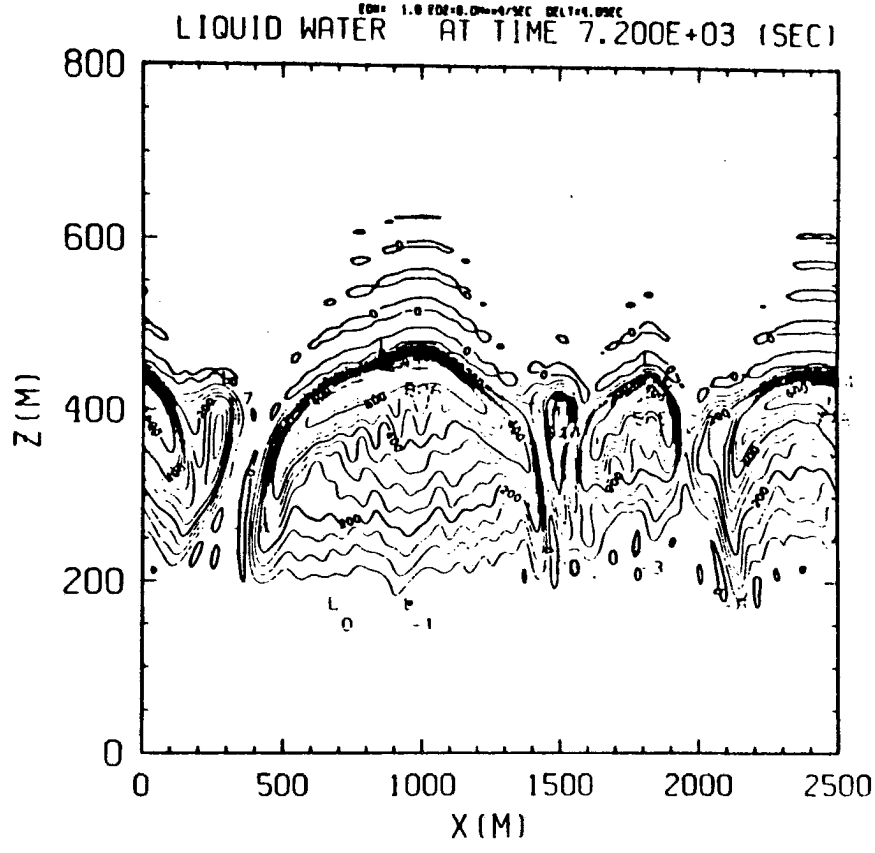

Figure 5.7. Same as figure 5.4 except for experiment D and the maximum velocity is 3.17 m s^{-1}.

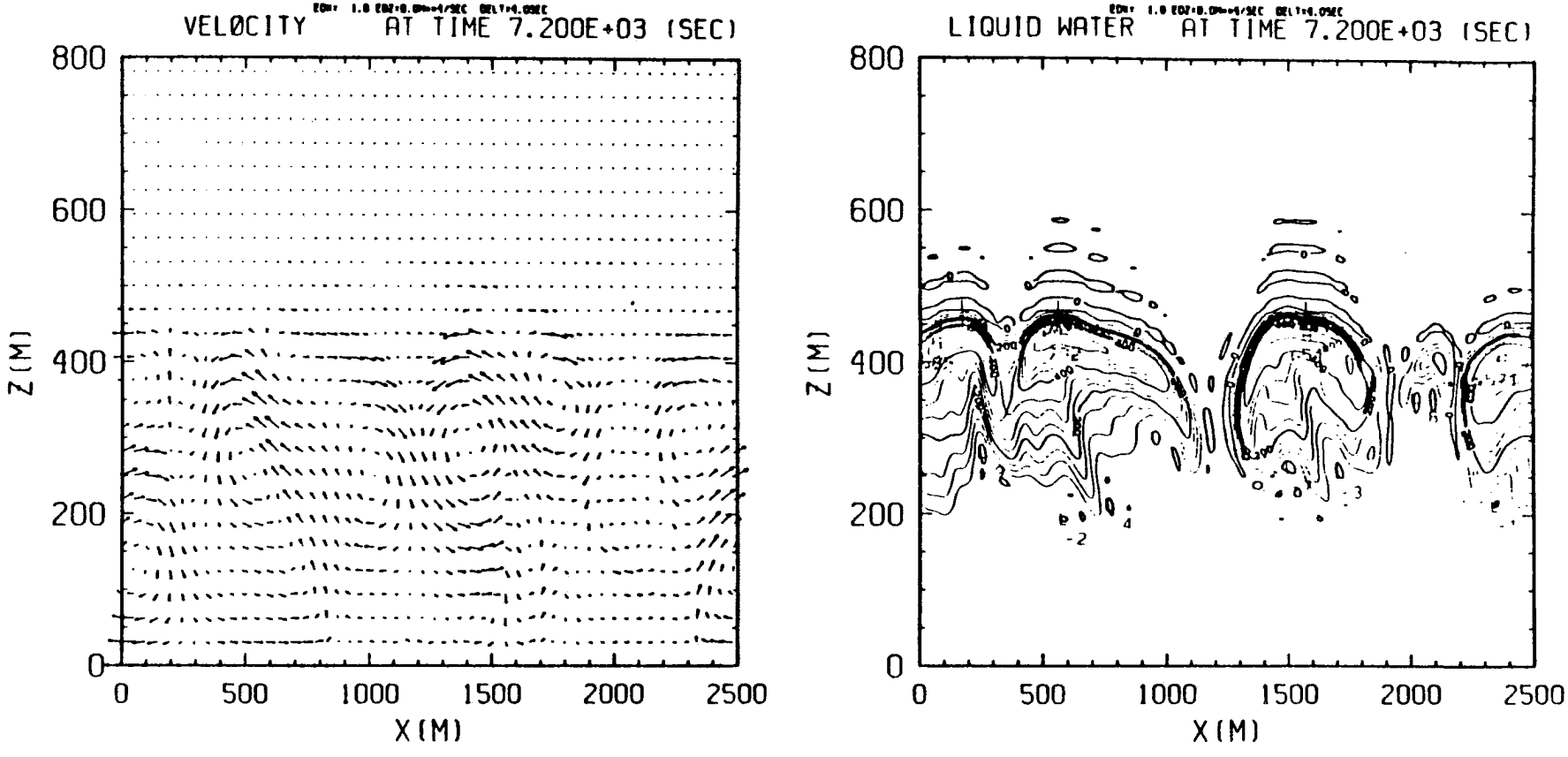

Figure 5.8. Same as figure 5.4 except for experiment E and the maximum velocity is 1.57 m s^{-1}.

cover the top 50m to 100m of the cloud cell. It should be noted that these clouds are purely buoyancy (radiation) driven because there is no initial background wind shear in the model. In experiments A, B, C and D (Figs. 5.6 through 5.9) there is only one cell of circulation in the vertical as revealed in the velocity field pictures. These circulations make the boundary layer well-mixed. The upward branch of the circulation in these experiments is in the center of the cloud cell while downward motion occurs near the side of the cell. The downdraft regions do not necessarily have a higher cloud base as predicted by the mixed layer model. The appearance of the stratocumulus cloud from experiment E (Fig. 5.8) is generally similar to the other experiments except for the motion field. There are two circulation cells in the vertical in experiment E as opposed to the one cell pattern seen in the rest of the experiments. These two cells of circulation are not decoupled in the vertical because the average Θ profile for experiment E (shown in Fig. 5.2) is still well-mixed. Also one would expect that the larger in-cloud buoyancy or heat flux should allow the motion to overcome the small negative flux region near the cloud base to reach the moist ocean surface. Finally, as observed in both Figs. 5.1 and 5.7, the cloud fraction in the region of the prescribed cooling in experiment D is not one hundred percent because of the formation of dome-shaped cloud cells. Some of the non-interactive cooling in experiment D will then inevitably be applied to clear regions between cloud domes. The fact that experiments A, B, C and D produce similar results implies cooling in the clear air between two cloud domes will not affect the boundary layer dynamics so long as the cooling is in the non-zero cloud fraction (turbulent) region.

From the results discussed above, there are two regimes of steady state behavior. One is from experiment E and others are from experiments A, B, C and D. The radiative forcings used in experiments A, B, C and D are all inside the non-zero cloud fraction region while the forcing in experiment E is in the zero cloud fraction capping inversion. The infrared radiation sensitivity of the model then is only in the vertical placement relative to cloud top. Once the radiative forcing is placed in the non-zero cloud fraction layer, the steady state of the model does not seem to be dependent on the horizontal or the vertical distribution of the cooling. This is probably due to the shorter time scale of the turbulence mixing (a few minutes as observed from the velocity field pictures). Before radiation can cool a local

region appreciably, turbulence must have already mixed downward the cloudy parcels. As a result, the spatial variability in radiative cooling has no impact on the boundary layer equilibrium dynamics so long as the cooling is inside the turbulent non-zero cloud fraction region. If there is no a priori reason to believe the present 2-D results will not carry through to the 3-D case, the discussion above indicates three things. First, since the present theory of radiative transfer does not support an infrared cooling occurring in the capping inversion (zero cloud fraction or non-turbulent region), it is then appropriate to use one of the cooling profiles other than E as the radiative forcing in the model. Secondly, the insensitivity of the model equilibrium state to the homogeneous or inhomogeneous infrared radiation in the non-zero cloud fraction region may suggest that a detailed radiative transfer calculation or observation to take the spatial variability of the cloud-topped cooling into account is not necessary. These horizontal variations as well as the cloud fraction (so long as it is not close to zero) where the radiative cooling is applied will not affect the equilibrium state physics. Finally, the model's infrared radiation sensitivity indicates a requirement for further observations and theoretical calculations (e.g. two-dimensional radiative transfer calculations) on the distribution of the radiative cooling in the region between zero and non-zero cloud fraction.

CHAPTER VI

ENTRAINMENT INSTABILITY

Entrainment is the process whereby fluid is exchanged across a density interface bounding a region of turbulent flow. Some laboratory simulations of the turbulent entrainment process have been reviewed by Turner (1973) with enlightening photographs. In general, it is observed that relatively motionless fluid is engulfed by turbulent flow penetrating across the mean density interface and is then mixed into the turbulent region. Smaller scale motion is rapidly damped by the interfacial density gradient so that a sharp interface is maintained which advances into the motionless fluid, causing the volume of the turbulent region to increase. Thus, the entrainment occurs in only one direction across the density interface into the turbulent region. Turner (1973) discussed the possible factors counteracting the growth of the turbulent boundary layer. One important factor in the application to geophysical fluid dynamics is the large scale subsidence in the atmosphere or the upwelling in the ocean. A steady state is possible in the presence of these large scale effects.

Entrainment processes in the cloud-topped marine boundary layer are more complicated than the classical laboratory experiments because of the existence of radiative cooling near cloud top and latent heat exchange (evaporation and condensation) inside the cloud. These additional diabatic effects not only influence the entrainment process near the cloud top but also regulate the turbulence in the boundary layer. As a result, a complete study of the entrainment problem in the marine boundary layer must take the dynamical effect (turbulence), the thermodynamical effect (diabatic forcings), large scale mean conditions as well as their interactions into account. Section 6.1 discusses the effect of evaporative cooling on mixtures of saturated and unsaturated parcels. The interaction between evaporative cooling and dynamics is studied in section 6.2 by the initial value technique. The possible missing ingredient in Lilly's original hypothesis is also discussed. Section 6.3 describes simulations

in which the effects of diabatic forcings, turbulence and large scale mean conditions are all included. A case with strong entrainment but without stratocumulus breakup is presented in section 6.4.

6.1 The effect of evaporative cooling

Central to the problem of entrainment instability is that a mixture of saturated cloudy air with unsaturated overlying air may be negatively buoyant under certain conditions (e.g. a large negative Θ jump across the cloud top). The continuous free penetration of the negatively buoyant parcels can then lead to the destruction of the stratocumulus layer. All existing entrainment instability theories emphasize the importance of evaporative cooling of the mixed parcel and its possible feedback on the dynamics. We now consider the effect of evaporative cooling based on (2.2)–(2.8), the governing equations of the thermodynamic theory.

We shall consider mixtures of a saturated parcel with an unsaturated parcel. The saturated parcel may be either a cloudy parcel with $\Theta = 305$ K, 0.5 g kg^{-1} liquid water mixing ratio and 7.4 g kg^{-1} water vapor mixing ratio or a cloud free parcel with the same Θ and q. The unsaturated parcels are also of two kinds. The first kind is an unstable one with $\Theta = 293$ K and $q = 0.5$ g kg^{-1}. The second is a stable one with $\Theta = 307$ K and $q = 3.5$ g kg^{-1}. Observations indicate that these saturated and unsaturated parcels are quite typical of the marine boundary layer. Fig. 6.1 illustrates the relative humidity, the ϑ difference and the amount of the evaporative cooling due to the presence of the cloud liquid water as a function of the fraction (χ) of unsaturated air involved in the mixture. The thin (solid, dashed and dotted) lines in Fig. 6.1 are the results for the mixture of the unstable parcel with the saturated cloudy and cloud free parcels. Similarly, heavy lines are for the mixture of saturated parcels with the stable parcel. The solid curves (both thin and heavy) are the relative humidity of the mixture of the cloudy parcel with the two unsaturated parcels. The dotted (thin and heavy) lines are the ϑ difference (the cloudy parcel as a reference) resulting from the mixture of unsaturated parcels with the cloud free saturated parcel. The dashed lines are the ϑ difference from the mixture of the cloudy parcels. The difference between the dotted and dashed curves in each case is the amount of evaporative cooling

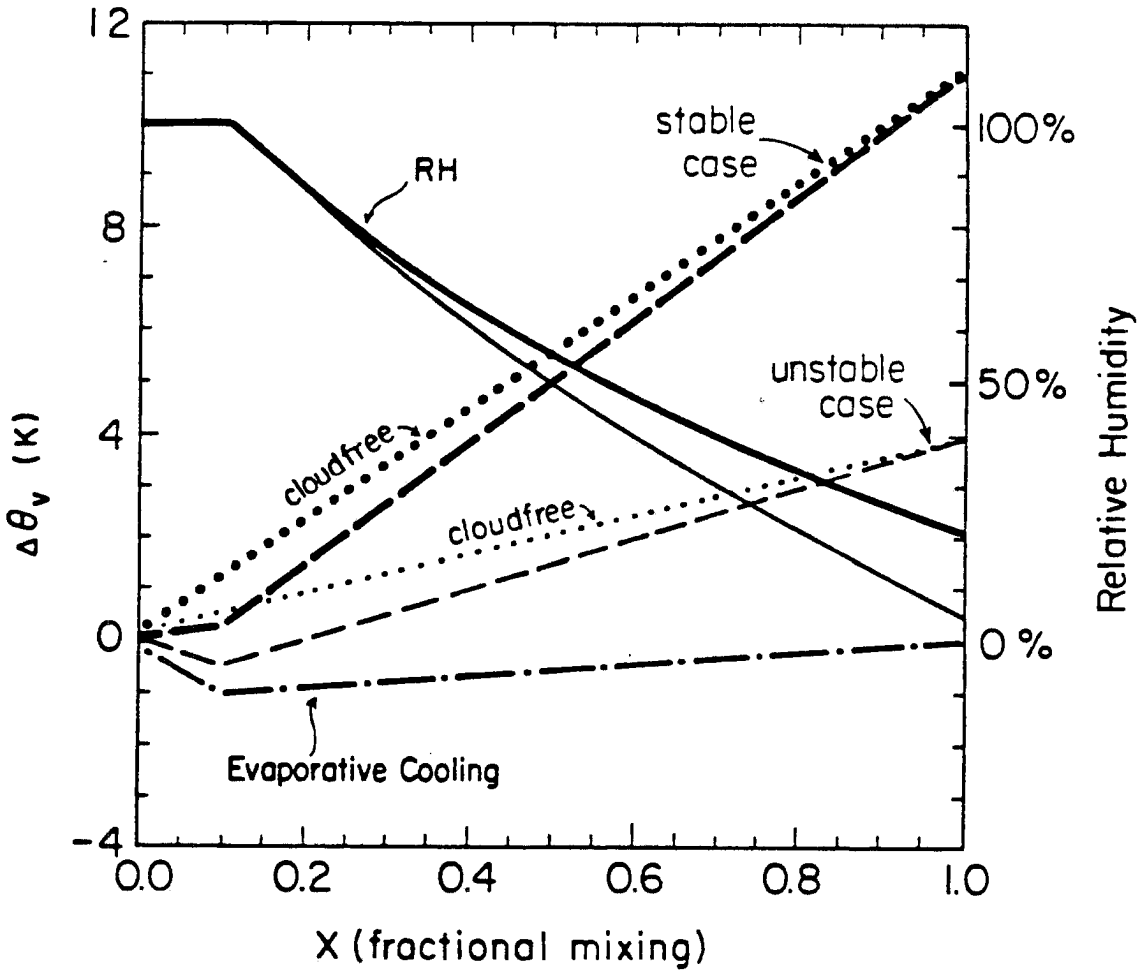

Figure 6.1. The relative humidity, the ϑ difference and the amount of evaporative cooling against the fraction (x) of the unsaturated air involved in the mixture for the experiments mentioned in the text. The mixing ratio of liquid water content in the cloudy parcel is 0.5 g kg^{-1}.

(dash dotted curve) due to the presence of 0.5 g kg^{-1} liquid water. Note that the amount of evaporative cooling as a function of mixing fraction (χ) is identical for both kinds of unsaturated parcels. The similarity in evaporative cooling indicates the generality of the following discussion.

Fig. 6.1 suggests that mixtures of stable air with either cloudy or cloud free parcels have positive buoyancy for all mixing fractions χ (heavy dotted and dashed curves). Therefore, free penetration of the mixed parcel is impossible and the cloud layer is stable. On the other hand, the negatively buoyant mixture in the unstable case is realized only when the fractional of mixing involved is small ($\chi \leq 0.2$). The maximum negative buoyancy of -0.6 K occurs at $\chi = \hat{\chi} \simeq 0.1$ where the mixed parcel is just saturated. Once all the liquid water is evaporated and the mixed parcels become unsaturated ($\chi \geq \hat{\chi}$), further addition of the unsaturated air simply warms the mixture and results in positive buoyancy. Thus, free penetration of the mixed air parcel in the unstable situation will crucially depend on the fraction of mixing involved. The mixed parcels may not always be negatively buoyant as predicted by the classical theory (Lilly, 1968; Randall, 1980b; Deardorff, 1980a). The low liquid water content of stratocumulus cannot produce enough evaporative cooling and the saturation of the mixture is not guaranteed. The decrease in ϑ due to evaporation, as given in the dash dotted curve, is large in the whole range of fractional mixing except near the two extremes $\chi \simeq 0$ and $\chi \simeq 1.0$. Typical infrared radiative cooling in the marine boundary layer is about 5 K hr^{-1}. If the turbulent mixing time scale is small, then the virtual temperature reduction by radiative cooling is important only when little mixing is occurring ($\chi \simeq 1.0$ or $\chi \simeq 0$). However, in both kinds of overlying air parcels considered here, negative buoyancy can be most easily produced by radiative or evaporative cooling when χ is small. In other words, downdrafts will be formed preferentially from cloudy air which has undergone little mixing with the inversion air. As a result, the downdraft regions do not necessarily have to have higher cloud bases (e.g. Fig. 5.4).

So far we have only considered the effect of evaporative cooling. Fig. 6.1 indicates that due to the low liquid water content of stratocumulus, a saturated and negatively buoyant parcel may not always be possible from the mixture of cloud with an unstable parcel. Since the resultant positive or negative buoyancy in the mixture is dependent on the mixing

fraction, thermodynamical analysis alone is insufficient to determine the stability of the stratocumulus clouds. We need interaction of evaporation and dynamics to investigate the entrainment problem. The hypothesis of entrainment instability will be further tested along this direction in the next section.

6.2 Initial value problems

To test the hypothesis of entrainment instability, we will perform initial value experiments for the U2 and S cases. In these initial value experiments, a cold anomaly of 1 K is assumed to be generated just below the inversion base (450m). In stratocumulus, cold bubbles such as this can be generated in about 10 minutes by an 80 W/m^2 infrared radiative flux divergence across cloud top if there is no turbulence. We will use this cold bubble as a mechanism to trigger entrainment instability in the U2 case, if such an instability exists. The results from the U2 and S cases for these initial value problems are shown in Figs. 6.2 through 6.6. The output is displayed in 10 minute intervals. The S results are presented on the right in these figures adjacent to the U2 results (on the left). The Θ fields with the contour interval of 0.25 K superimposed on the velocity fields (in arrows) are illustrated in the upper part of Figs. 6.2 through 6.6. The lower part of these figures show the cloud liquid water content. The initial cold bubble and the horizontally homogeneous cloud can be clearly seen in Fig. 6.2. The Θ, velocity and cloud liquid water content at 10 minutes and 20 minutes are presented in Figs. 6.3 and 6.4. In the Θ and the velocity fields part of the figures we note how the cold bubble sinks to the surface to form secondary symmetric circulations while exciting gravity wave oscillations in the capping inversion. The cloud liquid water content reveals the appearance and the disappearance of a cloud hole in the center of the domain near cloud top. The cloud hole appears at 10 minutes because large amounts of dry air are brought down by the initial cold bubble. The disappearance of the cloud hole as seen from cloud liquid water patterns in Fig. 6.4 indicates a dramatic decrease in the entrainment of dry air into the cloud layer in both the U2 and the S cases from minute 10 to minute 20. Similar physical fields at 30 and 40 minutes are shown in Figs. 6.5 and 6.6. From these two figures we can see the propagation of the secondary circulation toward the boundary. The cloud hole at this time is near cloud base; it subsequently disappears

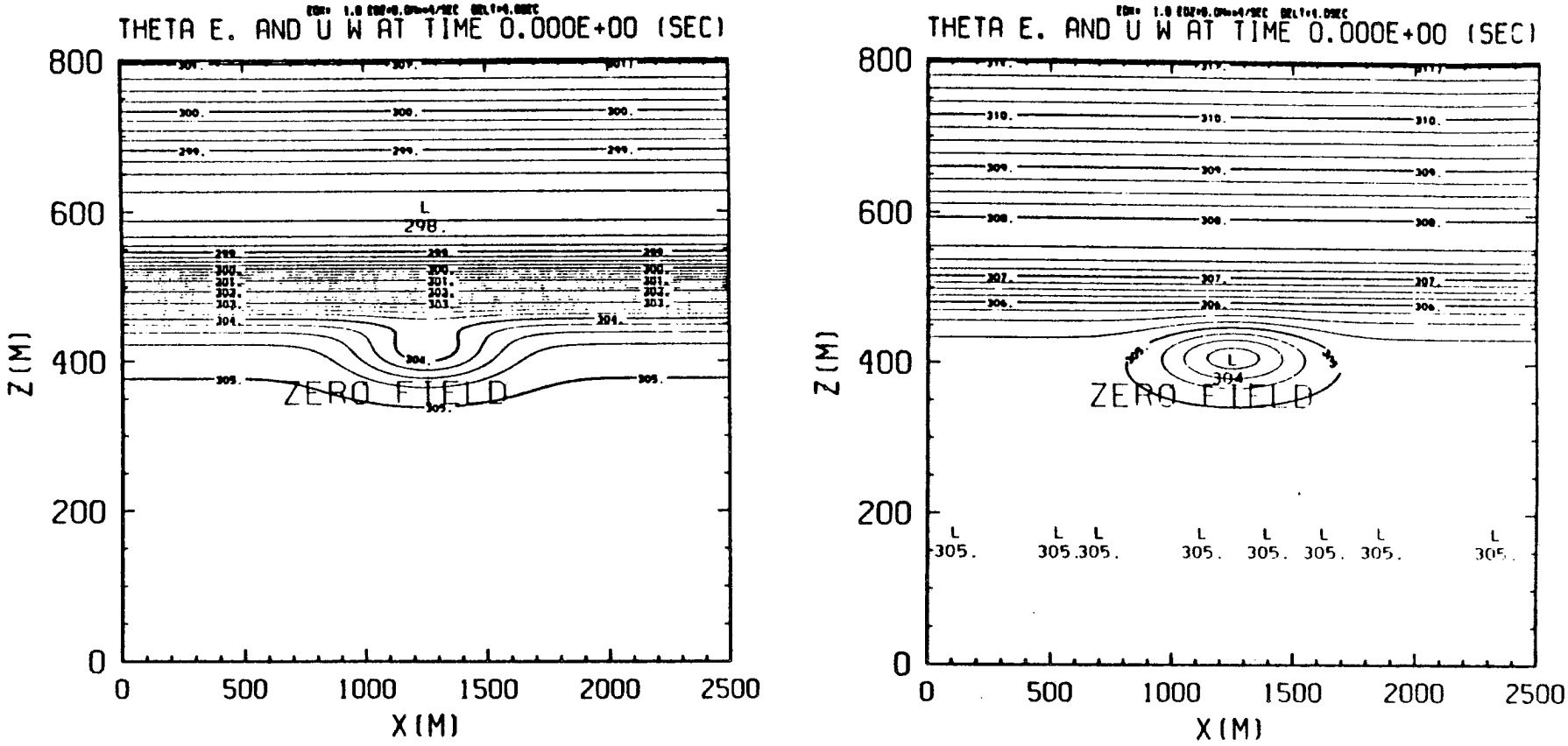

Figure 6.2. The initial Θ, velocity (upper pictures) and liquid water mixing ratio (lower pictures) for the U2 and S cases in the initial value problems. The U2 case is shown in the left adjacent to the S case. The liquid water mixing ratio in unit g kg^{-1} is scaled by 10^3.

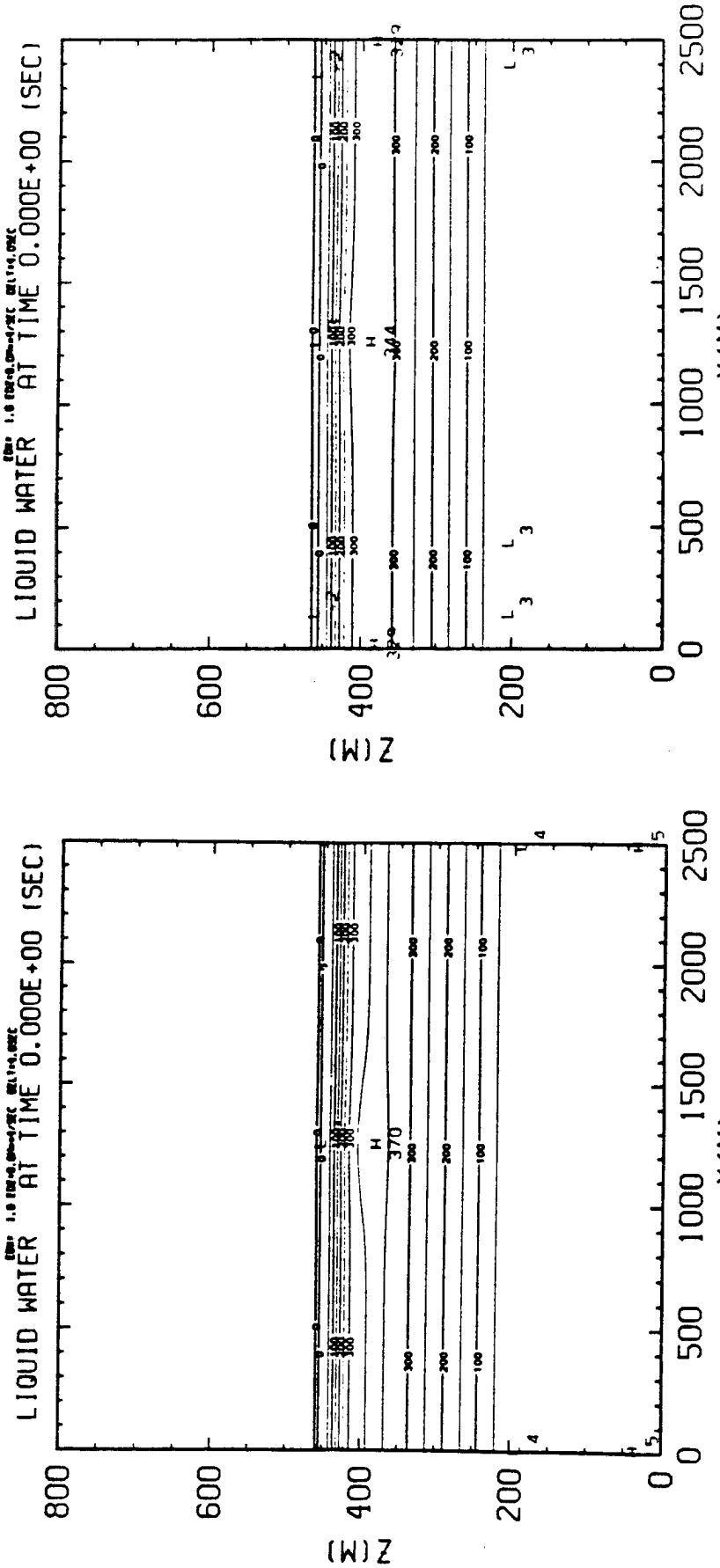

Figure 6.2. (Continued)

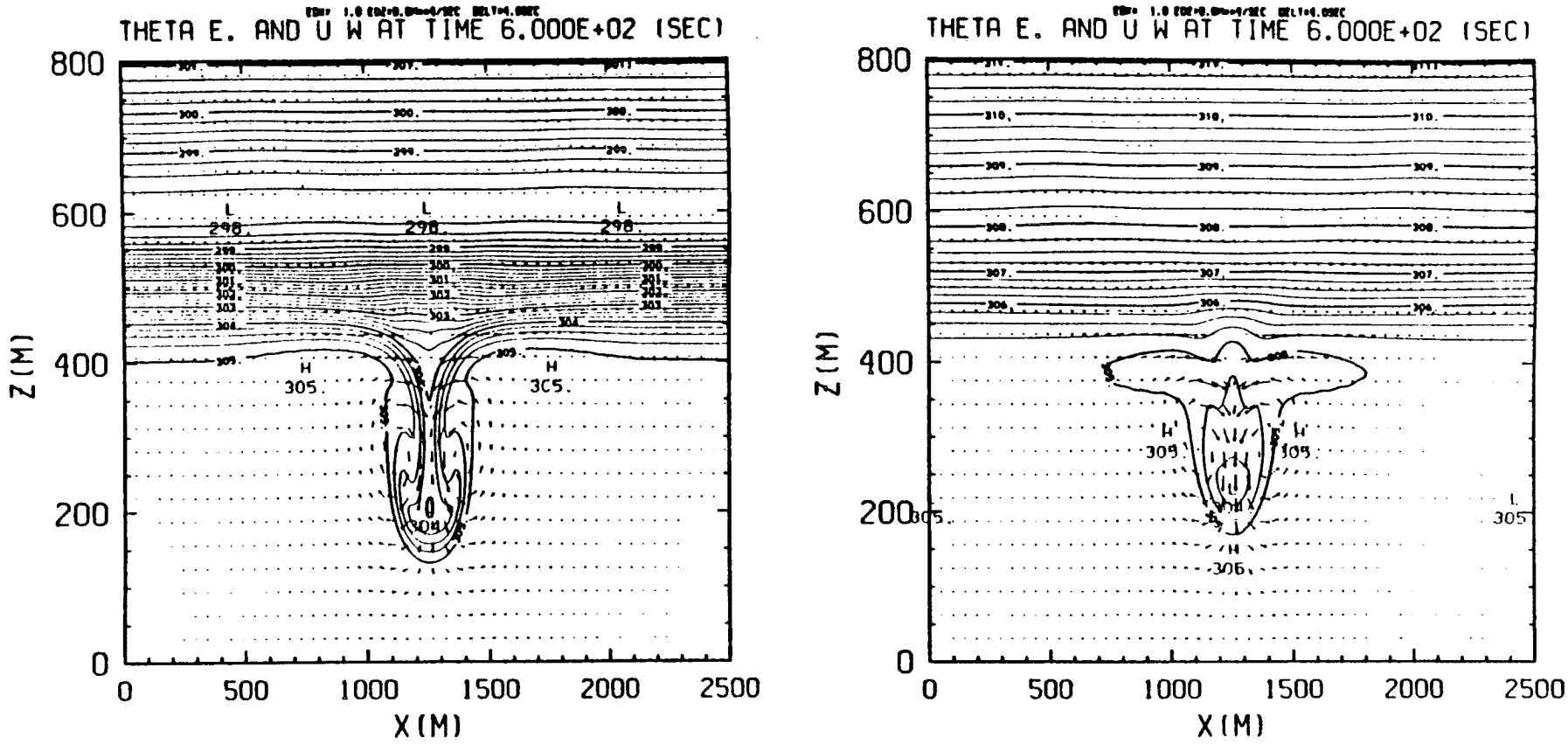

Figure 6.3. The Θ, velocity (upper pictures) and liquid water mixing ratio (lower pictures) for the U2 and S cases in the initial value problems at time equal to 10 minutes. The U2 case is shown in the left adjacent to the S case. Arrows represent wind velocity scaled by maximum velocity. The maximum velocity is 1.23 m s^{-1} for the U2 case and 0.85 m s^{-1} for the S case.

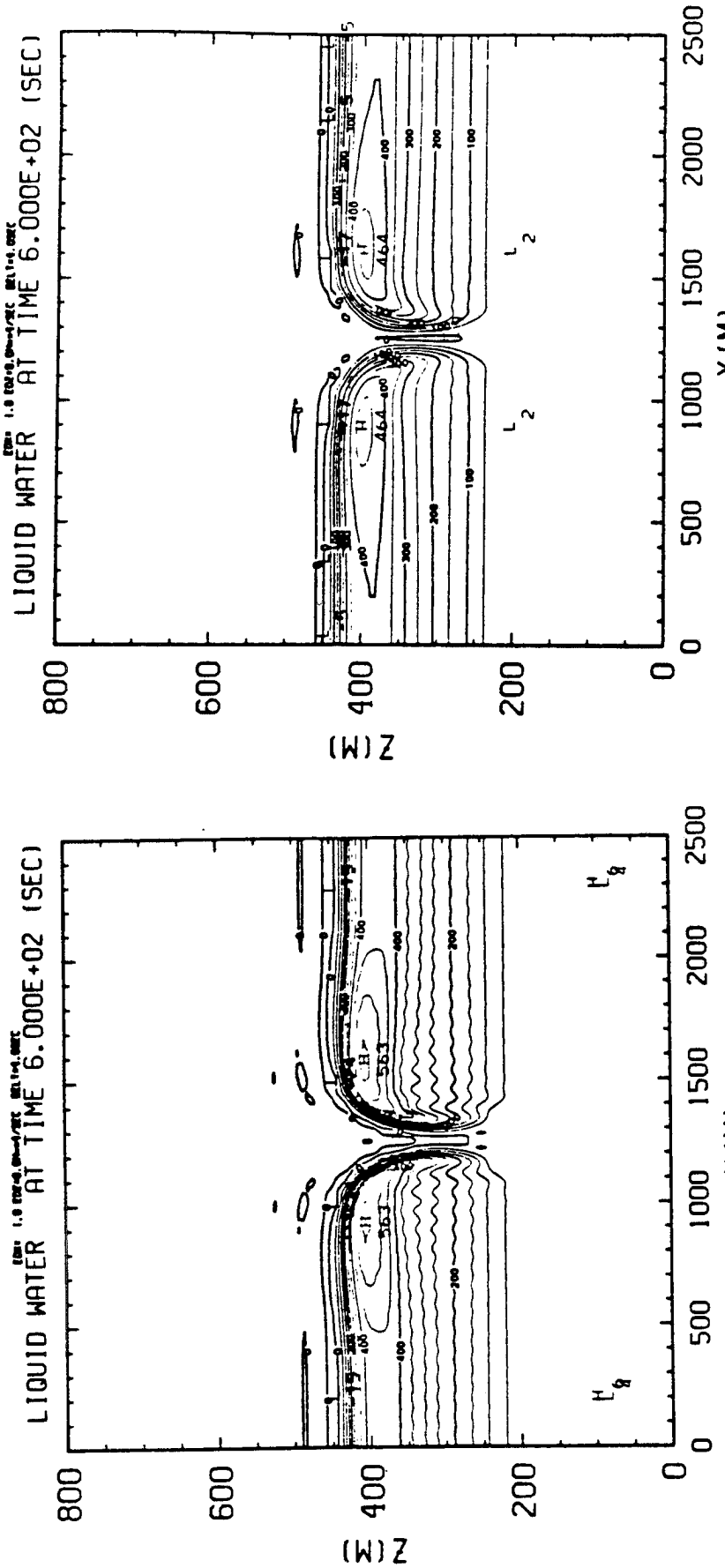

Figure 6.3. (Continued)

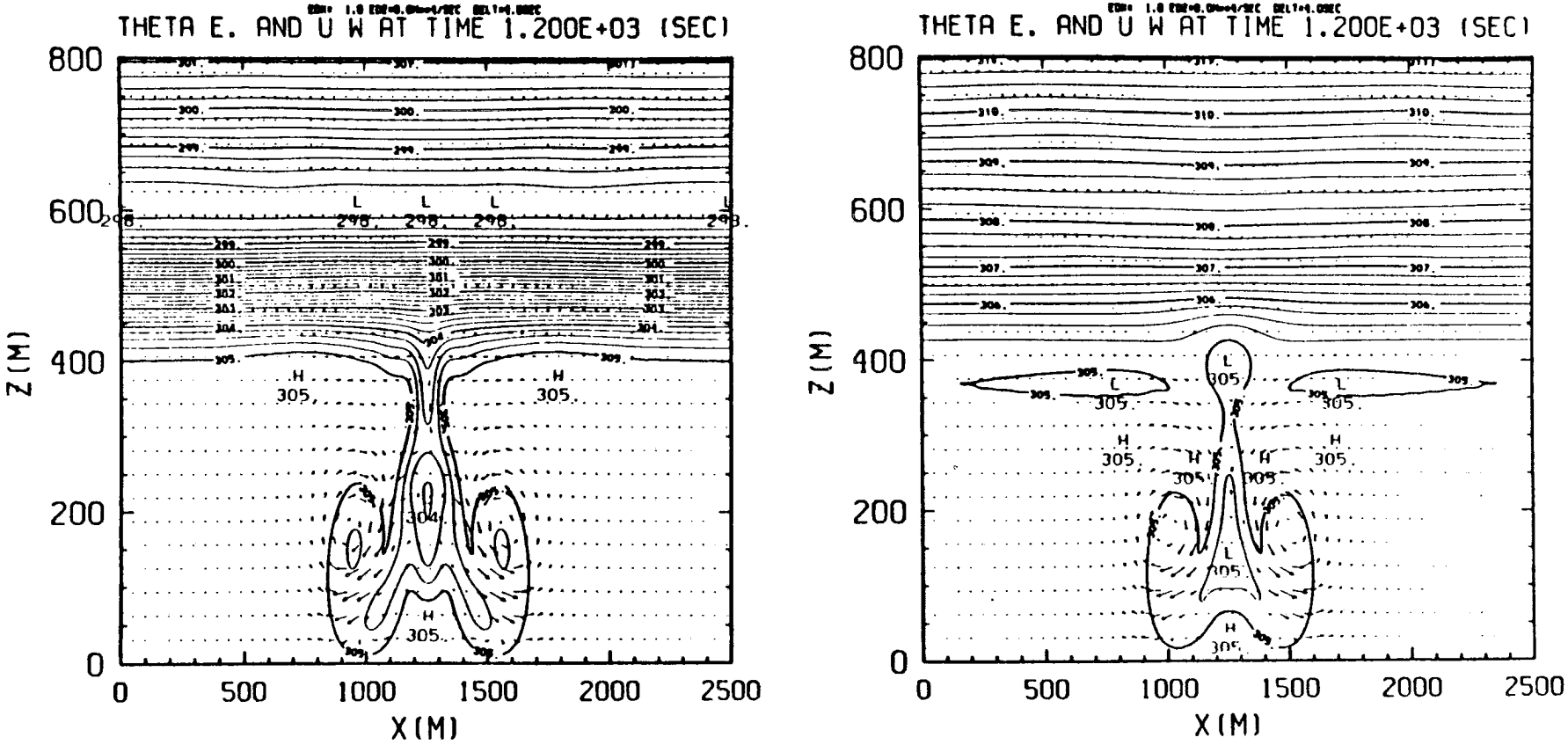

Figure 6.4. Same as figure 6.3 except at 20 minutes. The maximum velocity is 1.06 m s^{-1} for the U2 case and 0.97 m s^{-1} for the S case.

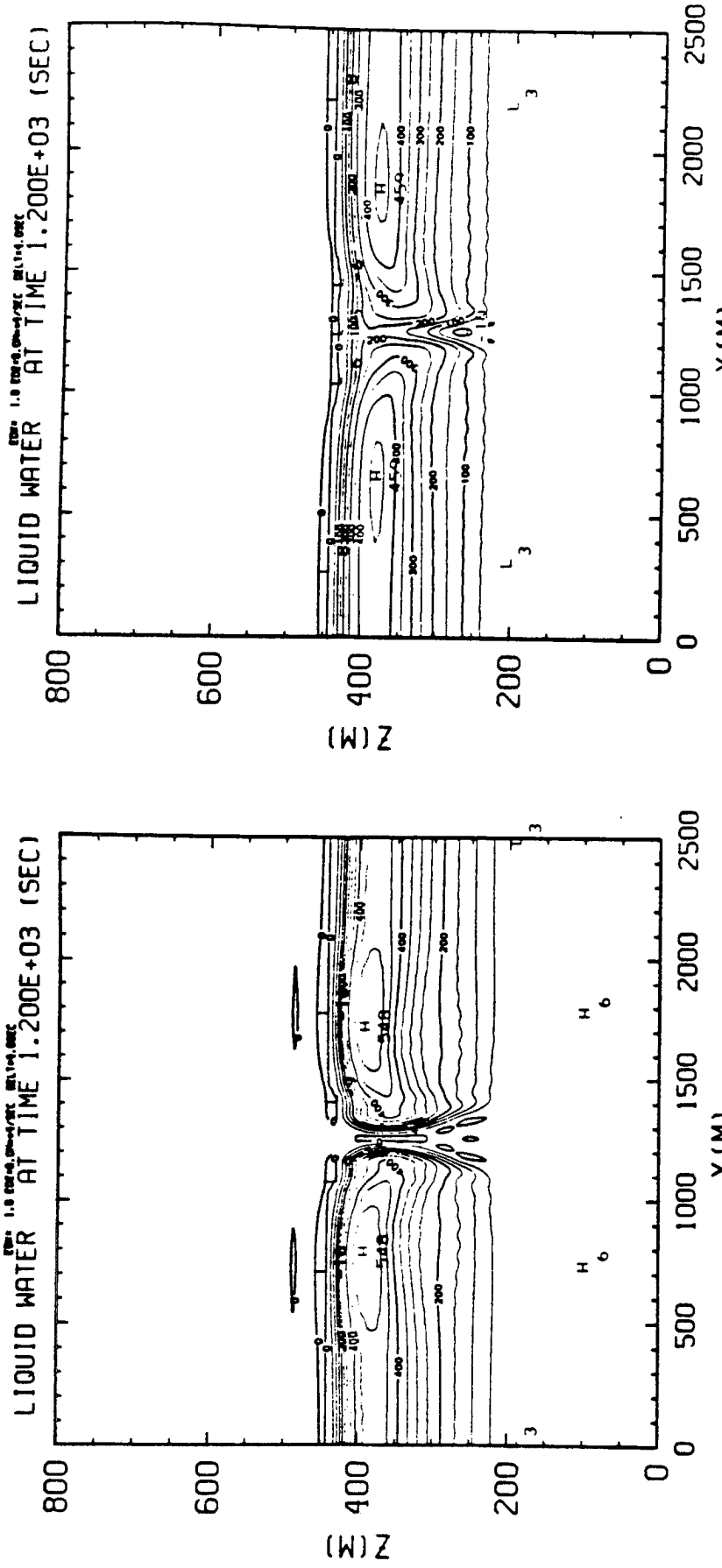

Figure 6.4. (Continued)

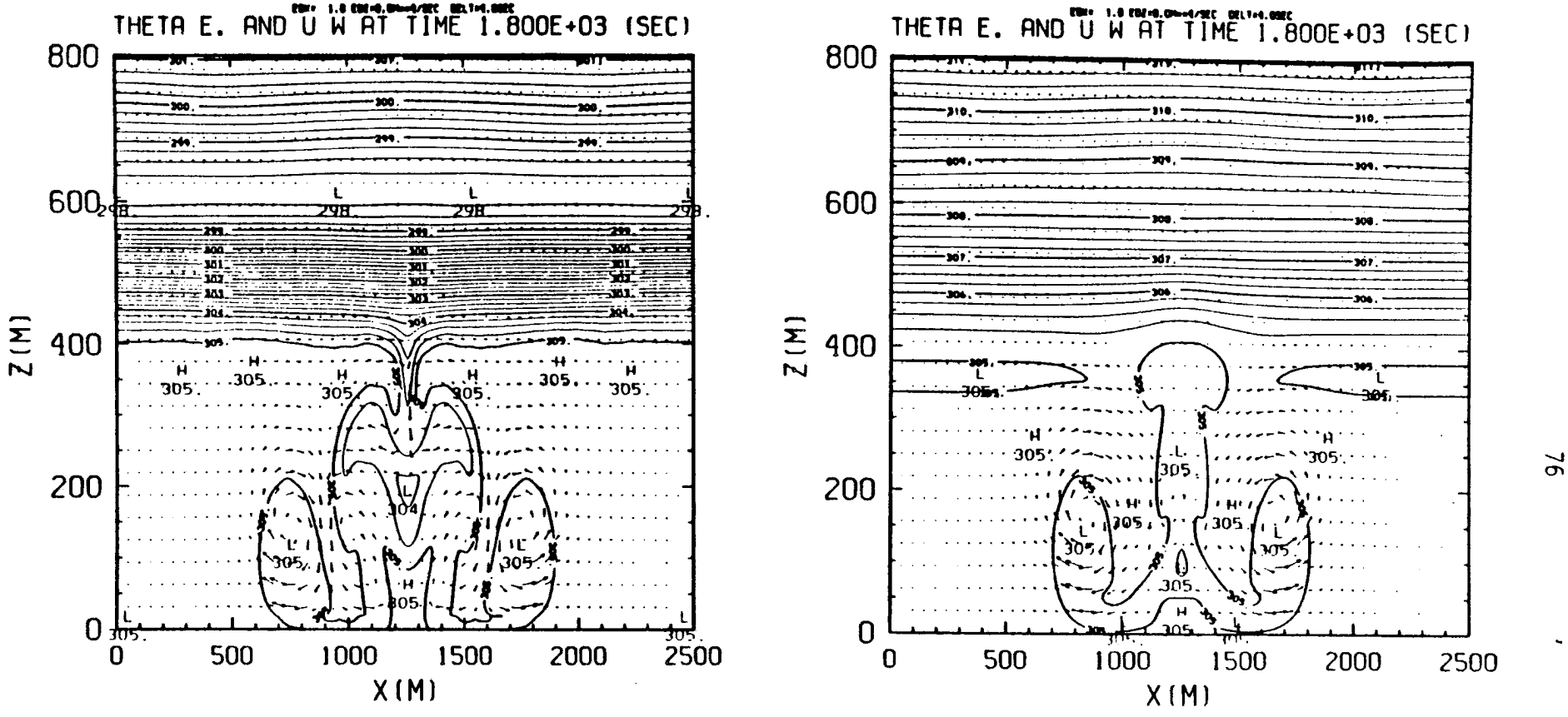

Figure 6.5. Same as figure 6.3 except at 30 minutes. The maximum velocity is 0.84 m s^{-1} for the U2 case and 0.78 m s^{-1} for the S case.

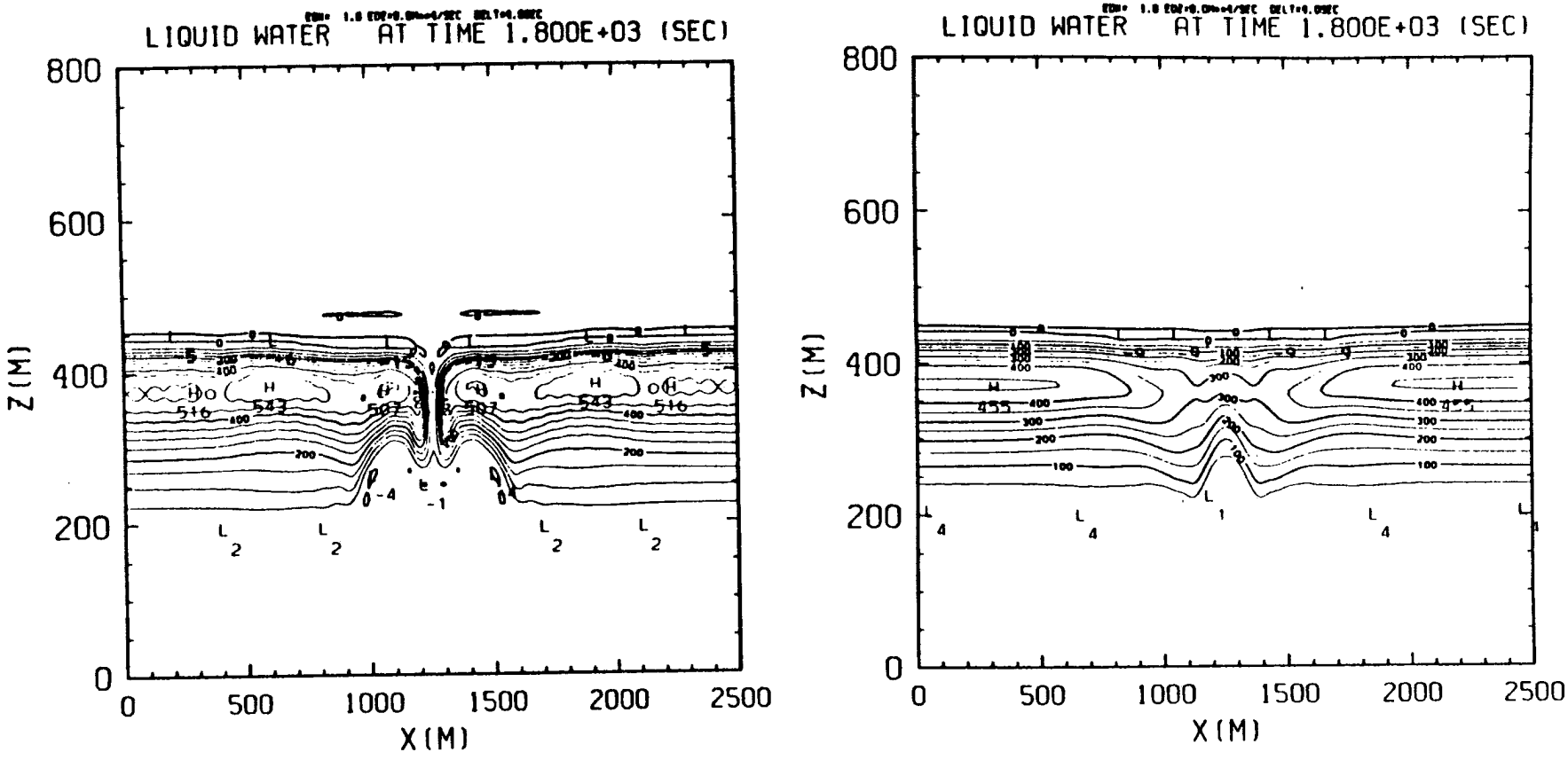

Figure 6.5. (Continued)

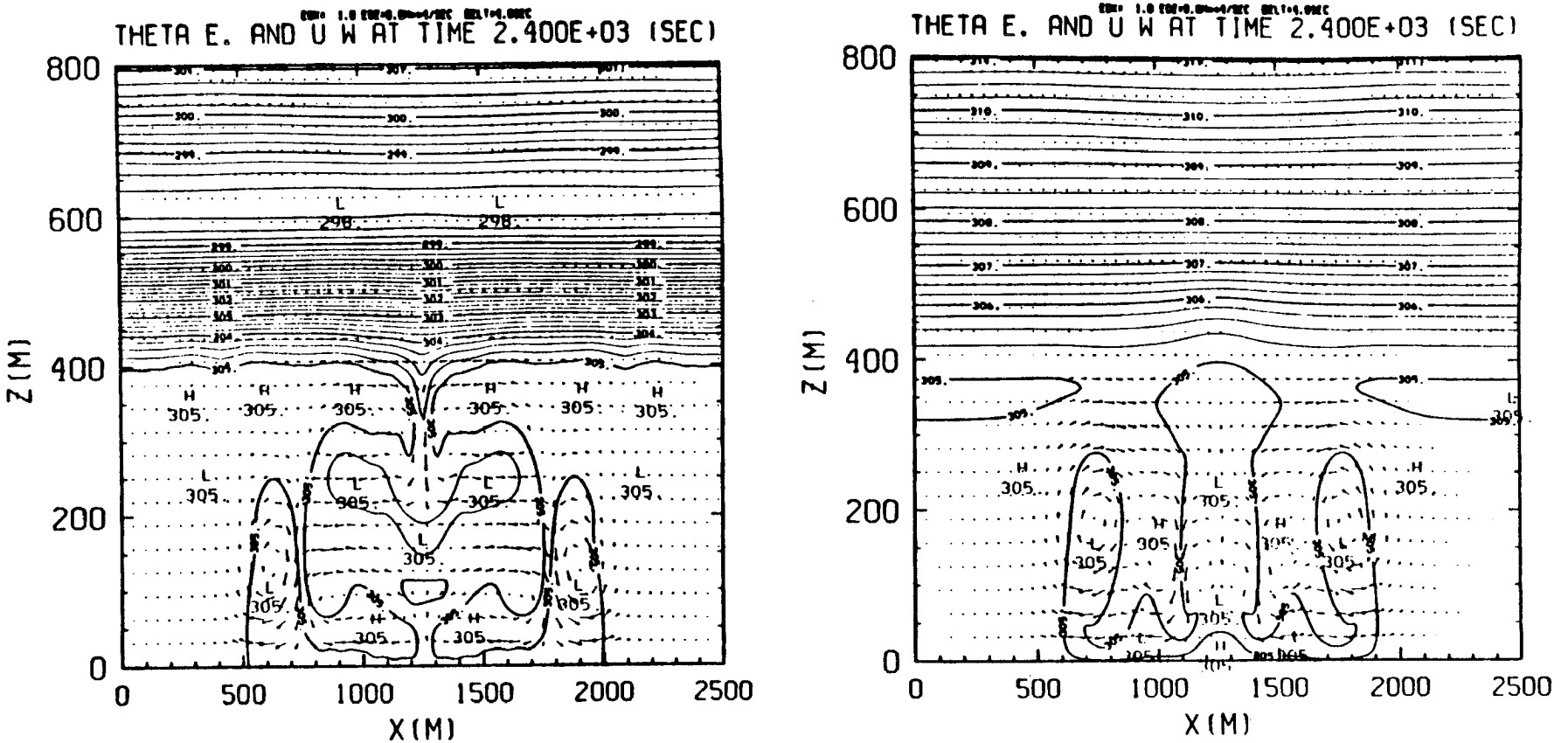

Figure 6.6. Same as figure 6.3 except at 40 minutes. The maximum velocity is 0.69 m s^{-1} for the U2 case and 0.67 m s^{-1} for the S case.

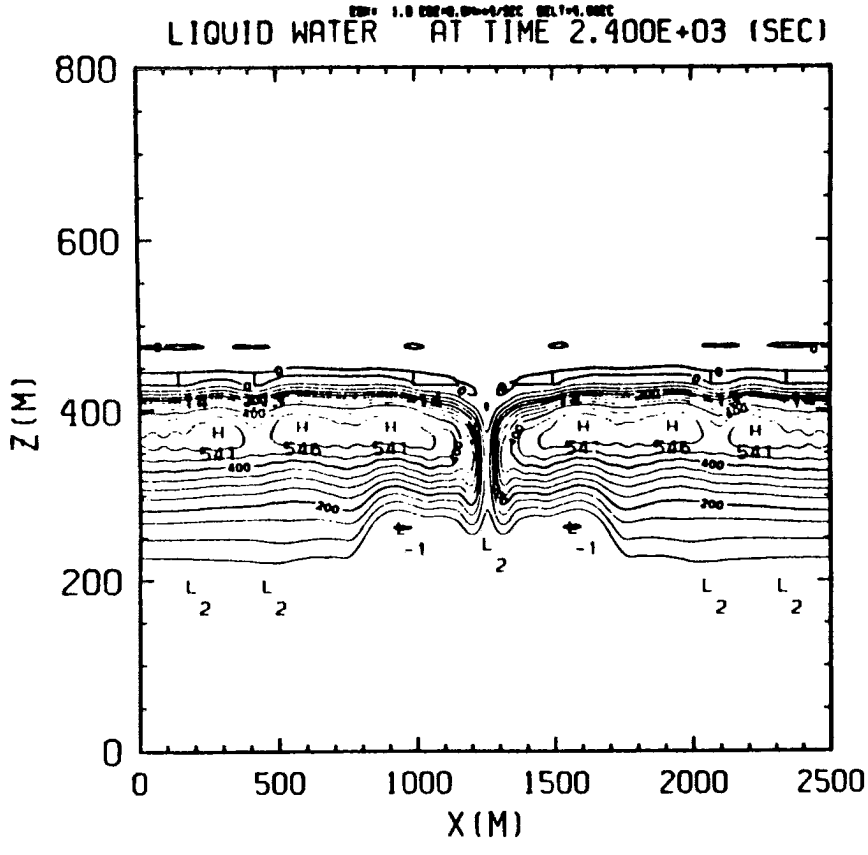

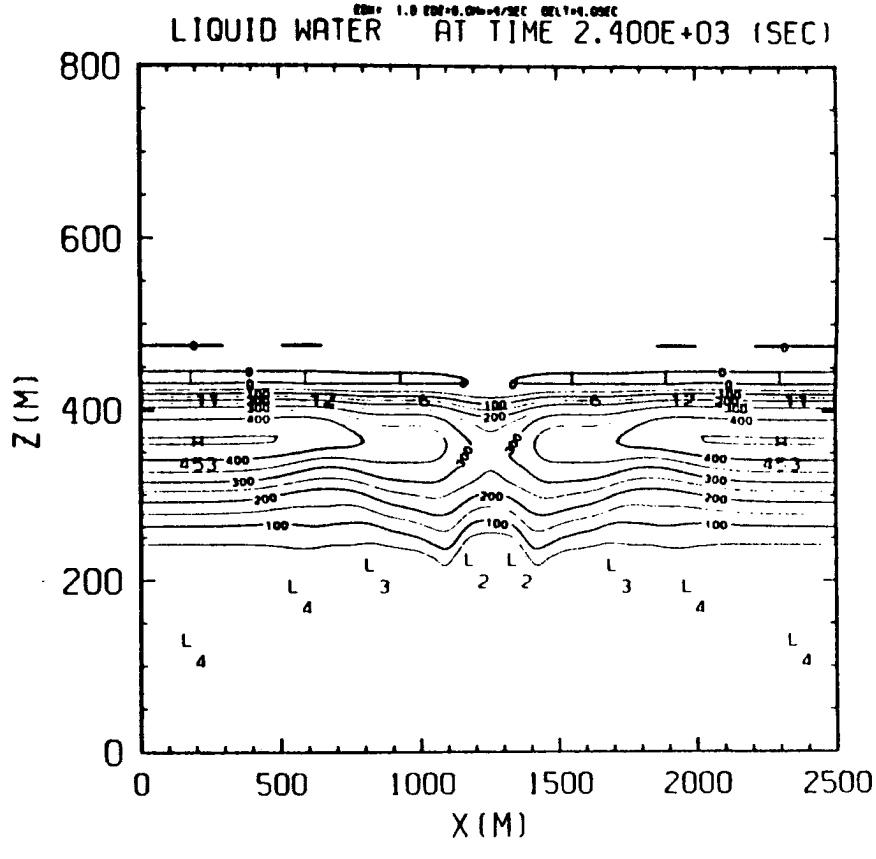

Figure 6.6. (Continued)

due to the decrease of entrainment. There are only subtle differences between the unstable U2 and stable S cases. In neither case do we see any sign of spontaneous rapid entrainment or cloud breakup.

In these initial value experiments, warm dry air is first brought down into the cloudy layer by the sinking cold bubbles. When the Θ jump is -7 K as in the U2 sounding, the mixed air parcel should be denser than the surrounding cloudy air from the classical entrainment instability argument. This negatively buoyant mixed parcel will then descend through the cloud layer and draw more dry air into the cloud. With this repeated process, there should be rapid entrainment and cloud breakup. Yet the disappearance of the cloud top hole from minute 10 to 20 for both the U2 and the S cases indicates that the mixed parcels become less and less negatively buoyant; thus they cannot penetrate freely into the cloud layer and draw more dry air from above. The cloud hole then disappears due to the decrease in entrainment. The fact that much dryer air (0.5 g kg^{-1} water vapor content) is involved in the U2 mixing process, yet the U2 results are so close to the S case, implies that there is not enough evaporative cooling in the U2 mixing process. Due to this insufficient evaporation, saturation of the entraining air is not guaranteed even in the negative Θ jump case. The mixed parcel as a result will not be colder than the surrounding environment and entrainment will decrease. This also explains why there are only subtle differences between the U2 and S cases. The lack of sufficient evaporation of the cloudy air when the dry parcel was introduced from above may be the key missing ingredient from the classical entrainment instability argument.

We have argued so far from the initial value problems that entrainment instability may not work as it was originally proposed. The key thing missing from that argument is the lack of enough evaporation to cool the mixed air parcel even when the Θ jump is -7 K. This insufficient evaporative cooling can probably be attributed to the typical low liquid water content of stratocumulus. In the cloud-topped marine boundary layer, the radiative cooling, latent heat exchange, turbulence and large scale subsidence are all involved in the entrainment process. Moreover, the turbulence budget depends crucially on the diabatic forcing (radiative cooling and latent heat exchange). One might then wonder if entrainment instability can be realized in a finite time due to the negatively buoyant cloudy air which has

undergone little mixing with the inversion air. Namely, can entrainment instability slowly build up by the feedback mechanism of some slightly mixed negatively buoyant eddies to the boundary layer turbulence? We will show this is not the case from the radiatively forced moist experiments where the effects of diabatic forcings, turbulence and large scale mean conditions are all considered. We shall see no sign of stratocumulus breakup even with unstable initial profiles.

6.3 Radiatively forced experiments

To further study entrainment instability in the forced situation, the U1, U2 and S soundings are numerically integrated under the interactive radiative forcing (forcing A) in this section. The radiative cooling will always cover about the top 75 m of the cloud in one vertical column with its magnitude depending on the amount of the liquid water content locally. There will be no radiative cooling locally if cloud holes are formed; all the cooling is confined in cloudy air. The interactive radiation is inhomogeneous in both space and time. The horizontally averaged infrared cooling rate is about 3 K hr^{-1} throughout the period of model integration.

The U1 case is integrated for three hours with the flux computed in the last hour. Fig. 6.7 shows the velocity field as well as the cloud liquid water content at 80,100,120 and 140 minutes for the U1 case. The velocity field is presented on the left adjacent to the cloud liquid water field. From Fig. 6.7 in this forced U1 case, we first notice that there are no signs of cloud layer breakup at 140 minutes. Because the moist model was initialized with no background wind, the simulated stratocumulus clouds in Fig. 6.7 are purely buoyancy driven, not by heating from below but by longwave radiative cooling from above. The stratocumulus cells appear to be dome-shaped with sharp liquid water gradients on the side. These sharp liquid water gradients occur on a length scale of approximately 40 m and can extend all the way down to the cloud base. The regions of peak liquid water content (e.g. greater than 0.4 g kg^{-1}) usually appear to be dome shaped and cover the top 100 m of the convective cells. The maximum upward motion is in the center of the convective cell while the downward motion is near the side of the cell as can be seen in both the velocity and the cloud liquid water fields in Fig. 6.7. The downdraft regions do not necessarily have

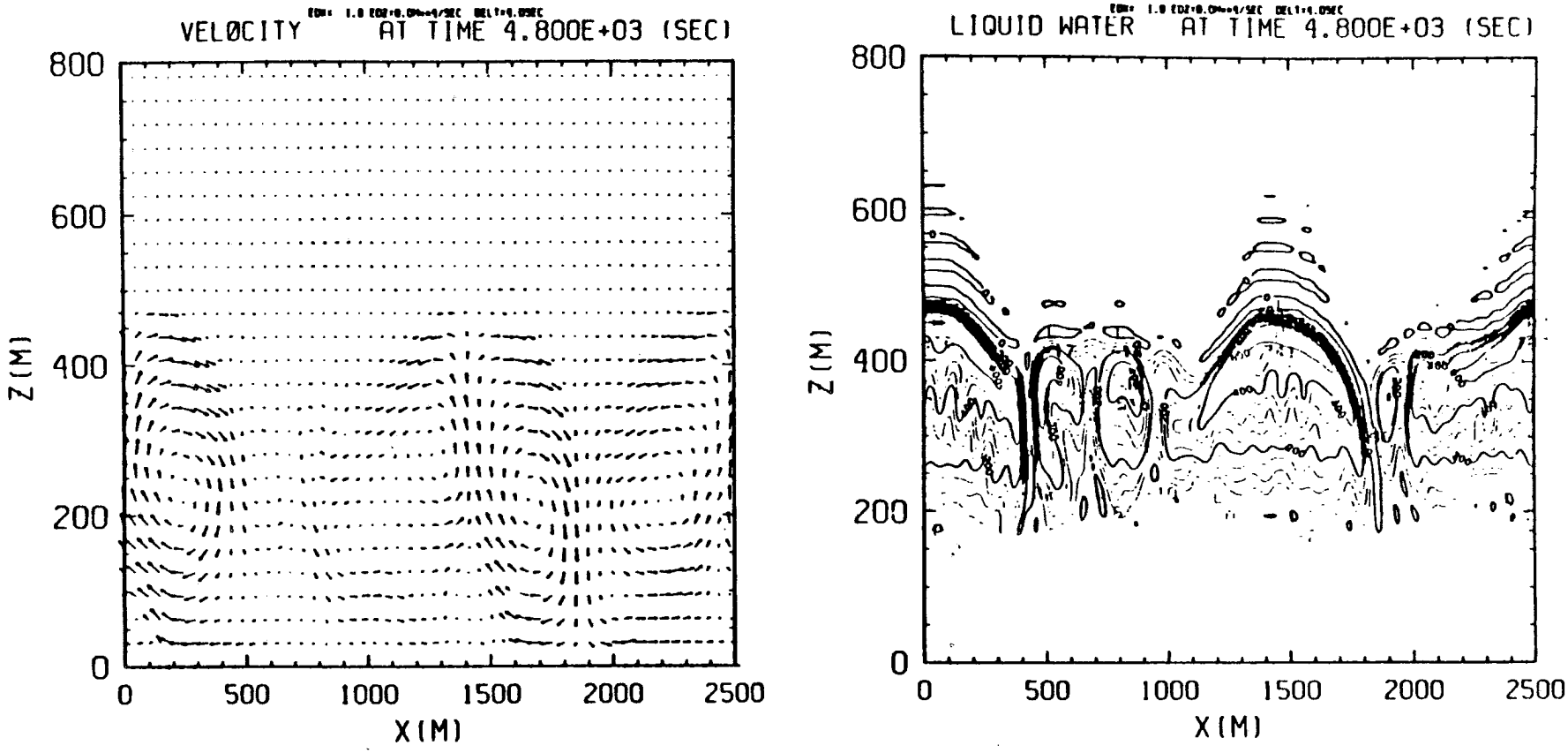

Figure 6.7. The velocity and the liquid water mixing ratio fields in physical domain for the U1 case in the interactive radiation experiment at time equal to 80, 100, 120 and 140 minutes. The velocity pictures are presented in the left adjacent to the liquid water mixing ratio pictures. The liquid water in unit g kg^{-1} is scaled by 10^3. The maximum velocities in the sequence of the pictures are 2.5m s^{-1}, ,2.7 m s^{-1}, 1.9 m s^{-1} and 2.4 m s^{-1} respectively.

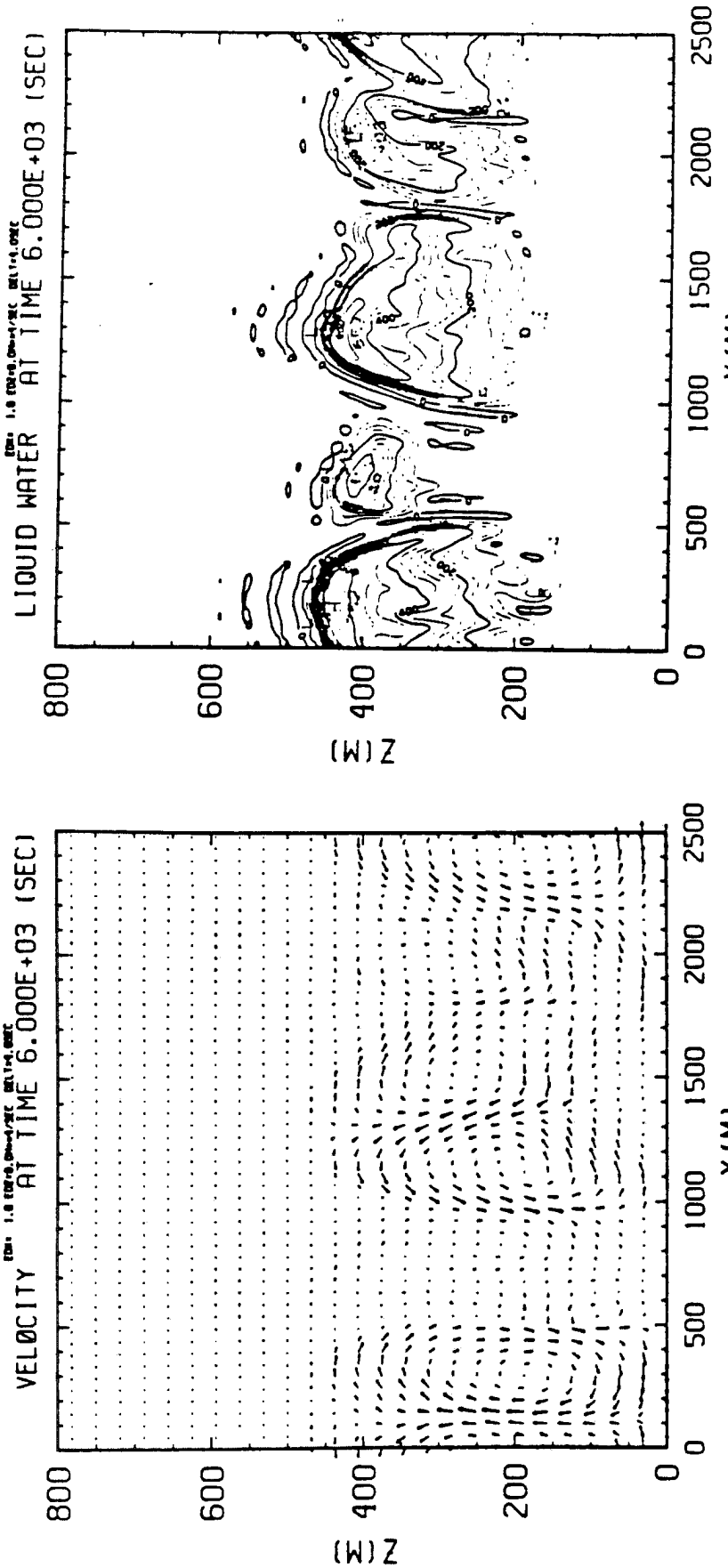

Figure 6.7. (Continued)

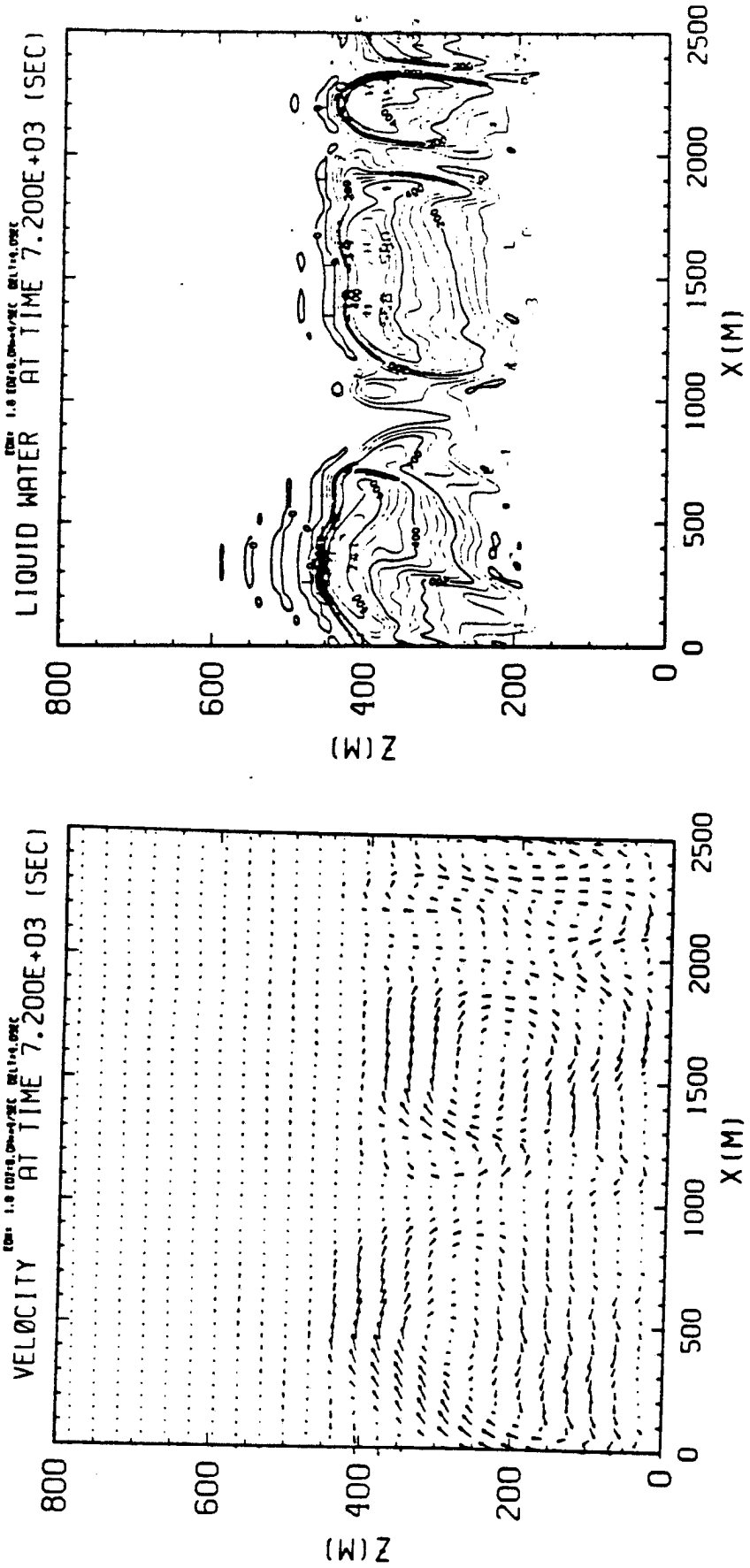

Figure 6.7. (Continued)

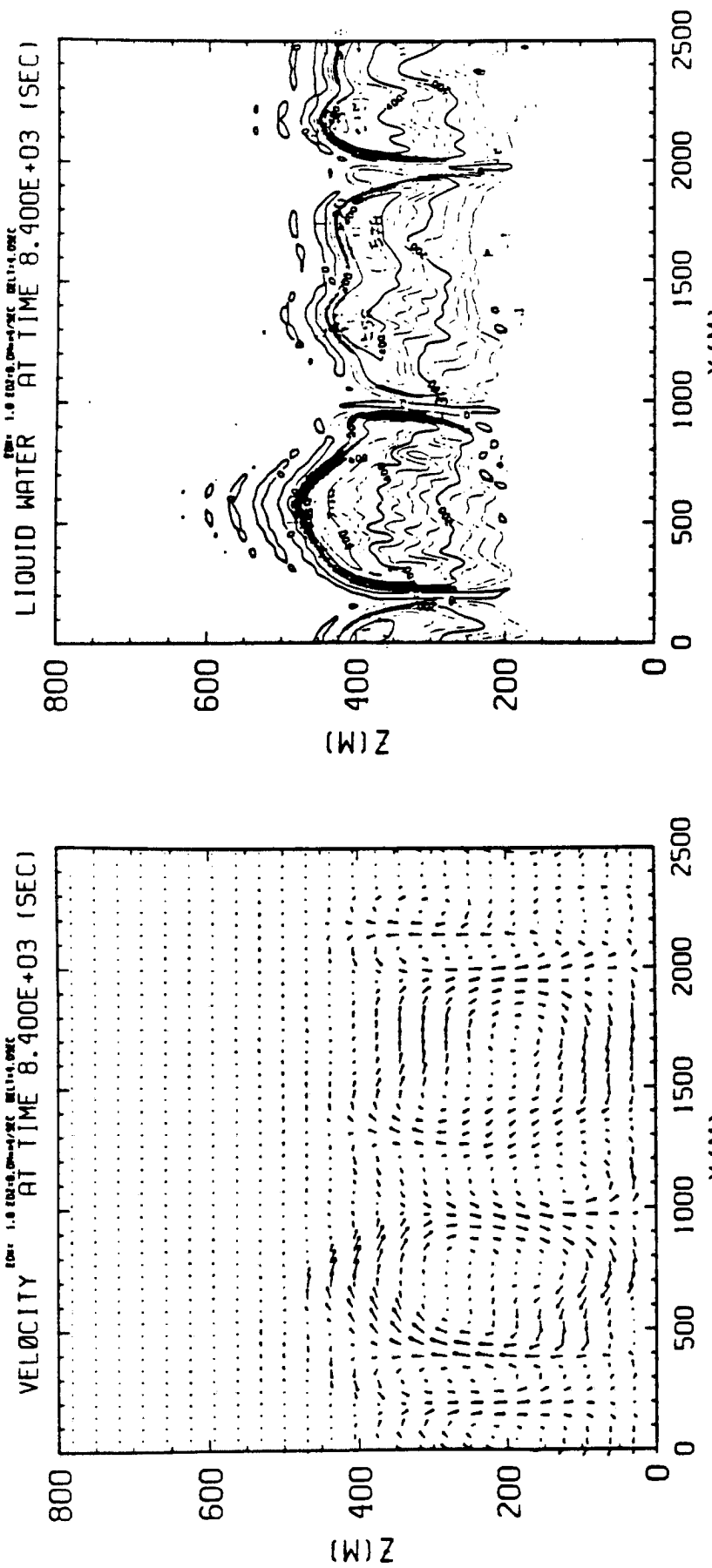

Figure 6.7. (Continued)

higher cloud bases (e.g. region near $x = 2000$ m at 80 minutes) as predicted by the simple mixed layer model. This indicates that the downdraft may not be always undergoing much mixing with the inversion air. There is only one cell of circulation in the vertical most of the time as shown in these velocity field pictures. It is these convective circulations which make the cloud-topped boundary layer well mixed. We do not observe any decoupled circulation in the vertical in the present study. The convective cell seen in Fig. 6.7 has a horizontal length scale of 800 m. Because the boundary layer has a depth of about 450 m, the aspect ratio of these cells is about 2.

Another interesting feature of these experiments is the life cycle of the convective cell near the horizontal position of 800 m. From 80 to 120 minutes model time, this cell is dying and forming a large cloud hole near $x = 800$ m. The cloud hole then disappears and the cloud becomes solid again in 20 minutes. We have seen phenomena like this many times in other model integrations. The appearance of cloud holes with the decay of convective cells appears to be a part of the natural variability of purely buoyancy driven convection. The cloud holes can disappear in a short time because of the formation of new convective cells; they appear to have nothing to do with entrainment instability.

Figs. 6.8 and 6.9 show velocity and cloud liquid water fields for the S and U2 cases at different times respectively. The motion fields are single-celled in the vertical with an aspect ratio of 2. The stratocumulus cells are again dome shaped with peak liquid water gradients on the side. The maximum upward motions are in the center of these convective cells. It seems that all physical features of the cloud-topped boundary layer in Figs. 6.8 and 6.9 agree quite well with Fig. 6.7. Also shown in Fig. 6.8 is the disappearance of the cloud hole in 20 minutes near $x = 250$ m. This is just another example of the natural variability of the convective cells.

Fig. 6.10 presents the profiles of the Θ, θ, ϑ, r, q and l fluxes from all three experiments. These fluxes represent an average state of the boundary layer in equilibrium with the mean large scale conditions. These fluxes are presented in the energy unit W m kg^{-1}, which is the same as the W m^{-2} unit if the air density is taken to be 1 kg m^{-3}. As in Fig. 6.10 the profiles of the flux are very similar for all cases. The U2 case has a larger magnitude for the total water and liquid water flux. This might be due to the fact that much dryer air was

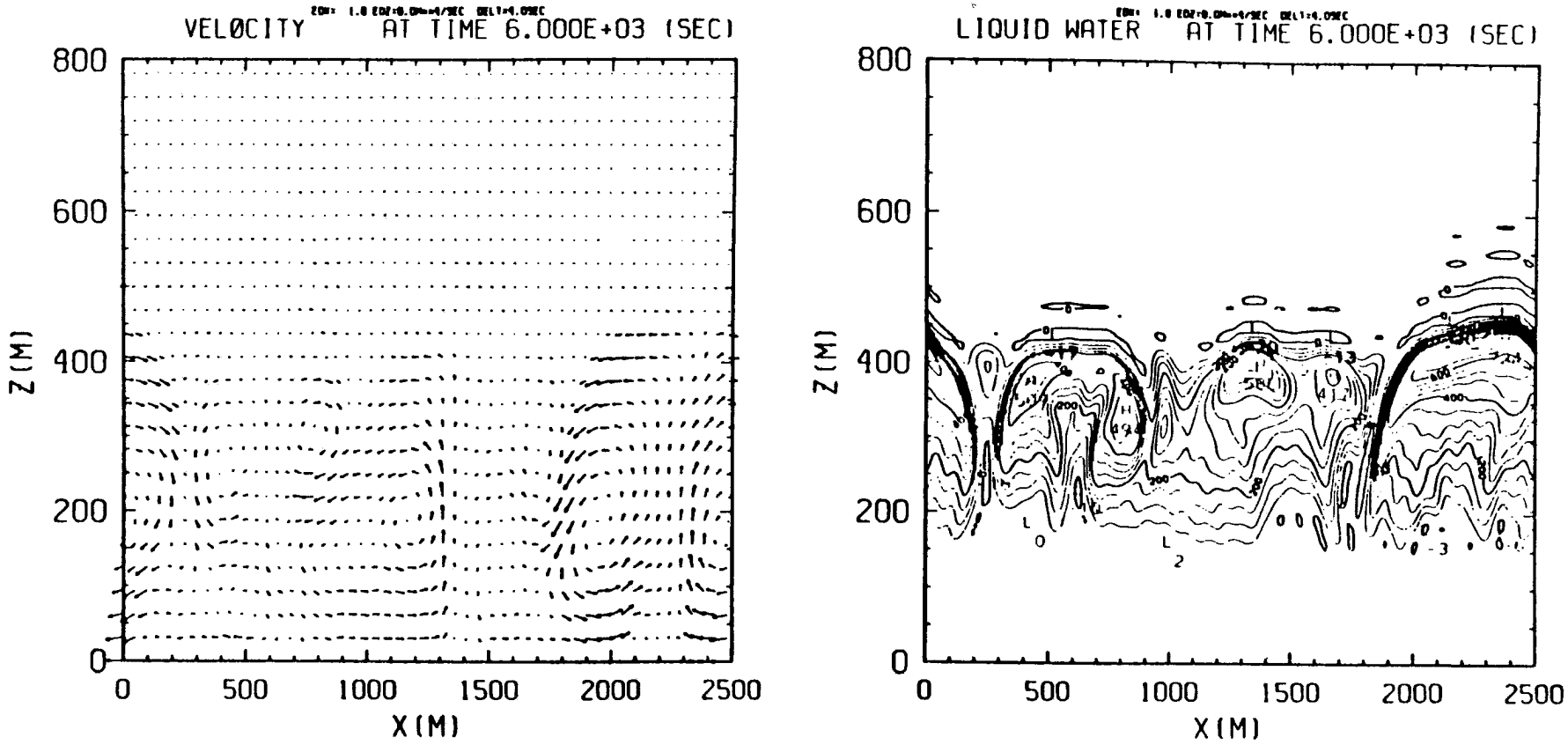

Figure 6.8. Same as figure 13 except for the S case at 100 and 120 minutes. The maximum velocities in the sequence of pictures are 2.5 m s^{-1} and 2.4 m s^{-1} respectively.

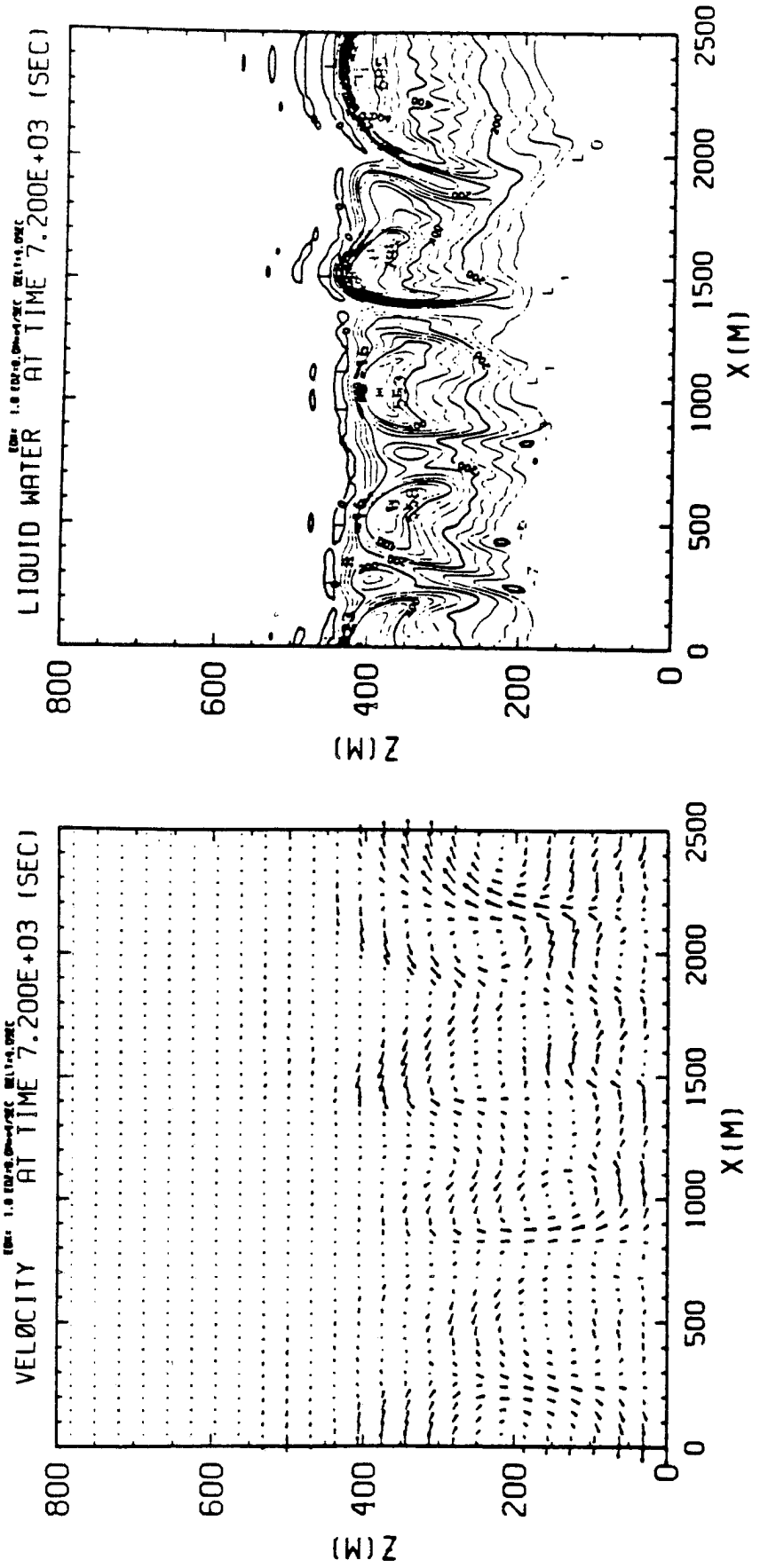

Figure 6.8. (Continued)

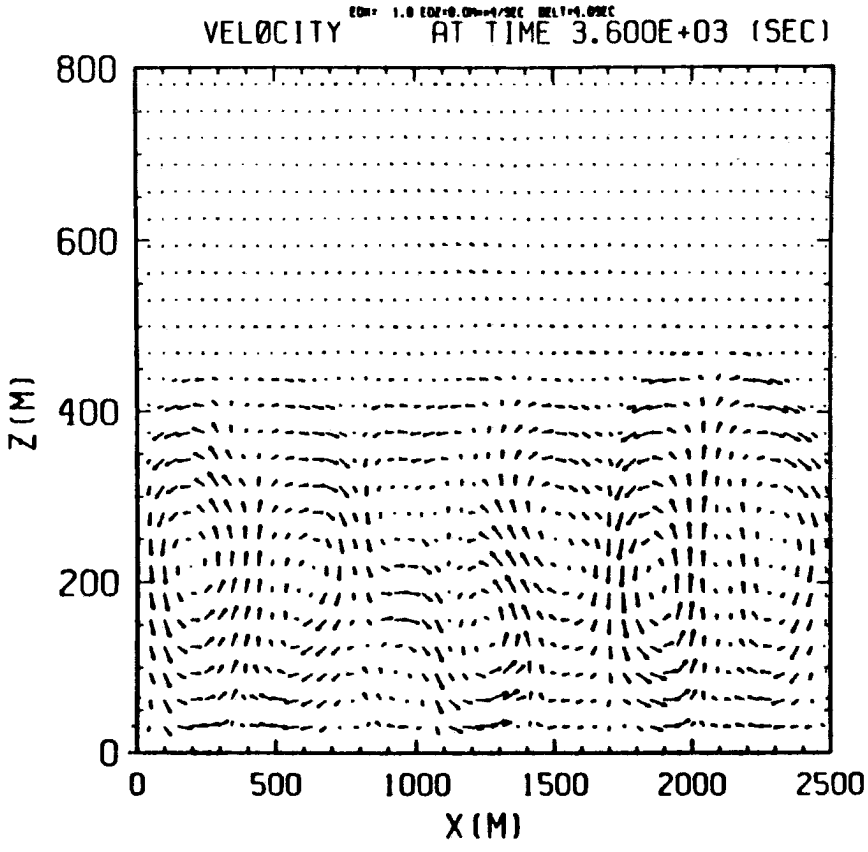

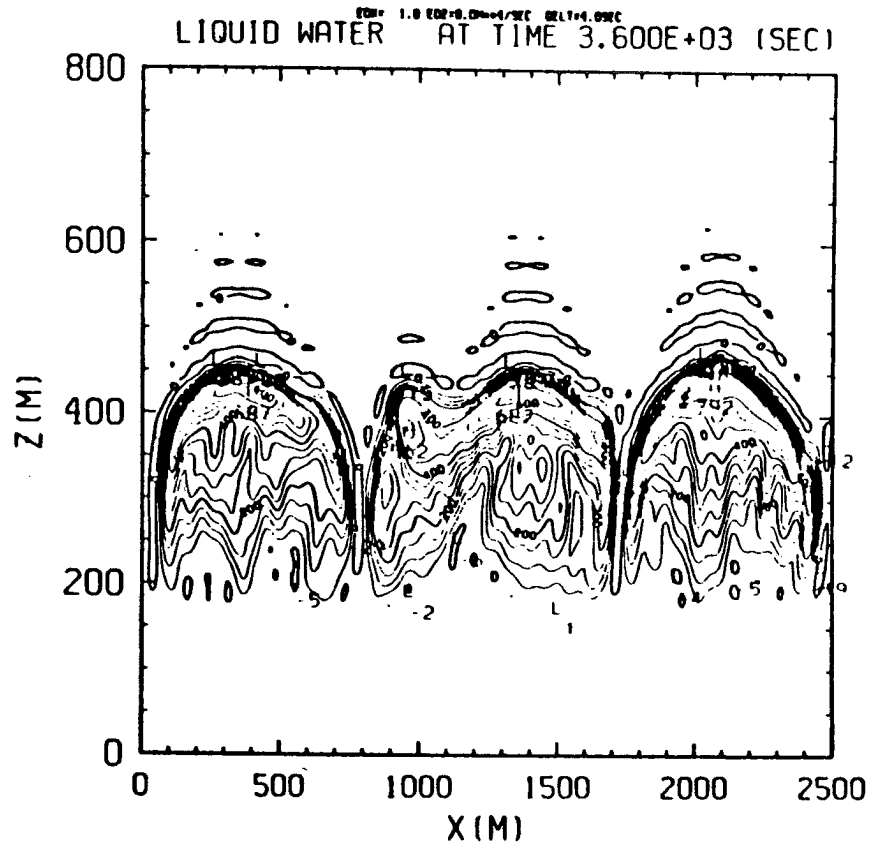

Figure 6.9. Same as figure 13 except for the U2 case at 60 and 120 minutes. The maximum velocities in the sequence of pictures are 0.21 m s^{-1} and 3.6 m s^{-1} respectively.

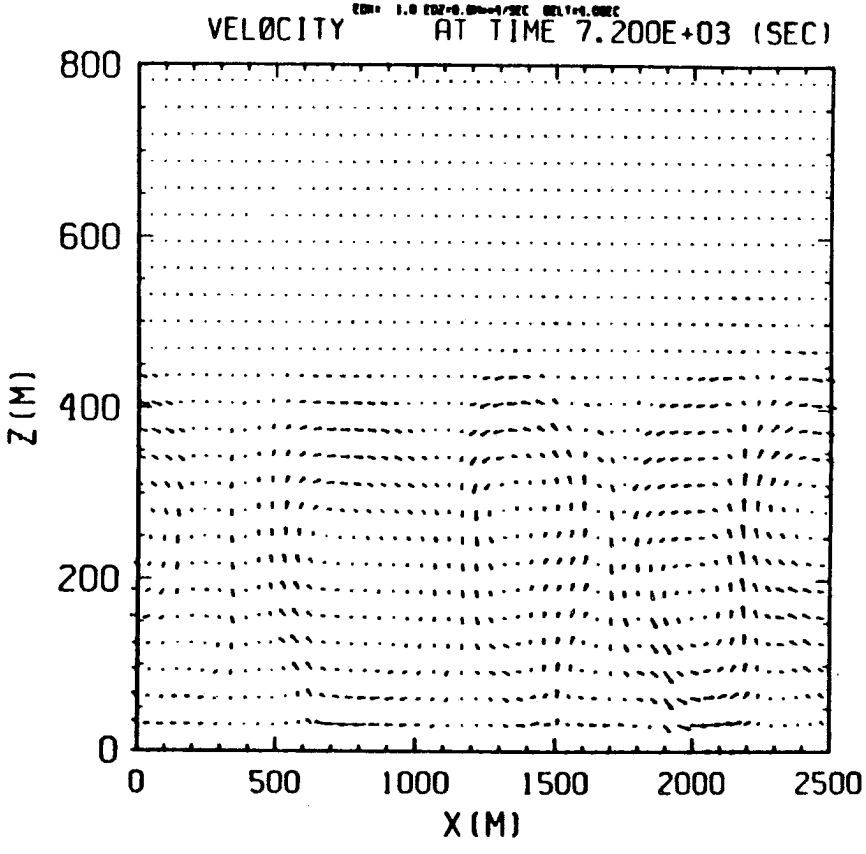

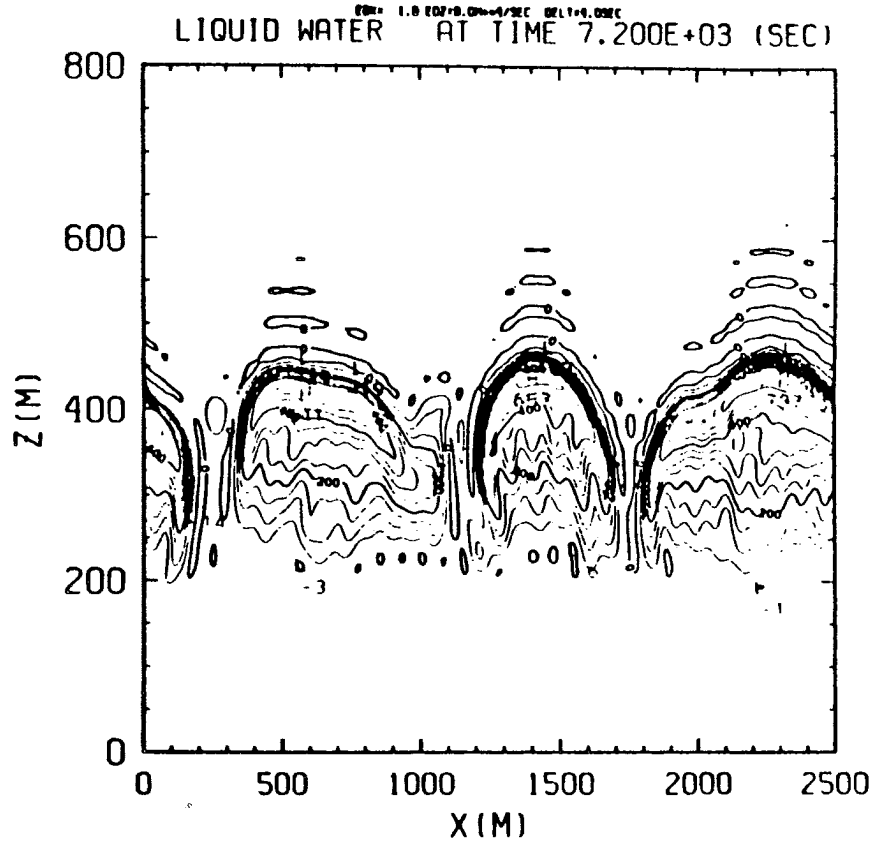

Figure 6.9. (Continued)

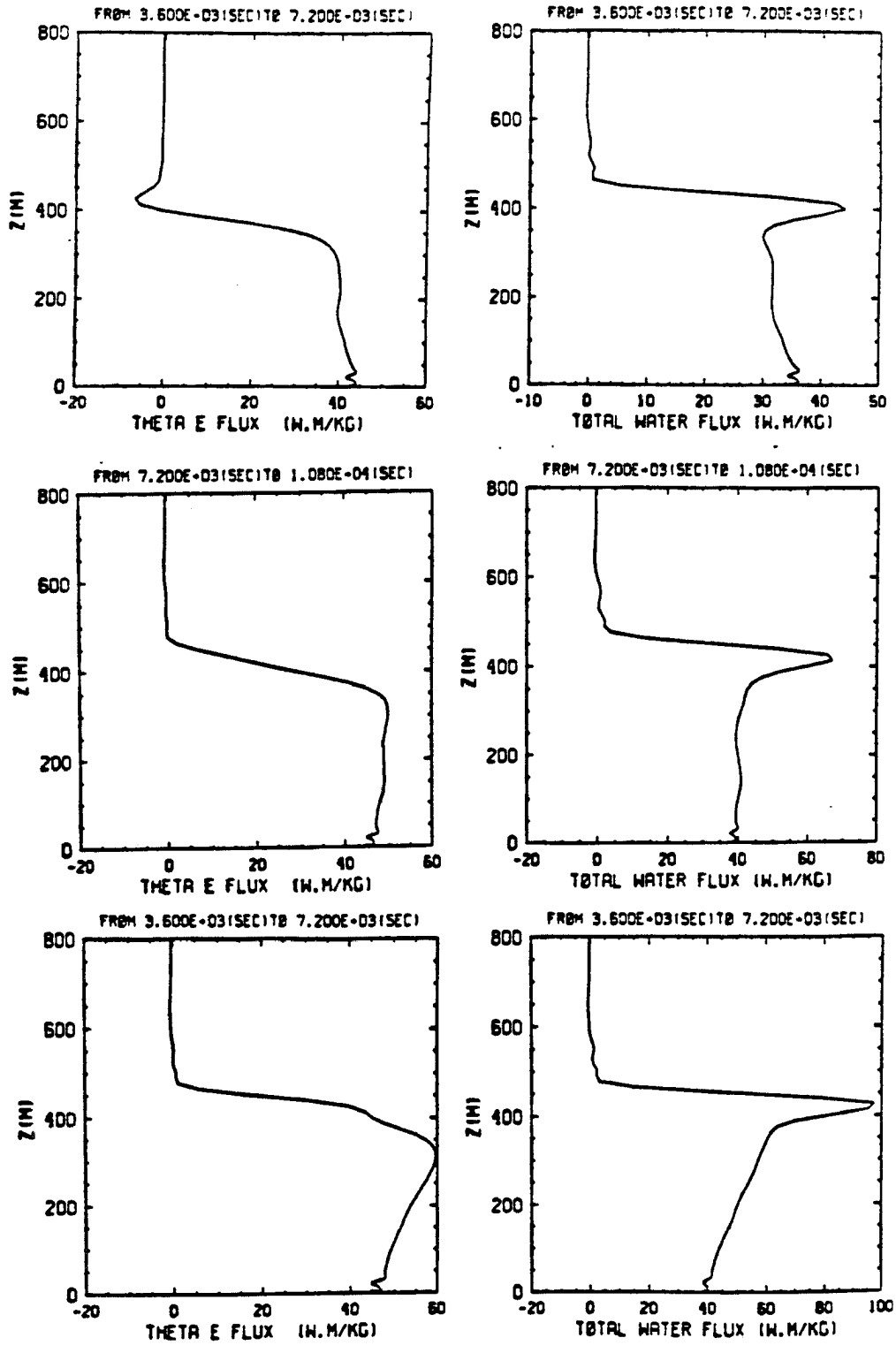

Figure 6.10. The Θ, r, θ, l, ϑ and q flux profiles for S(top), U1(middle) and U2(bottom) cases in the interaction radiation experiment. All the flux profiles are computed in a one hour period.

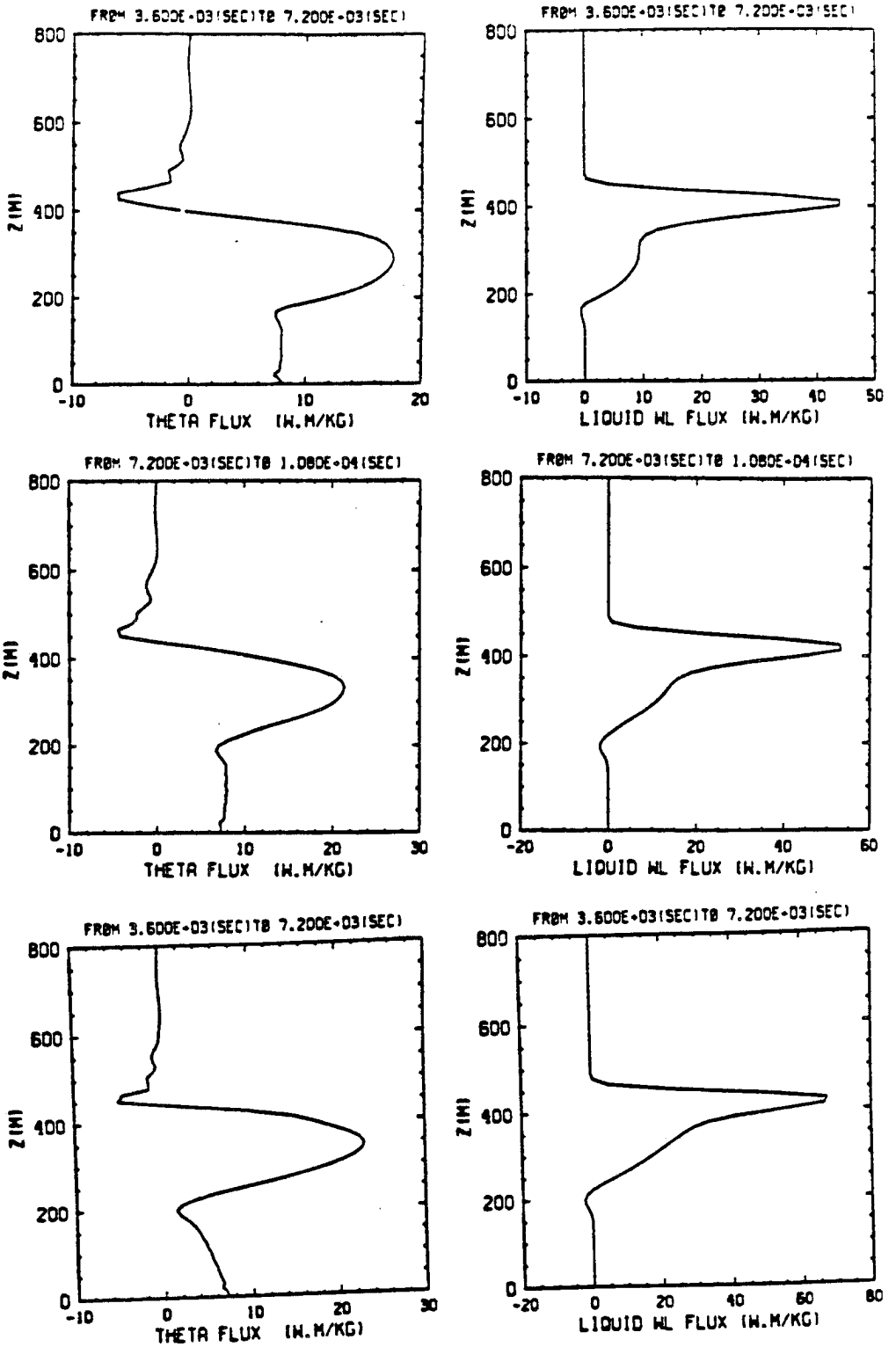

Figure 6.10. (Continued)

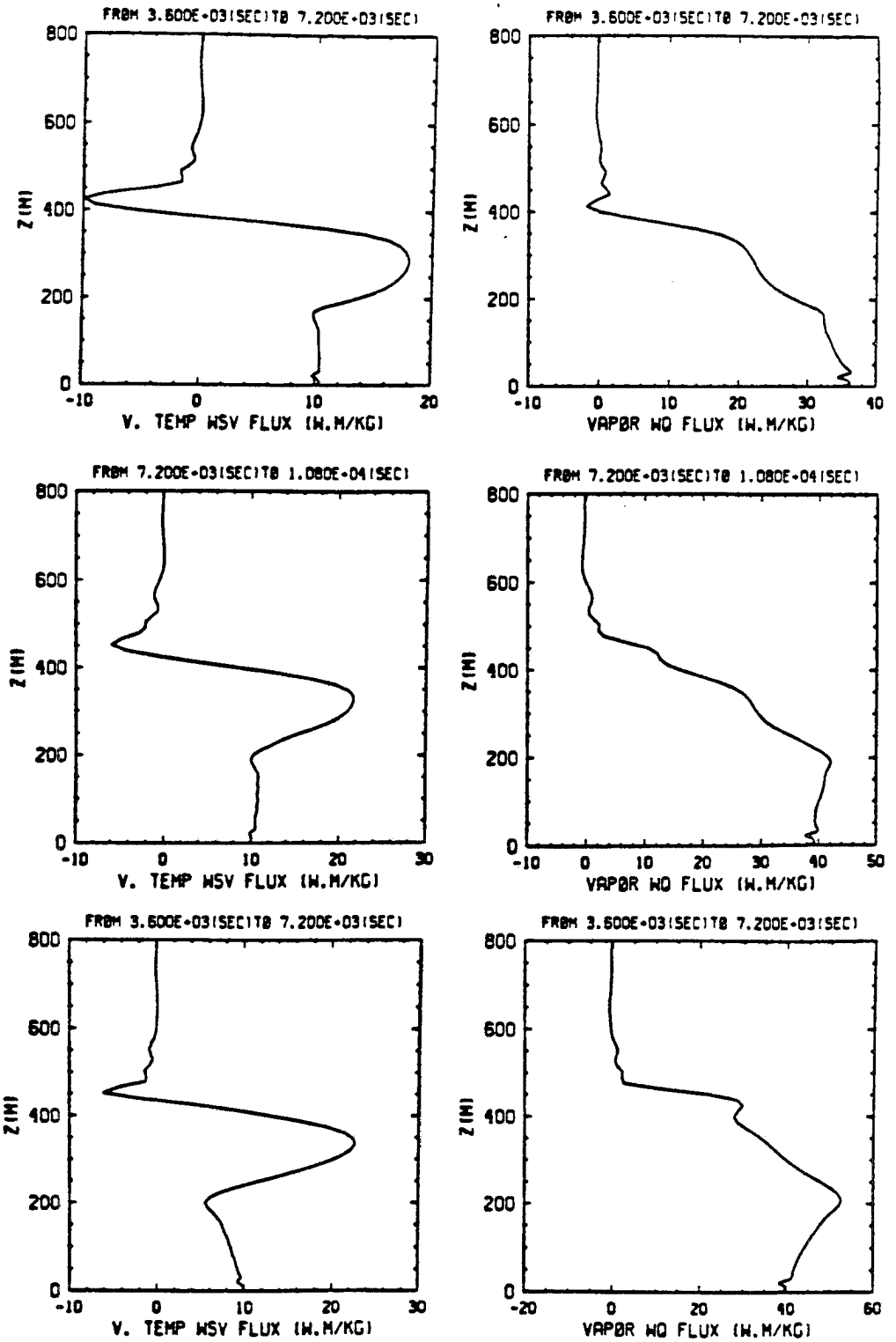

Figure 6.10. (Continued)

placed above the boundary layer in the U2 case, so that higher values of total water and liquid water flux are required to maintain the cloud layer. By the same reasoning the S case has the smallest total and liquid water flux. The negative values of the buoyancy flux (ϑ flux) and the heat flux (θ flux) right above the cloud top is caused by the overshooting of convective cells. The negative Θ flux value for the S case is also due to these overshooting convective cells. The U1 and U2 sounding have lower Θ values above the cloud top, so that there is no negative Θ flux by these overshootings. The much dryer air aloft probably has something to do with the smaller negative ϑ and θ flux above cloud top in the U1 and U2 case. The ϑ and θ fluxes from all cases are positive in both the subcloud layer and the cloud layer. The latent heat release inside the cloud contributes to larger ϑ and θ fluxes in the cloud region. We note that the positive subcloud layer fluxes differ considerably from classical mixed layer solutions.

Fig. 6.10 shows that both the U1 and U2 cases in the forced situation have very similar flux profiles to the S case. These flux profiles represent a quasi-steady state of the boundary layer. Thus we might argue that cases U1, U2 and S are in the same equilibrium state. If we did not expect the stratocumulus to break up in the S case, then we have no reason to expect the cloud breakup in the negative Θ jump cases (U1 and U2) since they are in the same equilibrium. Being in the same equilibrium also suggests that entrainment instability cannot be a slow time scale process depending on the feedback of some slightly evaporated cloud eddies (negatively buoyant) to the turbulence dynamics. Unless there are unlikely multiple equilibria on the time scale of hours for these stratocumulus, we might conclude that the cloud layer will not break up by the classical entrainment instability mechanism.

6.4 A case with strong entrainment

Cloud top entrainment is driven by turbulence, evaporation and cloud top radiative cooling. We will show in this section that the stratocumulus clouds remain solid even when there are some indications of strong entrainment. The fixed radiative forcing (forcing D) is used in this section. The prescribed cooling region in the model is between 400 m and 450 m in the vertical (in the initial cloud top region) with a peak cooling rate of about 11 K hr^{-1}. This non-interactive radiation is homogeneous in both space and time. Note that parts of

this non-interactive cooling will inevitably be applied to the clear air region between cloud domes during the time integration. The U2 case under fixed radiative forcing gives very similar results as the U1 case, thus only the U1 and S case will be discussed in detail. The Θ fields at the initial and final time of the model integrations for the U1 and the S cases are presented in Fig. 6.11. The U1 case is shown on the left adjacent to the S case. The 304 K and 306 K isotherms originally were located at 475 m height (in the capping inversion) for the U1 and S cases respectively. After two hours of model integration, the 304 K isotherm has been distorted and penetrates well into the boundary layer for the U1 case. The 306 K isotherm in the S case still stays above the cloud top except that it has been modified by the internal gravity waves. Since the same infrared radiative cooling is applied to each case, the distortion and the penetration into the mixed layer of the 304 K isotherm in the U1 case must be caused by the entrainment process. Fig. 6.12 shows the profiles of the horizontally averaged Θ field at the initial (dashed lines) and the end (solid lines) of the model integrations with the Θ profile of the U1 case lying on top of the Θ profile for case S. The S case (bottom of Fig. 6.12) still maintains a somewhat well-mixed boundary layer at the end of the model integration. The Θ field in case S is slightly lower than the 305 K initial condition due to the radiative cooling. On the other hand, the boundary layer is less well mixed in the U1 case and has a lower Θ value as compared with the S case after two hours of integration. This indicates lower Θ air above the cloud top has been brought down. The boundary layer is less well mixed as a result of this entrainment. The stronger entrainment appearing in the present U1 case probably is due to some of the larger non-interactive radiative cooling being applied to the clear regions between cloud cells.

Fig. 6.13 presents the velocity and cloud liquid water content fields at the end of the model integration. The U1 case is presented on the left adjacent to the S case. The convective cells have an aspect ratio of 2 as can be clearly seen from this figure. The clouds are nearly solid in both the U1 and S cases at the end of the model integration. There is no sign of cloud breakup in either case. The simulated stratocumulus clouds from the present non-interactive radiation forcing cases are very close to the ones in the interactive radiation cases (Figs. 6.7, 6.8 and 6.9), with the same dome shaped cloud cells and peak liquid water with sharp liquid water gradients on the side. When the entrained dry air

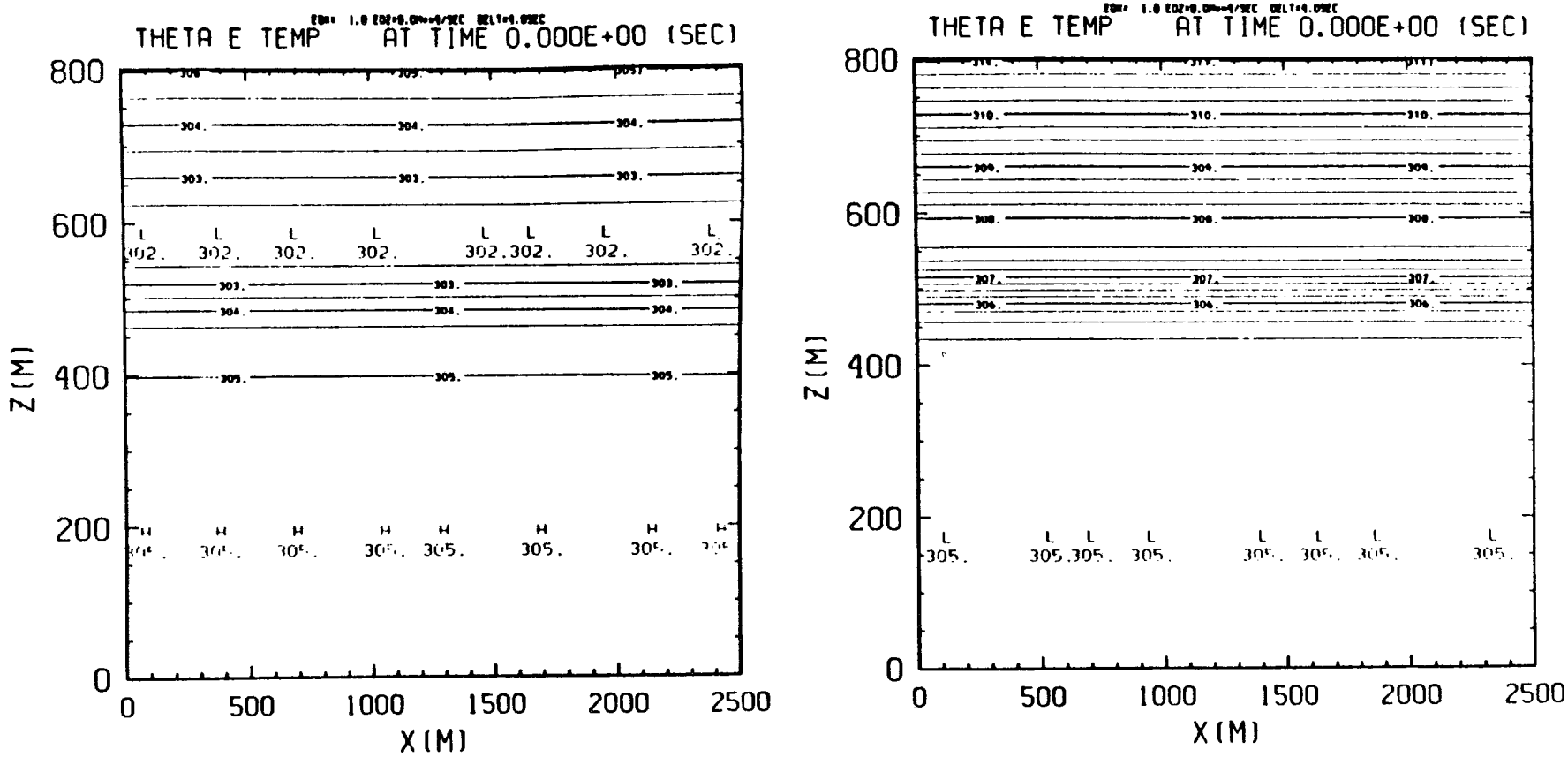

Figure 6.11. The initial (upper picture) and final (lower pictures) Θ temperature in the physical domain for the U1 and S cases in the fixed radiation experiment with the U1 case presented in the left adjacent to the S case.

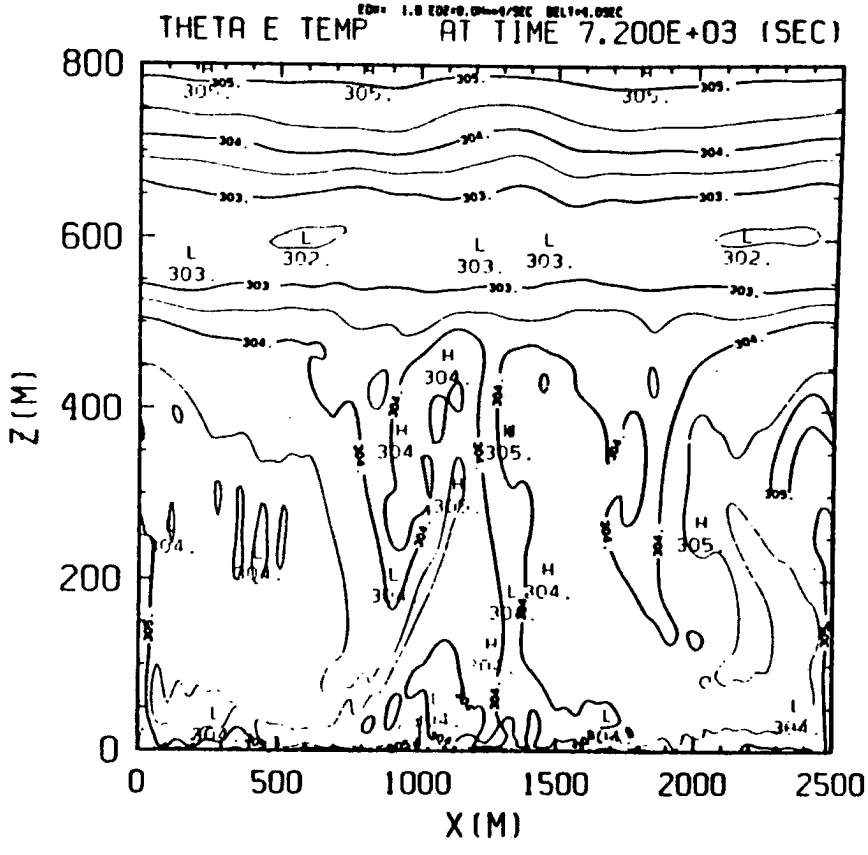

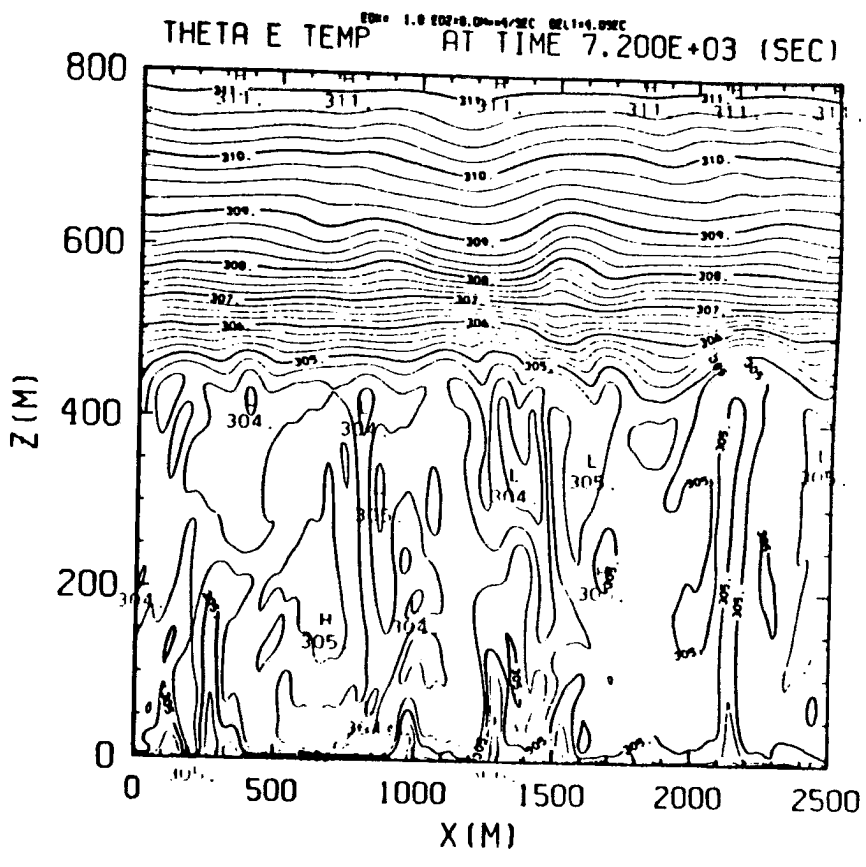

Figure 6.11. (Continued)

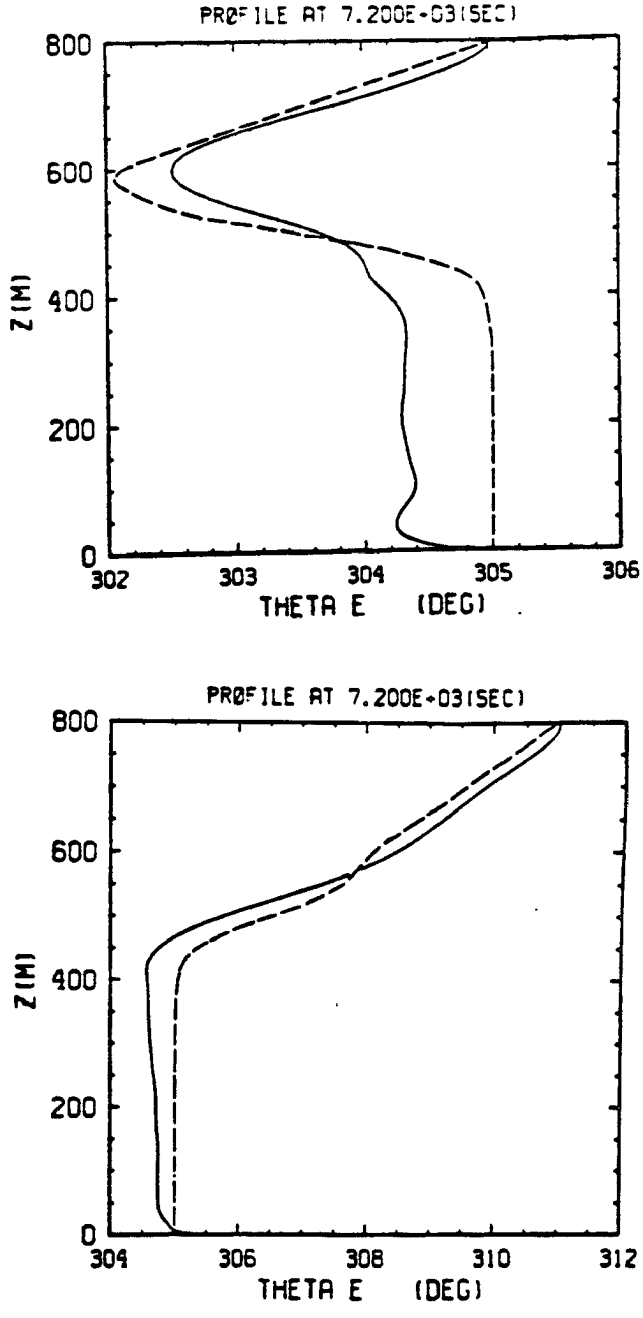

Figure 6.12. The horizontally averaged Θ temperature for the U1 and S cases in the fixed radiation experiment at the end of the model integration (120 minutes) with the U1 case shown on top of the S case. The dashed lines are the initial profiles for each case.

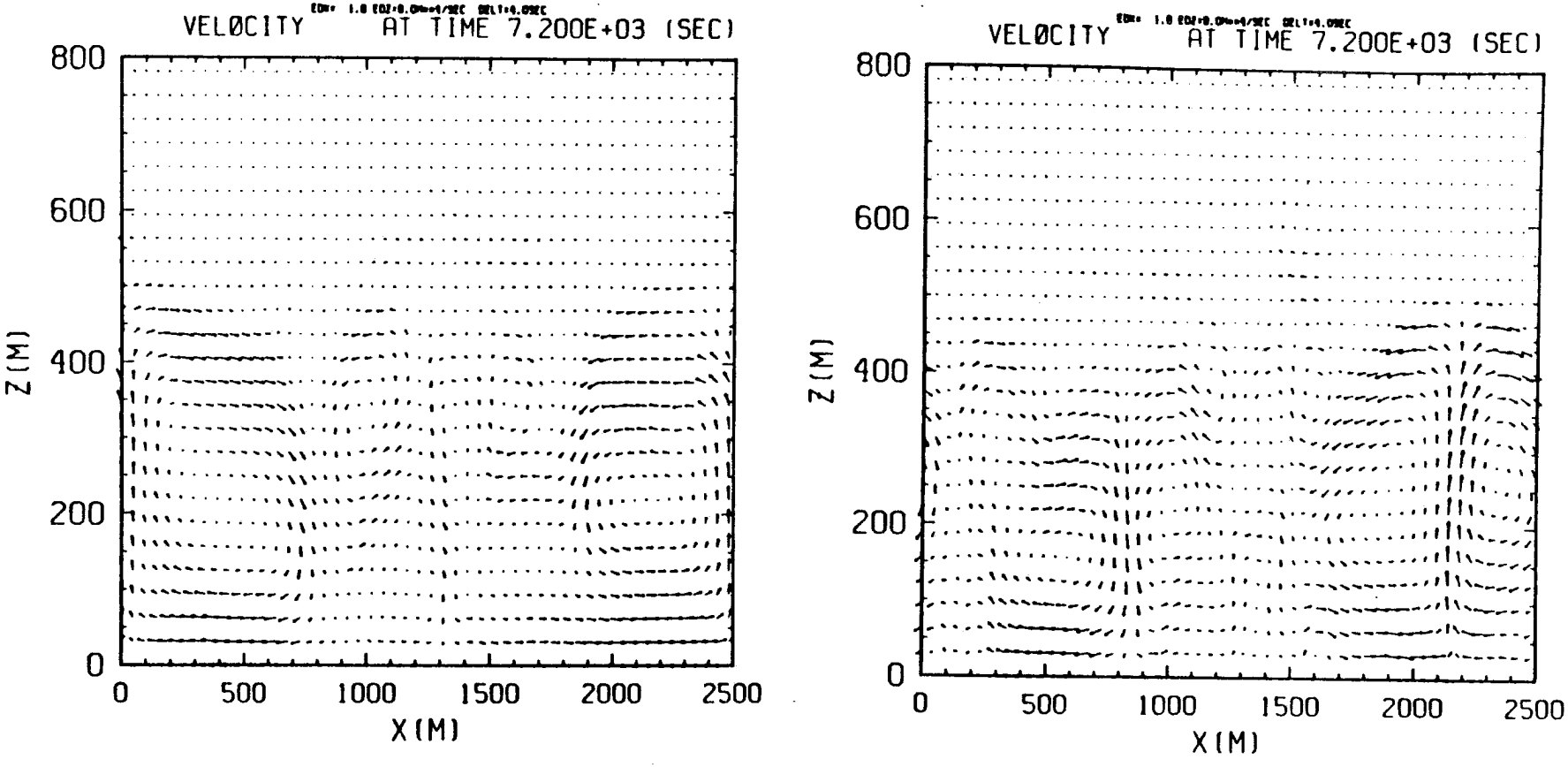

Figure 6.13. The velocity and liquid water mixing ratio in physical domain at 120 minutes for the U1 and S cases in the fixed radiation experiment. The liquid water mixing ratio in unit g kg^{-1} is scaled by 10^3. The maximum velocity is 3.8 m s^{-1} for the U1 case and 3.1 m s^{-1} for the S case.

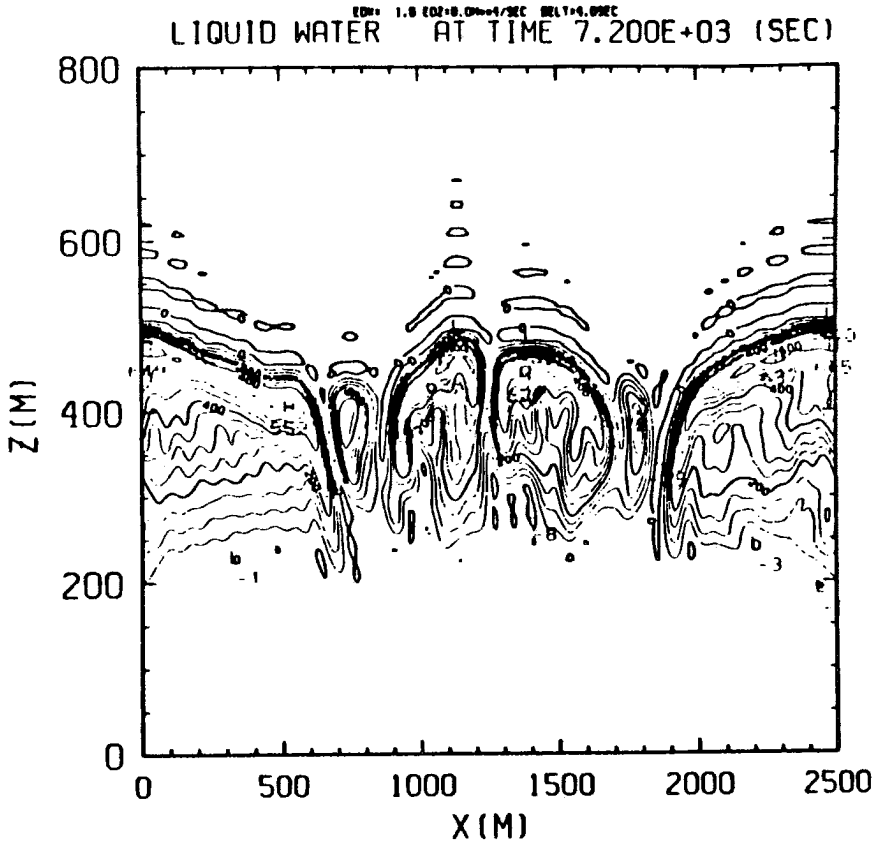

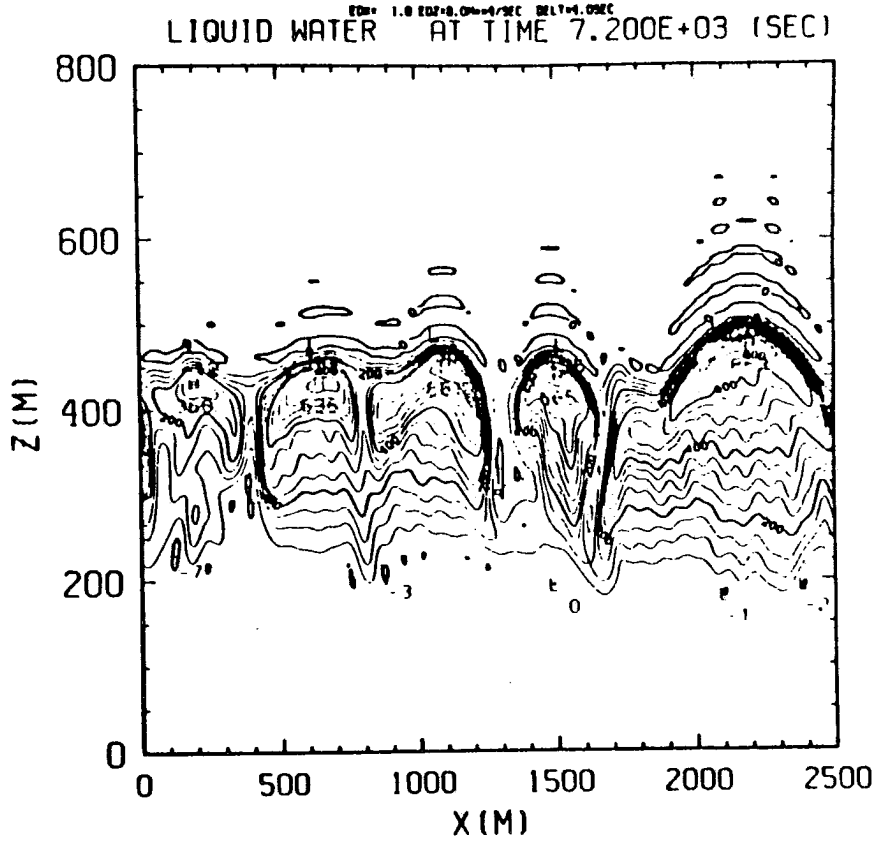

Figure 6.13. (Continued)

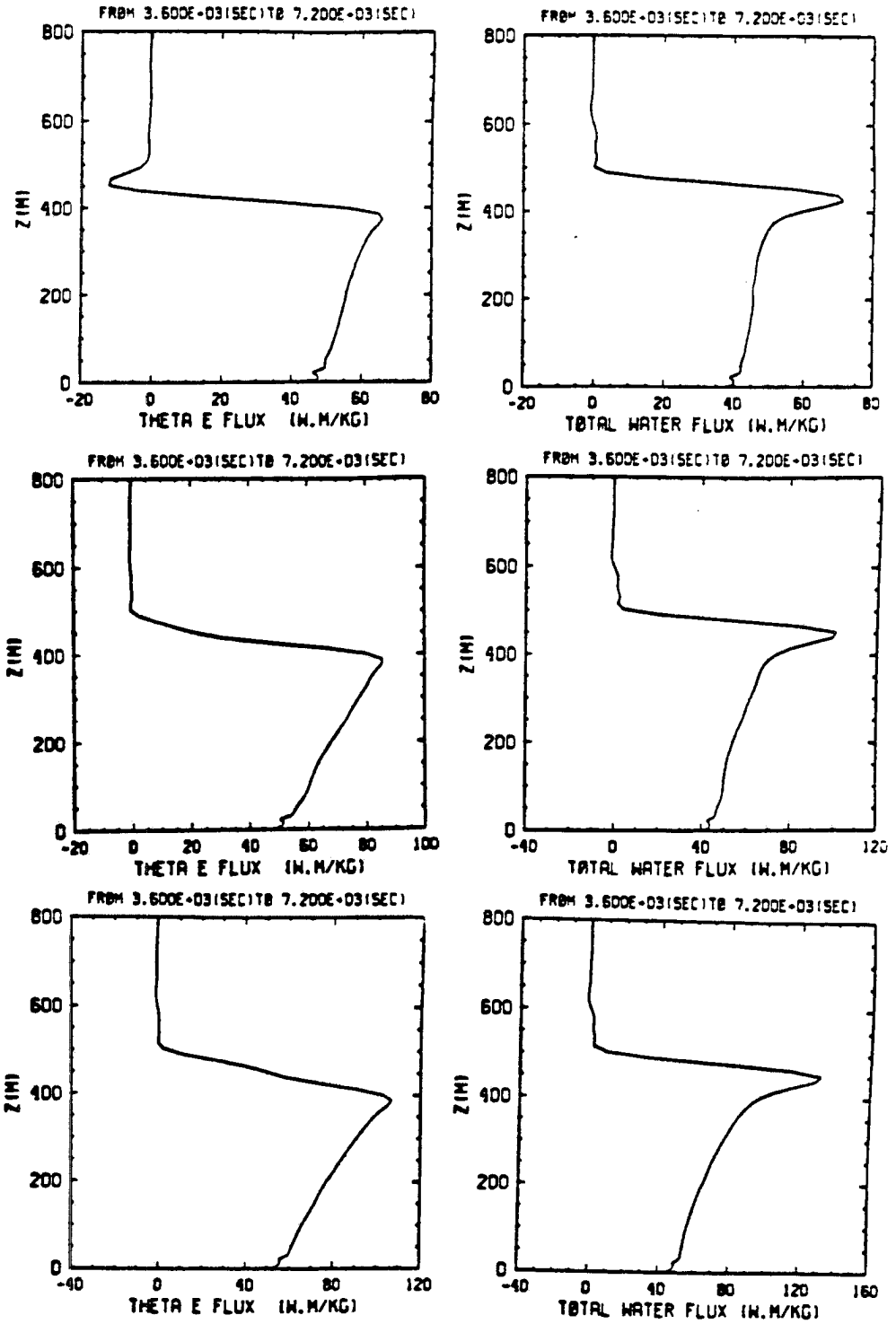

Figure 6.14. Same as figure 16 except for the fixed radiation experiment.

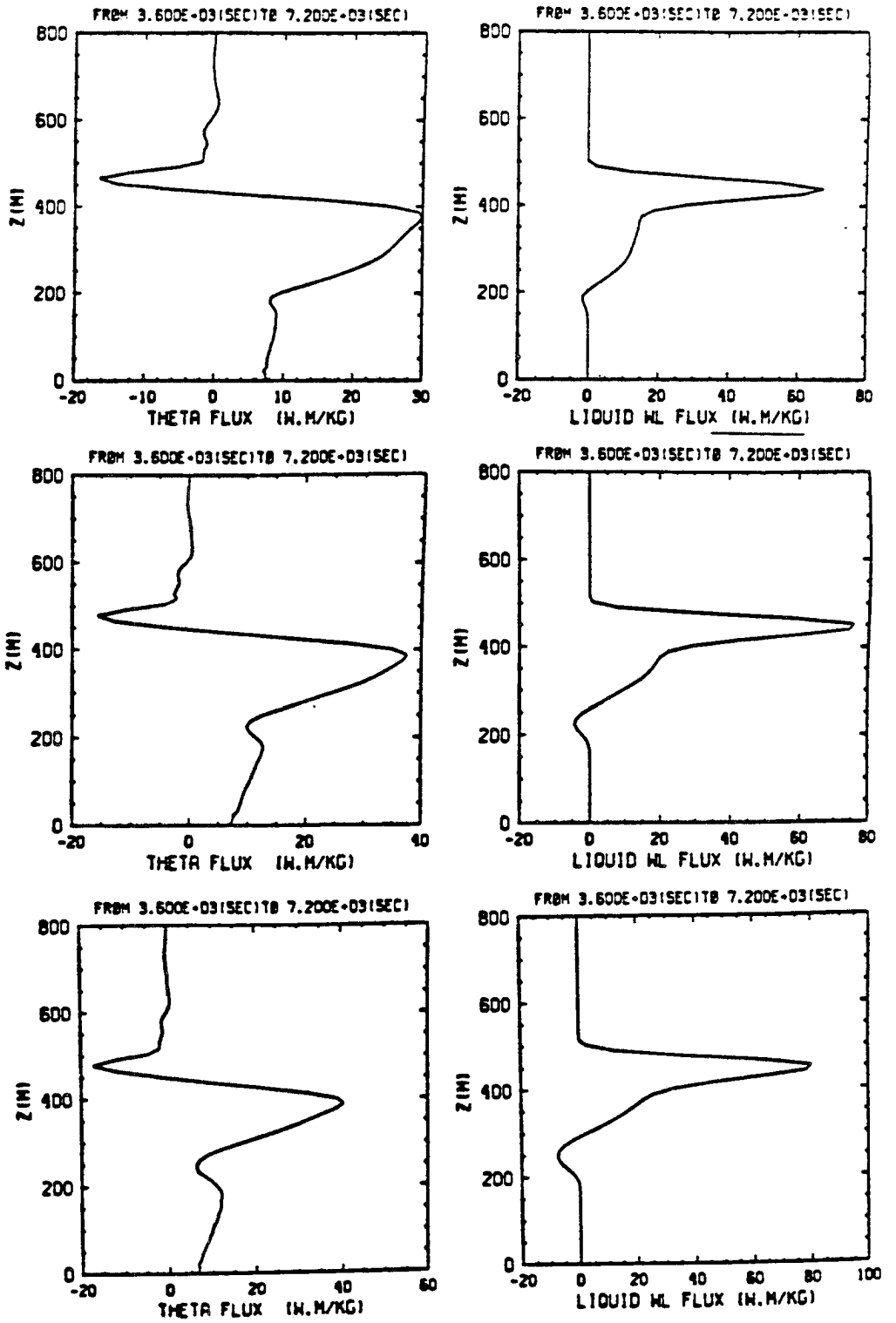

Figure 6.14. (Continued)

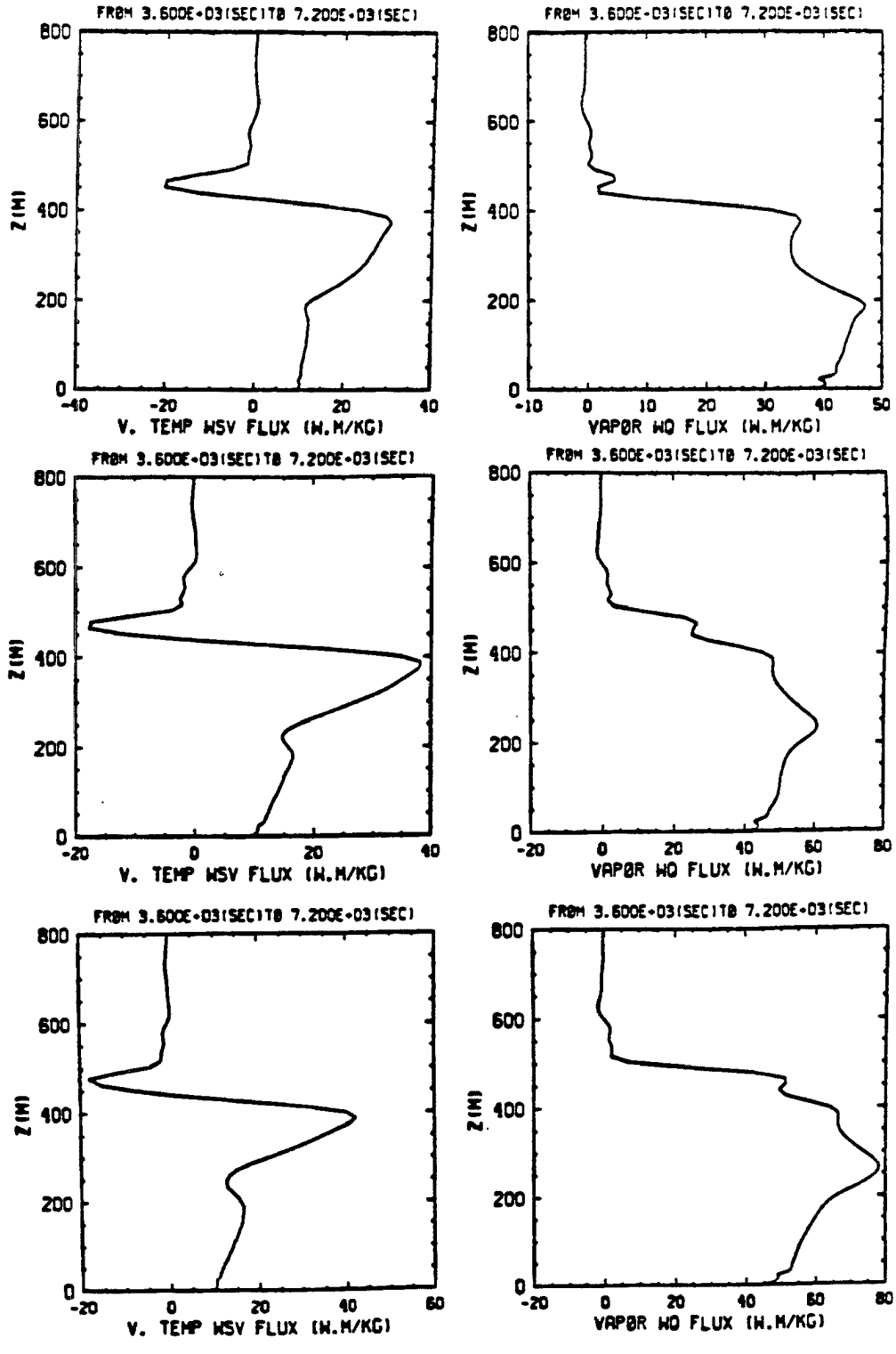

Figure 6.14. (Continued)

is carried down to the ocean surface by the convective circulations, there should be more evaporation occurring. The evaporated moisture from the ocean surface is then transported upward by the same buoyancy driven convective cells into the cloud layer against the drying effect caused by entrainment. This probably is the reason for the existence of the solid cloud under strong entrainment in this U1 case. The infrared radiation is important in two ways for the present case. It can generate entrainment and at the same time create buoyant circulations which carry water vapor upward from the ocean surface. The flux profiles for S, U1 and U2 under non-interactive radiation forcing are presented in Fig. 6.14. Again the largest liquid water and total water flux is in the U2 case while the smallest is in the S case. The flux profiles for the U1 and U2 cases are similar to the S case as can be seen in Fig. 6.14. Also we notice that there are similar features in the flux profiles shown in Figs. 6.10 and 6.14, except that the flux profiles in Fig. 6.14 have larger magnitude due to the stronger radiative forcing. The similarity between these profiles in different soundings under different forcing situations suggests that these boundary layers are in the same equilibrium state. This further supports two points. The first is that the horizontal variation of the infrared radiative cooling will not affect the equilibrium state of the boundary layer. A more detailed infrared radiative transfer calculation which considers the geometrical or the horizontal inhomogeneity effects of these buoyancy driven cloud cells may not be necessary if we are primarily concerned with steady state solutions. The second point is that the stratocumulus clouds can remain solid without breakup even under the circumstance of strong entrainment. The fact that the non-interactive radiation U1 and U2 cases reach the same equilibrium as the S case implies that it is impossible to break up the stratocumulus by the entrainment instability mechanism under typical large scale mean conditions. The moisture source from the ocean surface plus the buoyancy driven convective circulations guarantee the solid stratocumulus clouds under the strong entrainment situation.

CHAPTER VII

SUMMARY AND CONCLUSIONS

In spite of previous research on the cloud-topped marine boundary layer, some problems remain. It is generally believed that infrared radiation off the cloud top is an essential element in the maintenance of a mixed layer 500 to 1000 meters or more in thickness. Previous observations indicate that cloud top radiative cooling is likely to undergo significant horizontal as well as vertical variability. Thus, one question discussed in the dissertation is whether the dynamics of the marine boundary layer is affected by variability in the spatial distribution of radiative cooling. Another question studied concerns the stability of the clouds. It is suggested under certain conditions (Lilly, 1968; Deardorff, 1980; Randall, 1980) cloud-topped entrainment instability may occur, leading to a rapid increase of entrainment. It is usually thought that this mechanism is responsible for the breakup and the transition of stratocumulus into scattered cumulus. However, the measurements taken in the last decade do not seem to support this theoretical argument. There are more observations having very large negative Θ jumps than positive Θ jumps (Fig.2.3), with the cloud layer remaining solid for quite a long time (Fig.2.5). The question of entrainment instability deserves further attention.

There are quite a few assumptions involved in the study of marine stratocumulus by thermodynamic analysis as well as by use of mixed layer models. The thermodynamic theory of entrainment instability considers only the importance of evaporative cooling of the mixed parcel and its possible feedback on the dynamics. The resultant buoyancy in the unstable case is dependent on the mixing fraction and there is no knowledge about mixing fraction in the thermodynamic theory. Moreover, the cloud top radiative cooling as well as the subsidence are not part of the theory. Thus, the thermodynamic theory is neither closed nor sufficient to predict the cloud top entrainment instability. Dynamical

modeling with numerical techniques and resolution sufficient for the simulation of cloud top processes can eliminate most of these deficiencies involved in the thermodynamic theory and simpler models. The present dissertation is an effort in the direction of dynamical modeling. We have studied entrainment instability as well as the interaction between the dynamics and infrared radiation in the cloud-topped marine boundary layer with a high resolution Fourier-Chebyshev spectral Boussinesq model.

To investigate the impact of infrared cooling on the boundary layer dynamics, numerical simulation of the marine boundary layer convection forced by various spatial distributions of radiative cooling have been performed. The results suggest that the spatial variability in radiative cooling has no impact on the boundary layer equilibrium dynamics so long as the cooling is confined to the turbulent region. This insensitivity is probably due to the shorter time scale of the turbulence mixing. Before radiation can cool a local region appreciably, turbulence must have already mixed downward the cloudy parcels. The infrared radiation sensitivity of the model seems primarily related to the vertical positioning of the cooling relative to the inversion. Since the theory of radiative transfer does not support an infrared cooling occurring in the capping inversion (zero cloud fraction or non-turbulent region), a detailed radiative transfer calculation or observation to take the spatial variability of cloud-topped cooling into account is not necessary. On the other hand, the model's infrared radiation sensitivity indicates a requirement for further observations and theoretical calculations on the distribution of the radiation cooling in the region between the zero and the non-zero cloud fraction.

To further test the original hypothesis of Lilly, an initial value problem with a large cold anomaly was studied. With this approach, the free interaction of evaporative cooling and dynamics is allowed. It was found that there are great similarities in results for the stable case S and unstable case U2. No sign of cloud breakup was observed in either case. The fact that the entrainment of dryer air in the U2 case is so close to the high water vapor content S case indicates that there is not enough evaporative cooling in the U2 mixing process. Due to this insufficient evaporation, saturation of the entrained air is not guaranteed even with a -7 K jump in Θ. As a result, the mixed parcel is not colder than the surrounding environment and entrainment ceases. It is thought that the lack of sufficient evaporation

of the cloudy air when the dry parcel was introduced from above may be the key missing ingredient from the classical entrainment instability argument.

The entrainment instability problem was then explored by the radiatively forced experiments. These forced simulations include the effects of diabatic heating, turbulence and large scale mean conditions. A large scale subsidence is specified in the model according to a climatic divergence value of 5×10^{-6} s^{-1}. The sea surface temperature specified is about the same as the surface air temperature. The radiative forcings are of two kinds. In the interactive radiative forcing experiments, the infrared cloud-top cooling is proportional to the cloud liquid water mixing ratio and is thus inhomogeneous in both space and time. For the non-interactive radiative forcing, the cloud top cooling is homogeneous in space and time. Some of this fixed cooling will be applied to the clear region between cloud cells. The stratocumulus simulated in all cases appear to be domed shaped with sharp liquid water gradients on the sides. The updraft is in the center of the convective cell while the downdraft is near the side of the cell. The downdraft regions do not always have higher cloud bases as predicted by the simple mixed layer model. This indicates that the downdraft may not be always undergoing much mixing with the inversion air. There is only one cell of circulation in the vertical. We do not observe any vertically decoupled circulation in the present study. These cloud cells can decay and reform in a finite time (Fig. 6.7). The appearance and disappearance of the cloud holes may have nothing to do with the entrainment instability. The stratocumulus do not break up even in those cases where strong entrainment is occurring (Figs. 6.12 and 6.13). The ocean surface provides infinite moisture while the buoyant cells carry moisture upward into the cloud layer against the entrainment drying, thus guaranteeing the existence of solid stratocumulus. Stronger entrainment does not necessarily imply entrainment instability due to the presence of buoyancy cells coupled to the ocean surface. This agrees with the fact that when the radiative forcing is about the same, the magnitude of the total water and liquid water flux increases as the water vapor mixing ratio above the cloud decreases. The flux profiles computed from a one hour average show great similarity in all the simulations despite the differences in forcing and the presence of strong entrainment in some cases. This further supports two points. First, the horizontal variation of the infrared cooling will not affect the equilibrium state of the boundary layer. A more

detailed observation or theoretical calculation of the infrared radiation to consider the geometrical or the horizontal inhomogeneity effect of these buoyancy driven cloud cells may not be necessary if we are after the steady state structure of the boundary layer. Secondly, unless there are unlikely multiple equilibria on the time scale of hours, the stratocumulus in the U1 and U2 cases will not break up by the entrainment instability mechanism under typical climatic local mean conditions(e.g. sea surface temperature, subsidence).

While the present model results seem to be consistent with observations which indicate that entrainment instability may not break up stratocumulus, there are still numerous questions which need to be studied. An immediate question is what mechanisms control the transition of stratocumulus regime to trade wind cumulus regime and the breakup of stratocumulus off the California coast ? Our feeling from the study of the satellite pictures and synoptic maps is that the stratocumulus may break up due to increased subsidence. The cold advection after the passage of synoptic trough, the land-sea breeze off southern California, Santa Ana wind conditions and the higher boundary layer top at the southern end of the stratocumulus region are examples of possible larger subsidence than the typical climatic value. More modeling studies will be performed along this direction. The other possible problem is whether the stratocumulus will break up over land when the Θ jump across cloud top satisfies certain criteria. Similarly, the detached mixed layer over the ocean as reported by Nicholls and Leighton (1986) deserves further attention. Also the importance of the solar radiation as well as drizzle effects have yet to be determined. By properly including these two physical mechanisms in the model, a decoupling of the cloud and sub-cloud layers might be simulated. Even though the present model results indicate that the horizontal as well as the vertical variability of infrared radiation will not affect the equilibrium dynamics of the boundary layer, further study on the time scales of radiation and turbulent mixing is needed. Finally, it may also be worth the effort to construct the parcel paths from the dynamical model simulations under various sea surface temperatures and compare them with the stratocumulus model with an internal circulation by Wang and Albrecht (1986).

REFERENCES

Albrecht, B. A., A. K. Betts, W. H. Schubert, and S. K. Cox, 1979a: A model of the thermodynamic structure of the trade wind boundary layer: Part I: Theoretical development and sensitivity tests. *J. Atmos. Sci.*, **36**, 73–89.

Albrecht, B. A., 1979b: A model of the thermodynamic structure of the trade wind boundary layer: Part II: Applications. *J. Atmos. Sci.*, **36**, 90–98.

Albrecht, B. A., R. S. Penc and W. H. Schubert, 1985: An observational study of cloud-topped mixed layers. *J. Atmos. Sci.*, **42**, 800–822.

Arakawa, A., 1975: Modeling clouds and cloud processes for use in climate models. Report of the international study conference on the physical basis of climate modeling, Stockholm, 29 July–10 August 1974, GARP Publ. Ser. No. 16.

Asai, T., and K. Nakamura, 1978: A numerical experiment of air mass transformation processes over warmer sea. Part I: Development of a convectively mixed layer. *J. Meteor. Soc. Japan*,**56**, 424–434.

Betts, A. K., 1982: Saturation point analysis of moist convective overturning. *J. Atmos. Sci.*, **39**, 1484–1505.

Betts, A. K., 1983: Thermodynamics of mixed stratocumulus layers: Saturation point budgets. *J. Atmos. Sci.*, **40**, 2655–2670.

Bougeault, P., 1981a: Modeling the trade-wind cumulus boundary layer. Part I: Testing the ensemble cloud relations against numerical data. *J. Atmos. Sci.*, **38**, 2414–2428.

Bougeault, P., 1981b: Modeling the trade-wind cumulus boundary layer. Part II: A higher-order one-dimensional model. *J. Atmos. Sci.*, **38**, 2429–2439.

Bougeault, P., 1982: Cloud-ensemble relations based on the Gamma probability distribution for the higher-order models of the planetary boundary layer. *J. Atmos. Sci.*, **39**, 2691–2700.

Bougeault, P., 1985: The diurnal cycle of the marine stratocumulus layer: A higher-order model study. *J. Atmos. Sci.*, **42**, 2826–2843.

Brost, R., D. H. Lenschow and J. C. Wyngaard, 1982: Marine stratocumulus layers. Part I: Mean conditions. *J. Atmos. Sci.*, **39**, 800–817.

Burk, S. D., 1978: The moist boundary layer with a higher order turbulence closure model. *J. Atmos. Sci.*, **34**, 629–638.

Caughey, S. J., B. A. Crease and W. T. Roach, 1982: A field study of nocturnal stratocumulus. II: Turbulence structure and entrainment. *Quart. J. Roy. Meteor. Soc.*, **109**, 124–144.

Caughey, S. J. and M. Kitchen, 1984: Simultaneous measurements of the turbulent and microphysical structure of nocturnal stratocumulus cloud. *Quart. J. Roy. Meteor. Soc.*, **110**, 13–34.

Chen, C., and W. R. Cotton, 1983a: Numerical experiments with a one-dimensional higher turbulence model: simulation of the Wangara Day 33 case. *Bound-Layer Meteor.*, **25**, 375–404.

Chen, C., and W. R. Cotton, 1983b: A one-dimensional simulation of the stratocumulus-capped mixed layer. *Bound-Layer Meteor.*, **25**, 289–321.

Davis, P. J., and P. Rabinowitz, 1984: Methods of Numerical Integration. Academic Press, 612pp.

Deardorff, J. W., 1976: On the entrainment rate of a stratocumulus-topped mixed layer in a strong inversion. *Quart. J. Roy. Meteor. Soc.*, **102**, 563–582.

Deardorff, J. W., 1980a: Cloud-top entrainment instability. *J. Atmos. Sci.*, **37**,131–147.

Deardorff, J. W., 1980b: Stratocumulus-capped mixed layers derived from a three-dimensional model. *Boundary-Layer Meteor.*, **18**, 495– 527.

Deardorff, J. W., 1981: On the distribution of mean radiative cooling at the top of a stratocumulus-capped mixed layer. *Quart. J. Roy. Met. Soc.*, **107**, 191–202.

Deardorff, J. W., and J. A. Businger, 1980: Comments on: "Marine stratocumulus convection. Part I. Governing equations and horizontally homogeneous solutions". *J. Atmos. Sci.*, **37**, 481–482.

Eliasen, E., B. Machenhauer, and E. Rasmussen, 1970: On a numerical method for integration of the hydrodynamical equations with a spectral representation of the horizontal fields. Report No. 2, Institut for Teoretisk Meteorologi, Kobenhavns Universitet, 35 pp.

Fravalo, C., Y. Fouquart, and R. Rosset, 1981: The sensitivity of a model of low stratiform clouds to radiation. *J. Atmos. Sci.*, **38**, 1049– 1062.

Fouquart, Y., 1985: WMO Workshop on Modeling of the Cloud-Topped Boundary layer. Fort Collins, Colorado.

Fulton S. R. and W. H. Schubert, 1987: Chebyshev spectral methods for limited-area models. I: Model problem analysis. *Mon. Wea. Rev.*, **116**, to appear.

Gerber, H., 1986: Tethered balloon measurements at San Nicolas Island (Oct. 1984): Instrumentation, data summary, preliminary data interpretation. Naval Research Laboratory Report 8972, 77pp.

Gottlieb, D., and S. A. Orszag, 1977: Numerical Analysis of Spectral Methods. NSF-CBMS Monograph No. 26, NTIS No. AD- A056 922, Soc. Ind. and Appl. Math., Philadelphia, 172 pp.

Grassl, H., 1975: Albedo reduction and radiative heating of clouds by absorbing aerosol particles. *Contrib. Atmos. Phys.*, **48**, 199–210.

Hanson, H. P., 1981: Note on stratocumulus instability. *Tellus*, **33**, 109–112.

Hanson, H. P., 1982: EPOCS-1981 Summary Data Report: Aircraft measurements of radiation, turbulent transport and profiles in the atmospheric and oceanic boundary layers of the Pacific off California. NOAA Tech. Memo. ERL ESG-1, 157pp.

Hanson, H. P., 1984: On mixed-layer modeling of the stratocumulus-topped marine boundary layer. *J. Atmos. Sci.*, **41**, 1226–1234.

Kahn, P. H., and J. A. Businger, 1979: The effect of radiative flux divergence on entrainment of a saturated convective boundary layer. *Quart. J. Roy. Meteor. Soc.*, **105**, 303–306.

Kraichnan, R. H., 1967: Inertial ranges in two-dimensional turbulence. *Phys. Fluids*, **10**, 1417–1423.

Kraus, H., and E. Schaller, 1978a: Steady-state characteristics of inversions capping a well-mixed PBL. *Bound-Layer Meteor.*, **14**, 83–104.

Kraus, H., and E. Schaller, 1978b: A note on the closure in Lilly-type inversion models. *Tellus*, **30**, 284–288.

Kuo, H.-C., 1983: Radiation fields in maritime stratocumulus. M.S. Thesis. Colorado State University.

Langlois, W. E., 1973: A rapidly convergent procedure for computing large-scale condensation in a dynamical weather model. *Tellus*, **25**, 86–87.

Lenschow, D. H., 1973: Two examples of planetary boundary layer modification over the Great Lakes. *J. Atmos. Sci.*, **30**, 568–581.

Lenschow, D. H., and E. M. Agee, 1976: Preliminary results from the Air Mass Transformation Experiment (AMTEX). *Bull. Amer. Meteor.*, **57**, 1346–1355.

Lilly, D. K., 1968: Models of cloud-topped mixed layers under a strong inversion. *Quart. J. Roy. Meteor. Soc.*, **94**, 292–309.

Lilly, D. K., and W. H. Schubert, 1980: The effects of radiative cooling in a cloud-topped mixed layer. *J. Atmos. Sci.*, **37**, 482–487.

Moeng, C.-H., 1986: Large-eddy simulation of a stratus-topped boundary layer. Part I: Structure and budgets. *J. Atmos. Sci.*, **43**, 2886–2900.

Moeng, C.-H., 1987: Large-eddy simulation of a stratus-topped boundary layer. Part II: Implications for mixed-layer modeling. *J. Atmos. Sci.*, **44**, in press.

Nakamura, K., and T. Asai, 1985: A numerical experiment of airmass transformation process over warmer sea: Part II: Interaction between small-scale convections and large-scale flow. *J. Meteor. Soc. Japan*, **63**, 805–827.

Nicholls, S., 1984: The dynamics of stratocumulus: aircraft observations and comparisons with a mixed-layer model. *Quart. J. Roy. Meteor. Soc.*, **110**, 783–820.

Nicholls, S., and J. Leighton, 1986: An observational study of the structure of stratiform cloud sheets: Part I: Structure. *Quart. J. Roy. Meteor. Soc*, **112**, 431–460.

Nicholls, S., and J. D. Turton, 1986: An observational study of the structure of stratiform cloud sheets: Part II: Entrainment. *Quart. J. Roy. Meteor. Soc*, **112**, 461–480.

Ninomiya, K., 1975: Large-scale aspects of air mass transformation over the East China Sea during AMTEX'74. *J. Meteor. Soc. Japan*, **53** 285–303.

Nitta, T., 1976: Large-scale heat and moisture budgets during the Air Mass Transformation Experiment. *J. Meteor. Soc. Japan*, **54**, 1–14.

Ogura, Y., and N. A. Phillips, 1962: Scale analysis of deep and shallow convection in the atmosphere. *J. Atmos. Sci.*, **19**, 173–179.

Oliver, D. A., W. S. Lewellen, and G. G. Williamson, 1978: The interaction between turbulent and radiative transport in the development of fog and low-level stratus. *J. Atmos. Sci.*, **35**, 301–316.

Orszag, S. A., 1970: Transform method for the calculation of vector-coupled sums: Application to the spectral form of the vorticity equation. *J. Atmos. Sci.*, **27**, 890–895.

Paltridge, G. W., 1974: Infrared emissivity, shortwave albedo and the microphysics of stratiform water clouds. *J. Geophys. Res.*, **79**, 4053–4058.

Platt, C. M. R., 1976: Infrared absorption and liquid water content in stratocumulus clouds. *Quart. J. Roy. Meteor. Soc.*, **102**, 553–561.

Randall, D. A., 1980a: Entrainment into a stratocumulus layer with distributed radiative cooling. *J. Atmos. Sci.*, **37**, 148–159.

Randall, D. A., 1980b: Conditional instability of the first kind upside-down. *J. Atmos. Sci.*, **37**, 125–130.

Reynolds, D. W., T. H. Vonder Haar, and S. K. Cox, 1975: The effect of solar radiation absorption in the tropical troposphere. *J. Appl. Met.*, **14**, 433–444.

Riehl, H., 1979: Climate and weather in the tropics. Academic Press, 611pp.

Roach, W. T., R. Brown, S. J. Caughey, B. A. Crease and A. Slingo, 1982: A field study of nocturnal stratocumulus. I: Mean structure and budgets. *Quart. J. Roy. Meteor. Soc.*, **108**, 103–123.

Rogers, D. P., and J. W. Telford, 1986: Metastable stratus tops. *Quart. J. Roy. Meteor. Soc.*, **112**, 481–500.

Schaller, E., and H. Kraus, 1981a: The role of radiation in an inversion-capped planetary boundary layer. part I: The need for a detailed consideration of radiative processes. *Bound-Layer Meteor.*, **20**, 485–495.

Schaller, E., and H. Kraus, 1981b: The role of radiation in an inversion-capped planetary boundary layer. Part II: The internally interactive radiative-convective model. *Bound-Layer Meteor.*, **20**, 497–513.

Schubert, W. H., 1976: Experiments with Lilly's cloud-topped mixed layer model. *J. Atmos. Sci.*, **33**, 436–446.

Schubert, W. H., Wakefield, J. S., Steiner, E. J., and S. K. Cox, 1979a: Marine stratocumulus convection. Part I: Governing equations and horizontally homogeneous solutions. *J. Atmos. Sci.*, **36**, 1286–1307.

Schubert, W. H., J. S. Wakefield, E. J. Steiner and S. K. Cox, 1979b: Marine stratocumulus convection, Part II: Horizontally inhomogeneous solutions. *J. Atmos. Sci.*, **36**, 1308–1324.

Schubert, W. H., G. D. Taylor, S. R. Fulton and M. DeMaria, 1984: A Chebyshev spectral method for boundary layer models. *Arch. Met. Geoph. Biocl.*, **Ser. A33**, 117–126.

Slingo, A., R. Brown and C. L. Wrench, 1982b: A field study of nocturnal stratocumulus. Part III. High resolution radiative and microphysical observations. *Quart. J. Roy. Meteor. Soc.*, **108**, 145–165.

Slingo, A., S. Nicholls and J. Schmetz, 1982a: Aircraft observations of marine stratocumulus during JASIN. *Quart. J. Roy. Meteor. Soc.*, **108**, 833–856.

Stage, S. A., and J. A. Businger, 1981a: A model for entrainment into a cloud-topped marine boundary layer. Part I: Model description and application to a cold-air outbreak episode. *J. Atmos. Sci.*, **38**, 2213–2229.

Stage, S. A., and J. A. Businger, 1981b: A model for entrainment into a cloud-topped marine boundary layer. Part II: Discussion of model behavior and comparison with other models. *J. Atmos. Sci.*, **38**, 2230– 2242.

Stephens, G., G. W. Paltridge and C. M. R. Platt, 1978: Radiation profiles in extended water clouds. Part III. Observations. *J. Atmos. Sci.*, **35**, 2133–2141.

Stephens, G., and M. R. Platt, 1987: Aircraft observations of the radiative and microphysical properties of stratocumulus and cumulus cloud fields. *J. Atmos. Sci.* To appear.

Taylor, P. K., A. L. M. Grant, H. Gunther and G. Olbruck, 1983: Mass, momentum, sensible heat and latent heat budgets for the lower atmosphere. *Phil. Trans. R. Soc. Lond. A*, **308**, 275–290.

Tennekes, H., 1978: Turbulent flow in two and three dimensions. *Bull. Amer. Meteor. Soc.*, **59**, 22–28.

Turner, J. S., 1973: Buoyancy effects in fluids. Cambridge University Press. 368pp.

Twomey, S., 1978: Comments on 'Effects of cloud size and cloud particles on satellite-observed reflected brightness'. *J. Atmos. Sci.*, **308**, 2389–2390.

Wakefield, J. S., and W. H. Schubert, 1976: Design and execution of the marine stratocumulus experiment. Atmos. Sci. Pap. No. 256, Colorado State University, 74 pp.

Wakefield, J. S., and W. H. Schubert, 1981: Mixed-layer model simulation of eastern North Pacific stratocumulus. *Mon. Wea. Rev.*, **109**, 1952–1968.

Wang, S. and B. A. Albrecht, 1986: A stratocumulus model with an internal circulation. *J. Atmos. Sci.*, **43**, 2374–2391.

Weaver, C., 1987: Ph.D. Dissertation, Colorado State University.

Welch, R. M., S. K. Cox, and J. M. Davis., 1980: Solar radiation and clouds. *Met. Mon.*, **17**, No. 39. *Amer. Met. Soc.*

Wiscombe, W. J., R. M. Welch, and W. D. Hall., 1984: The effect of very large drops on cloud absorption. Part I: Parcel Models. *J. Atmos. Sci.*, **41**, 1336–1355.

APPENDIX A

DERIVATION OF THE SPECTRAL COEFFICIENT EQUATIONS

Equations (3.14)–(3.17) are obtained by taking the Fourier-Chebyshev inner product (defined by (3.11)) of each of the equations (3.1)–(3.4) with the basis function $T_n(z')e^{2\pi imz/L}$. For example, from (3.2) we obtain (3.15) with $\hat{A}^{(1,0)}_{mn}$, $\hat{D}^{(0,1)}_{mn}$ and $\hat{\vartheta}^{(1,0)}_{mn}$ given by

$$\hat{A}^{(1,0)}_{mn} = \frac{2}{\pi c_n}\left\langle \frac{\partial A}{\partial x}, T_n(z')e^{2\pi imz/L}\right\rangle = i\left(\frac{2\pi m}{L}\right)\hat{A}_{mn}\,, \tag{A.1}$$

$$\hat{B}^{(0,1)}_{mn} = \frac{2}{\pi c_n}\left\langle \frac{\partial B}{\partial z}, T_n(z')e^{2\pi imz/L}\right\rangle\,, \tag{A.2}$$

$$\hat{\vartheta}^{(1,0)}_{mn} = \frac{2}{\pi c_n}\left\langle \frac{\partial \vartheta}{\partial x}, T_n(z')e^{2\pi imz/L}\right\rangle = i\left(\frac{2\pi m}{L}\right)\hat{\vartheta}_{mn}\,. \tag{A.3}$$

To evaluate (A.2) we substitute the Fourier-Chebyshev expansion for B to obtain

$$\hat{B}^{(0,1)}_{mn} = \frac{4}{H\pi c_n}\sum_{m'=-M}^{M}\sum_{n'=0}^{N}\hat{B}_{m'n'}\left\langle \frac{\partial T_{n'}(z')}{\partial z'}e^{2\pi im'z/L}, T_n(z')e^{2\pi imz/L}\right\rangle\,. \tag{A.4}$$

Using the Chebyshev derivative relation

$$\frac{\partial T_n(z')}{\partial z'} = \left\{\begin{array}{ll} 2n(T_{n-1}+T_{n-3}+\cdots+T_3+T1) & n \text{ even} \\ 2n(T_{n-1}+T_{n-3}+\cdots+T_4+T2)+nT_0 & n \text{ odd}\end{array}\right\} \tag{A.5}$$

it is easy to show that

$$\left\langle \frac{\partial T_{n'}(z')}{\partial z'}e^{2\pi im'z/L}, T_n(z')e^{2\pi imz/L}\right\rangle = \left\{\begin{array}{ll} n'\pi & m'=m \text{ and } n'+n \text{ odd}, n<n' \\ 0 & \text{otherwise}\end{array}\right\} \tag{A.6}$$

which allows (A.4) to be written as

$$\hat{B}^{(0,1)}_{mn} = \frac{4}{Hc_n}\sum_{\substack{n'=n+1\\ n'+n \text{ odd}}}^{N} n'\hat{B}_{mn'} \tag{A.7}$$

The derivations of (3.16) and (3.17) proceed similarly. The derivation of (3.14) involves second derivatives. Taking the Fourier-Chebyshev inner product of (3.1) with $T_n(z')e^{2\pi imz/L}$ we obtain

$$\frac{2}{\pi c_n}\left\langle \frac{\partial^2\psi}{\partial z^2}, T_n(z')e^{2\pi imz/L}\right\rangle - \left(\frac{2\pi m}{L}\right)^2\hat{\psi}_{mn} = \hat{\varsigma}_{mn} \tag{A.8}$$

To evaluate the first term we substitute the Fourier-Chebyshev expansion for ψ to obtain

$$\left\langle \frac{\partial^2 \psi}{\partial z^2}, T_n(z') e^{2\pi i m z/L} \right\rangle = \left(\frac{2}{H}\right)^2 \sum_{m'=-M}^{M} \sum_{n'=0}^{N} \hat{\psi}_{m'n'} \left\langle \frac{\partial^2 T_{n'}(z')}{\partial z'^2} e^{2\pi i m' z/L}, T_n(z') e^{2\pi i m z/L} \right\rangle \tag{A.9}$$

Differentiating (A.5) with respect to z' and then using (A.5) itself, it can be shown that

$$\left\langle \frac{\partial^2 T_{n'}(z')}{\partial z'^2} e^{2\pi i m' z/L}, T_n(z') e^{2\pi i m z/L} \right\rangle = \left\{ \begin{array}{cc} \frac{\pi}{2} n'(n'^2 - n^2) & \begin{array}{c} m'=m \text{ and } n'+n \text{ even}, \\ n+1<n' \end{array} \\ 0 & \text{otherwise} \end{array} \right\}, \tag{A.10}$$

which allows (A.8) to be written

$$\frac{4}{H^2 c_n} \sum_{\substack{n'=n+2 \\ n'+n \text{ even}}}^{N} n'(n'^2 - n^2) \hat{\psi}_{mn'} - \left(\frac{2\pi m}{L}\right)^2 \hat{\psi}_{mn} = \hat{\varsigma}_{mn} \,. \tag{A.11}$$

Equation (A.11) is required to hold for $n = 0, 1, 2, \ldots, N-2$. The boundary conditions $\psi(x, 0, t) = \psi(x, H, t) = 0$ are then used to close the system.

APPENDIX B

DISCRETIZATION OF A SIMPLE MODEL PROBLEM

We consider the one-dimensional nonlinear advection equation

$$\frac{\partial u}{\partial t} + u\frac{\partial u}{\partial x} = 0$$

on the infinite domain with the initial condition

$$u(x,0) = f(x) = -\tan^{-1}(x - x_0).$$

The analytical solution is

$$u(x,t) = f(x - u(x,t)t).$$

From the analytical solution we can predict the time of the shock formation as follows:

$$u = -\tan^{-1}(x - ut - x_0) \tag{B.1}$$

$$\frac{\partial u}{\partial x} = -\frac{1}{1 + (x - x_0 - ut)^2}\left(1 - t\frac{\partial u}{\partial x}\right)$$

at $x = x_0$, $u = 0$ so

$$\left(\frac{\partial u}{\partial x}\right)_{x=x_0} = -\left(1 - t\left(\frac{\partial u}{\partial x}\right)_{x=x_0}\right)$$

or

$$\left(\frac{\partial u}{\partial x}\right)_{x=x_0} = \frac{1}{t-1} \rightarrow -\infty \text{ as } t \rightarrow 1.0.$$

The analytical solution of the 1-D nonlinear advection equation can be solved numerically to any desired accuracy by fixed point iteration on (B.1) with x and t as specified parameters. Since t varies continuously from 0 to 1, if we use the analytical solution computed from the previous time as the initial guess for the next time, the method of continuation will guarantee convergence of the iteration. Fig. B.1 shows the analytical solution of the nonlinear advection equation at t=0.0, t=0.5, t=0.75 and t=1.0.

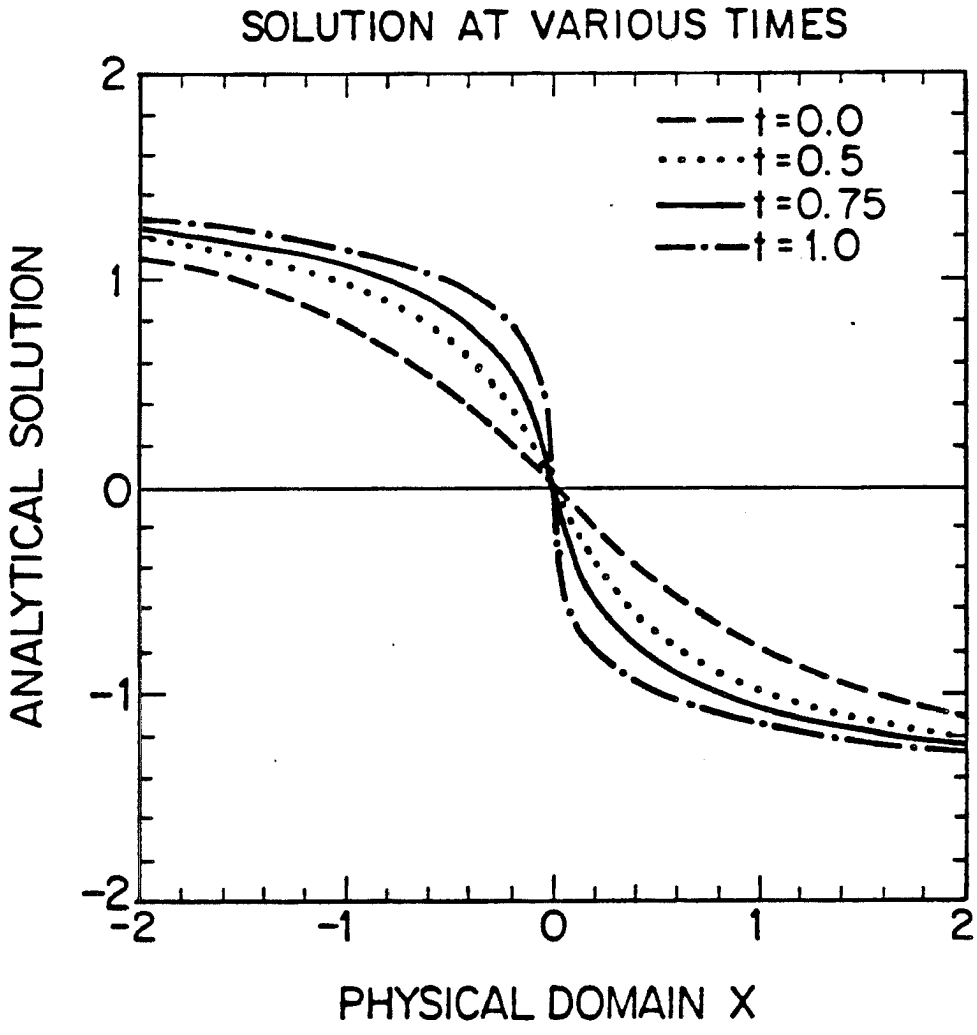

Figure B.1. The analytical solution of the nonlinear advection equation at $t = 0.0$, $t = 0.5$, $t = 0.75$ and $t = 1.0$.

Once the analytical solution is established, we consider the problem with the same initial condition on the finite domain [−1,+1]. The centered difference and Chebyshev-collocation methods then are used to solve the problem with the boundary conditions provided by the analytical solution. The corresponding error, defined as the analytical solution minus the numerical solution measured in the L2 norm, is shown in Fig. B.2 as a function of the number of degrees of freedom N for t=0.5 and t=1.0 (shock formation time). The collocation method converges exponentially to the analytical solution at t=0.5 and converges algebraically to the analytical solution at t=1.0. The different convergence properties for the collocation method are due to the fact that the smoothness of the analytical solution changes as the shock forms. The finite difference method has algebraic convergence at all times.

Fig. B.3 shows the error norm as a function of time for N=16 and N=32. The error grows with the time for these two methods and two different values of N. The collocation method is better than the finite difference method at all times except near the time of shock formation. The two methods have about the same accuracy when the shock forms.

The errors as a function of shock position for the collocation method with N=16, N=32, t=0.5, and t=1.0 are plotted in Fig. B.4. The error decreases as the shock position gets close to the boundary when t=0.5. The reason is that there are more collocation points near the boundary. But at t=1.0 the accuracy is of the same order no matter where the shock forms. The local minimum error occurs when the shock forms at the collocation points while the local maximum error is between two collocation points. In another words, the higher resolution of the Chebyshev-collocation method near the boundaries is expected only when the shock has not formed (when the numerical solution has the exponential convergence property).

We next consider the same one-dimensional nonlinear advection equation on the finite domain [−1,+1], except with the initial condition $u(x,0) = f(x) = \bar{u} - \tan^{-1}(x - x_0)$. Physically, this amounts to the previous situation with the inclusion of a mean propagation at the speed $\bar{u}$. The analytical solution by characteristics is $u(x,t) = f(x - u(x,t)t)$, which can be solved numerically by fixed point iteration. The shock formation time is still 1.0. The position of shock formation shifts from x_0 to $x_0 + \bar{u}$.

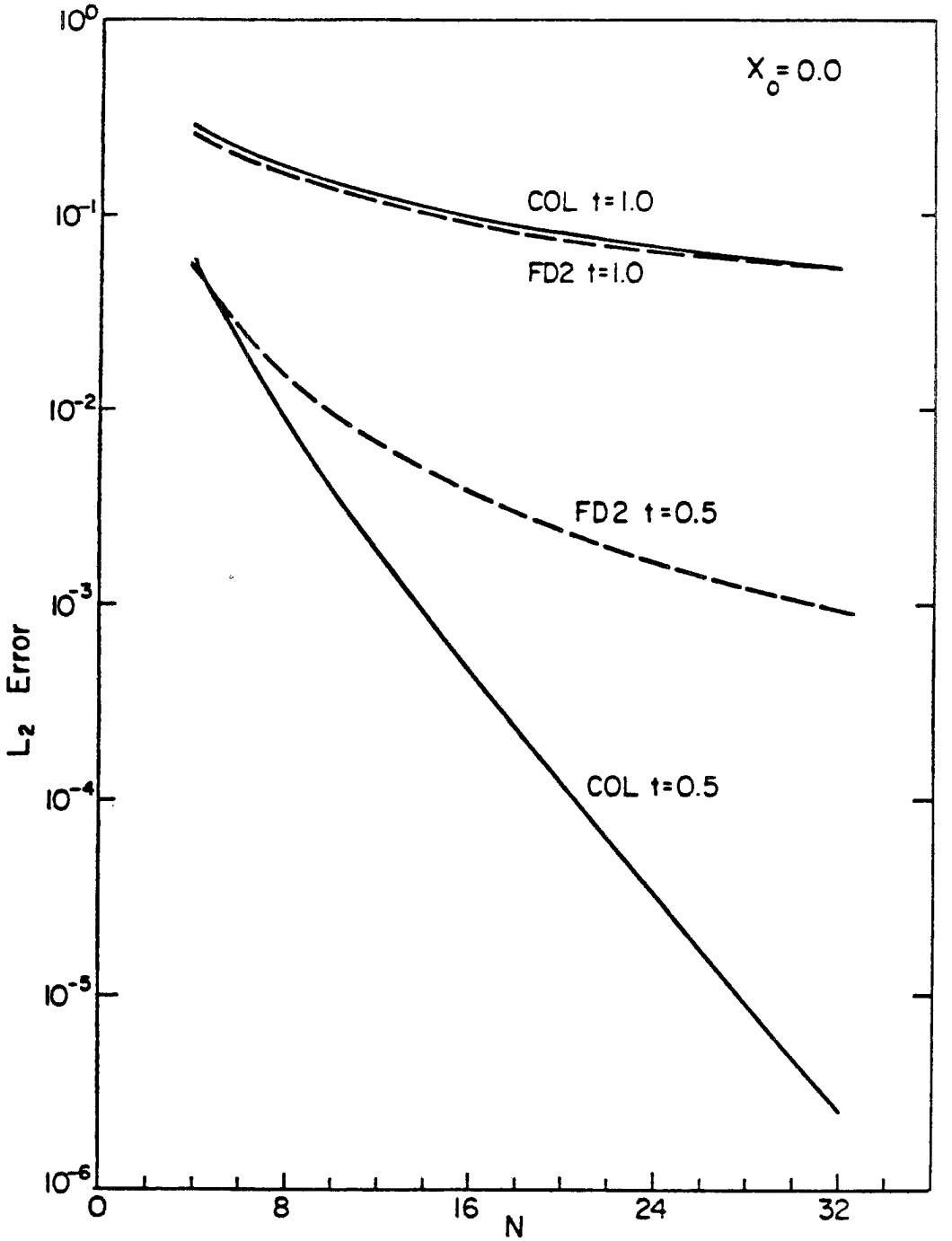

Figure B.2. L_2 error in the numerical solution of the nonlinear advection equation as a function of the number of degrees of freedom N for the collocation (COL) and the second order finite difference (FD2) methods at $t = 0.5$ and $t = 1.0$ (shock formation time). The shock formation position $X_0 = 0.0$.

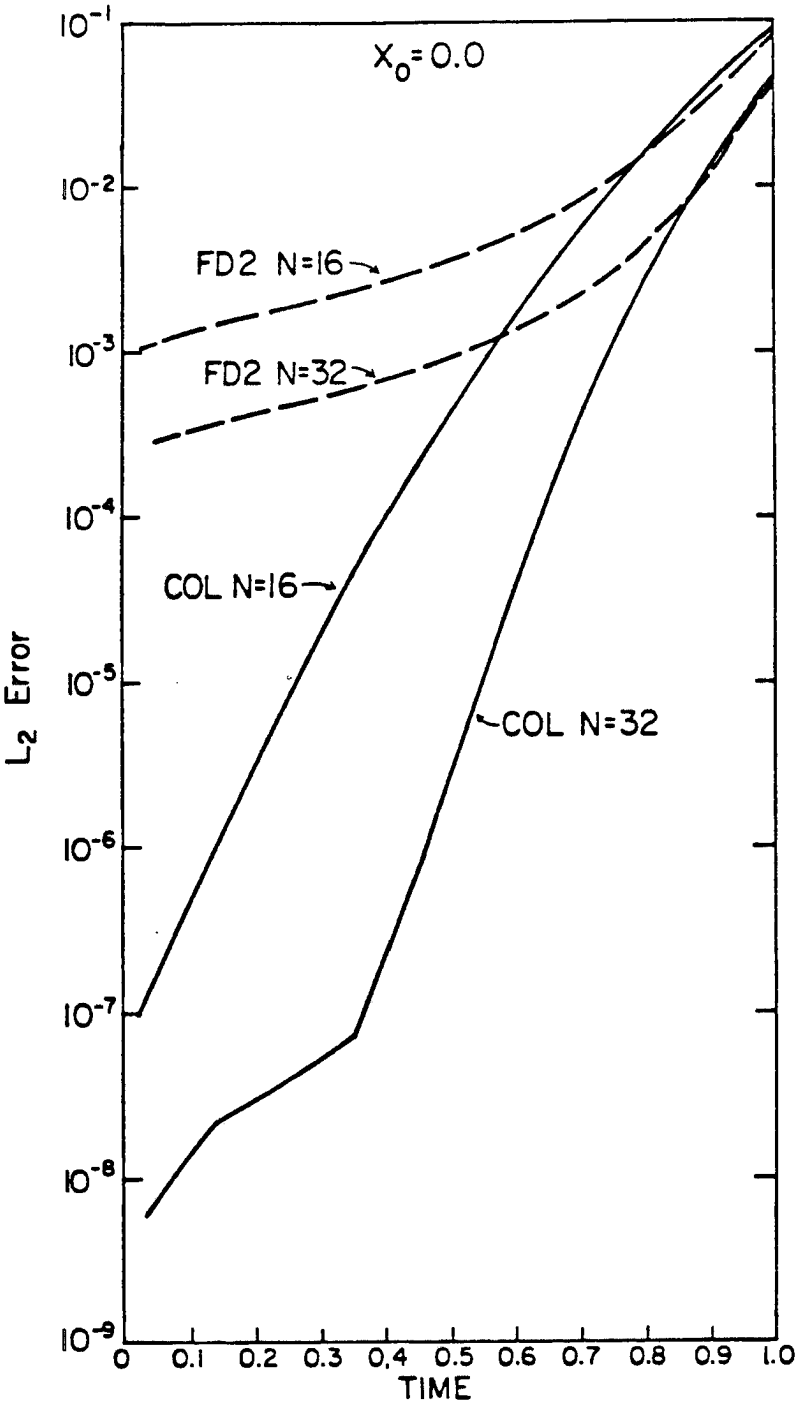

Figure B.3. L_2 error in the numerical solution of the nonlinear advection equation as a function of time for COL and FD2 methods with $N = 16$ and $N = 32$. The shock formation position $X_0 = 0.0$.

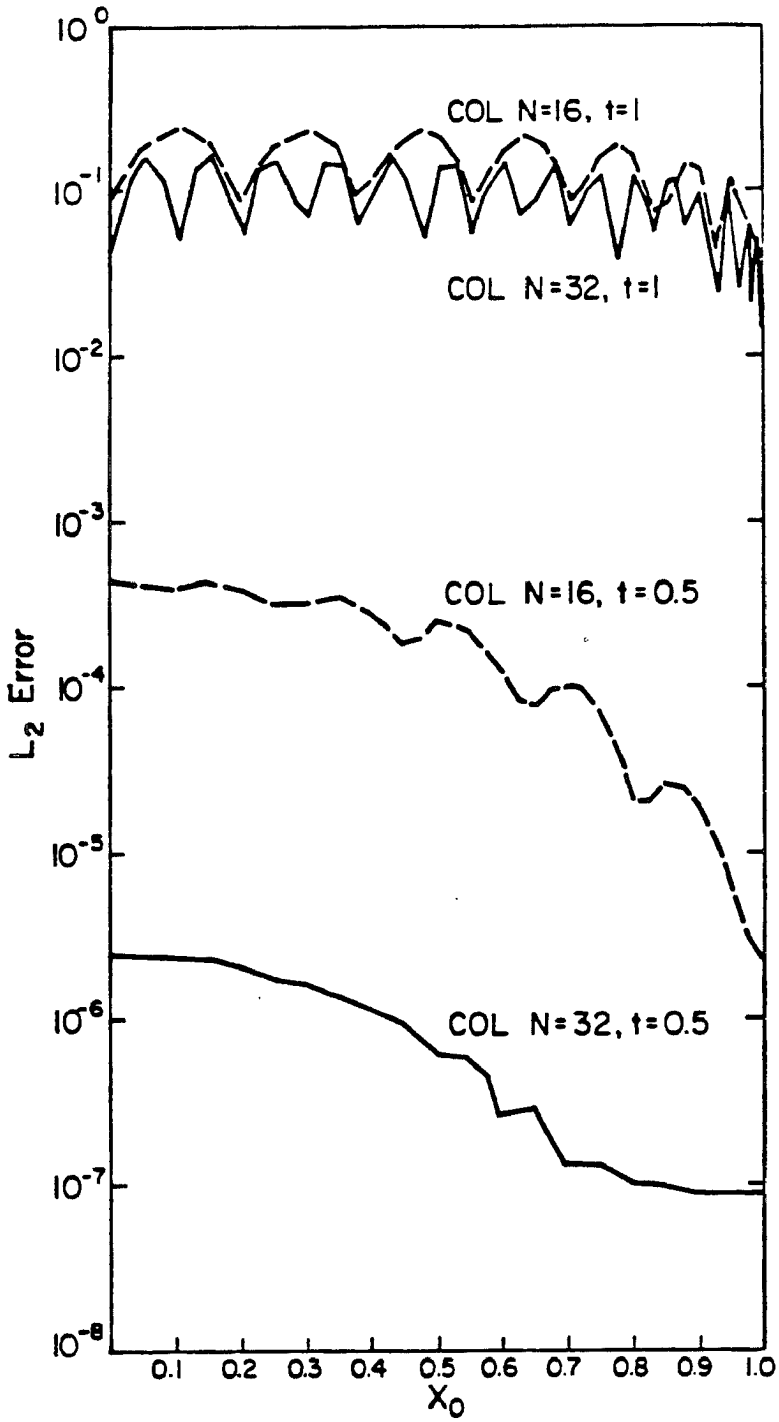

Figure B.4. L_2 error in the numerical solution of the nonlinear advection equation as a function of shock formation position X_0 for COL and FD2 methods with $N = 16$ and $N = 32$ at time t =0.5 and $t = 1.0$.

The centered difference and Chebyshev-collocation methods are again used to solve the problem with boundary conditions provided by the analytical solution. The error norm defined before as a function of the number of degrees of freedom N for t=0.5, t=0.75 and t=1.0 with $\bar{u} = 1.0, x_0 = -0.5$ are plotted in Fig. B.5. The collocation method is more accurate than the finite difference method at all times and for all N. The collocation errors in Fig. B.5 are about the same as the collocation errors in Fig. B.2 while the finite difference errors get worse. Fig. B.6 shows the error norms as a function of time for both methods with N=16 and N=32. In all cases the error grows substantially with time as the shock forms. Note that the finite difference errors are larger than the finite difference errors in Fig. B.3. These figures suggest that the collocation method can handle the advection process better than the finite difference method. Also in Fig. B.5 at t=0.75, the collocation method is ten times more accurate than the finite difference method for N=32. Because the shock is not of prime interest in most atmospheric studies, we can conclude that the collocation method is far more accurate than the finite difference method even in the case of a steep gradient (e.g. t=0.75).

Finally, the error norm as a function of the advection speed $\bar{u}$ for both methods with N=32 at t=0.5, t=0.75 and t=1.0 is shown in Fig. B.7. The finite difference error increases as the advection speed $\bar{u}$ increases while the collocation error is less sensitive to $\bar{u}$. This is another indication that the finite difference method has difficulty handling the advection process.

The second order Runge-Kutta time integration scheme has been used in the results presented so far, with the time step chosen to be very small so that the error in the computation is dominated by the spatial discretization error due to the spectral method. The tau method has about the same spatial discretization error as the collocation method for this particular problem. We now consider the efficiency of several different time integration schemes. Because the size of the time step in Chebyshev spectral methods tends to be limited by accuracy rather than by stability, higher order time integration schemes may give better efficiency. To test this, the same nonlinear advection equation (without mean advection) is solved repeatedly by the tau method with different time step sizes for the second order Runge-Kutta method (RK2), second order Adams-Bashforth method (AB2), fourth

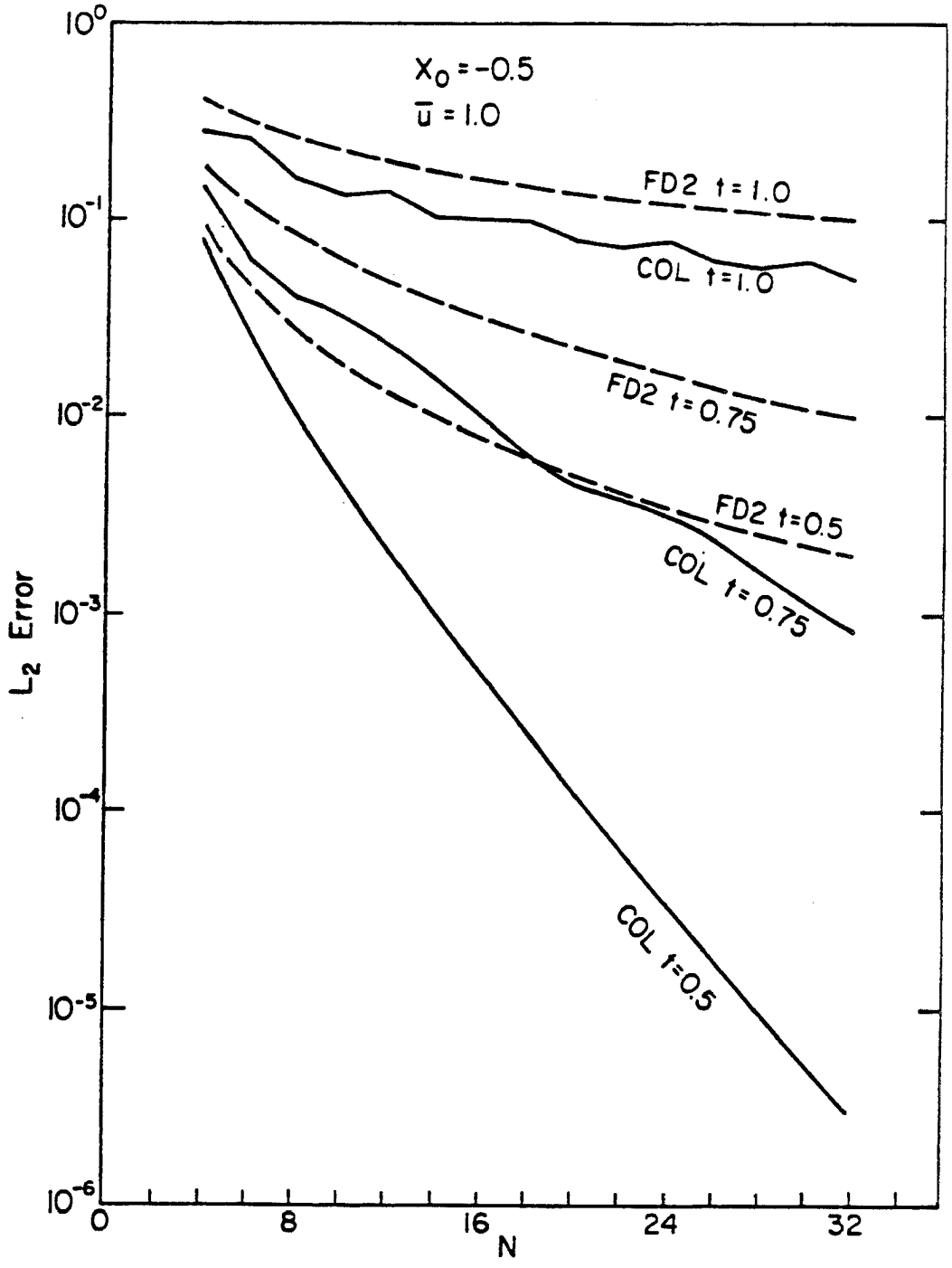

Figure B.5. L_2 error in the numerical solution of the nonlinear advection equation as a function of the number of degrees of freedom N for COL and FD2 methods at $t = 0.5$, $t = 0.75$ and $t = 1.0$. The mean propagation speed $\bar{u} = 1.0$ and $X_0 = -0.5$.

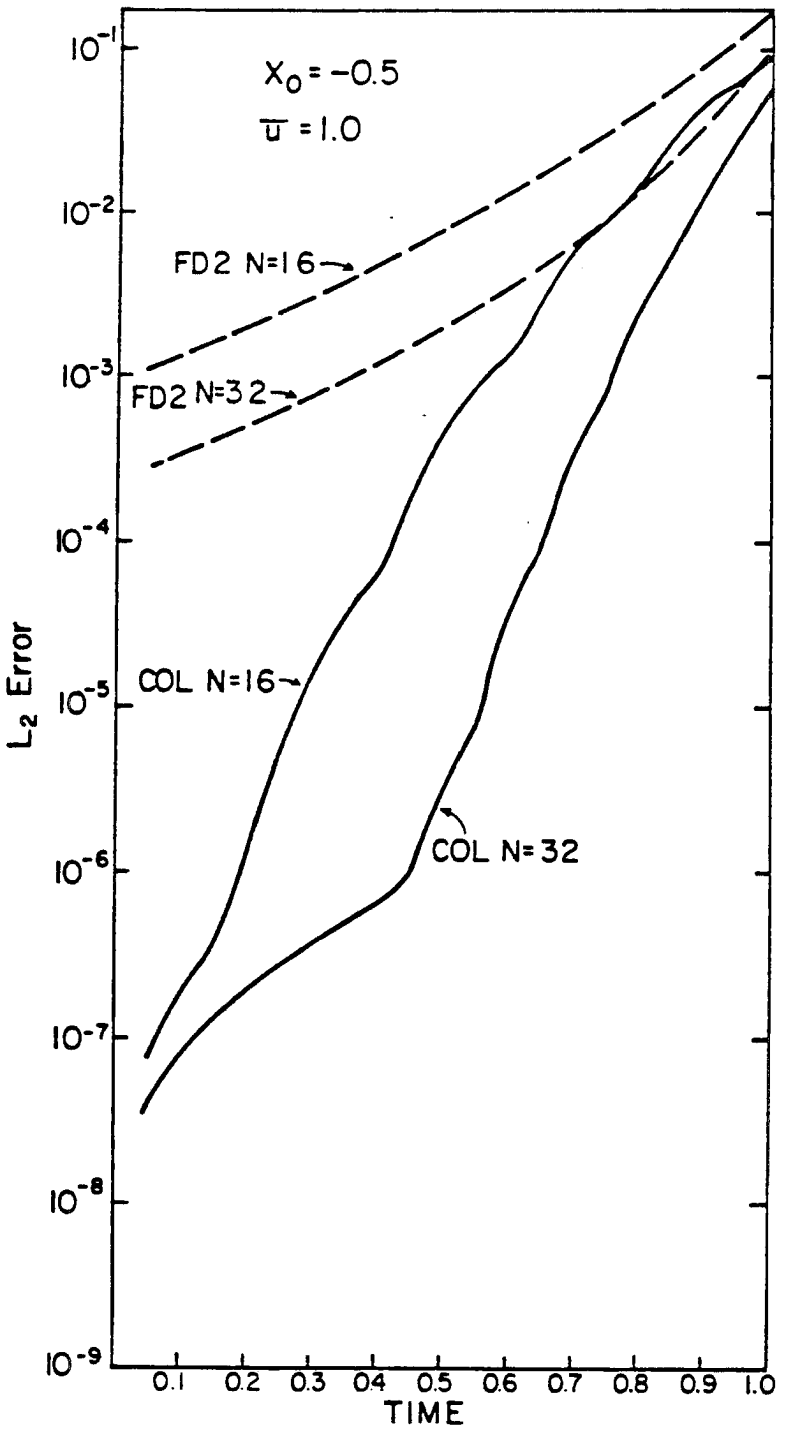

Figure B.6. Same as figure B.3 except X_0 = -0.5 and $\bar{u}$ = 1.0.

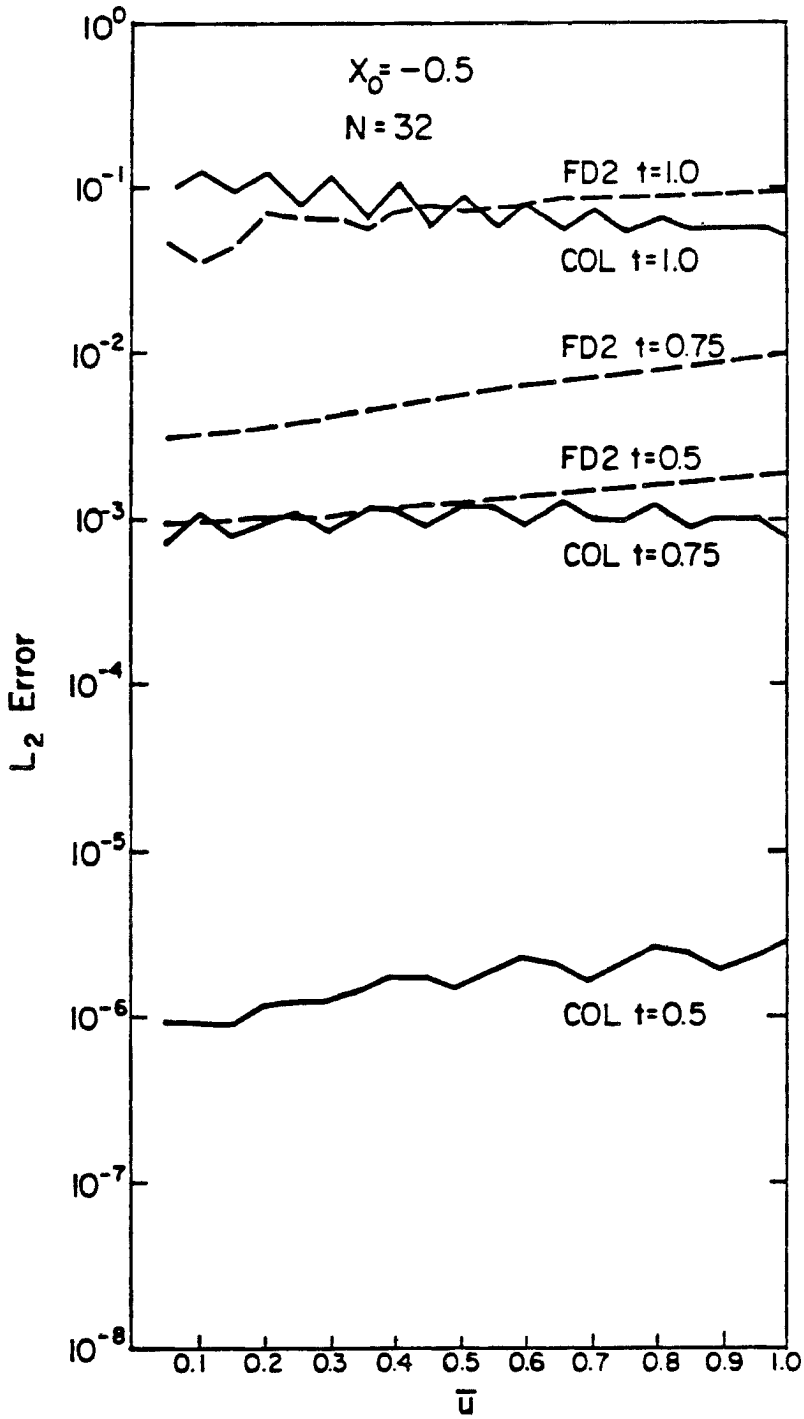

Figure B.7. L_2 error in the numerical solution of the nonlinear advection equation as a function of mean propagation speed $\bar{u}$ for COL and FD2 methods with $N = 32$ and X_0 = -0.5 at $t = 0.5$, $t = 0.75$ and $t = 1.0$.

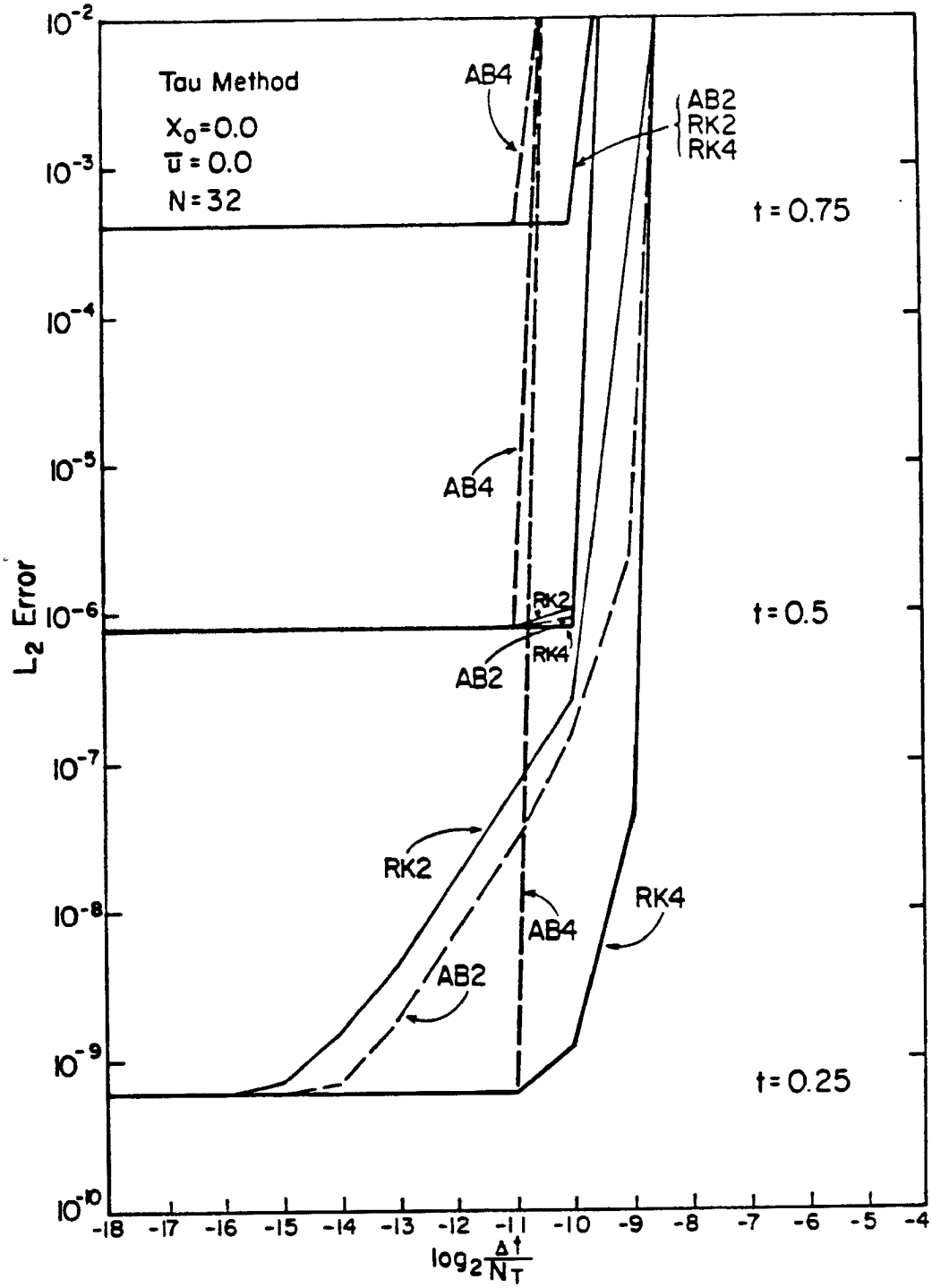

Figure B.8. L_2 error in the numerical solution of the nonlinear advection equation as a function of the time step size (Δt) divided by the number of function evaluations (N_T) for $t = 0.25$, $t = 0.5$ and $t = 0.75$ for the Tau method with $N = 32$, $\bar{u} = 0.0$. and $X_0 = 0.0$.

order Runge-Kutta method (RK4) and fourth order Adams-Bashforth method (AB4). The main difference between the RK and AB methods is that the former require more than one function evaluation each time step but no computational modes are introduced.

The error norm as a function of the time step size Δt divided by the number of function evaluations N_T for t=0.25, t=0.5 and t=0.75 is shown in Fig. B.8. The AB4 method tends to have a more severe stability condition than the other methods. The RK4 method has better efficiency than RK2 and AB2 at t=0.25, when the spectral discretization error is very small; the time step size for the second order methods is limited by accuracy and not by stability. The RK2 and AB2 methods are as good as the RK4 method at t=0.5 and t=0.75 when the spatial discretization error is considerably larger. Note that the RK4 method requires four function evaluations each time step but takes less (or an equal amount of) work than the second order methods to reach a given accuracy. Thus the fourth order Runge-Kutta method seems to be an efficient time integration scheme for use with the tau method.